

LOW ORDER WAVEFRONT SENSING AND CONTROL ON
MAGAO-X

by

Avalon McLeod

Copyright © Avalon McLeod 2023

A Thesis Submitted to the Faculty of the

JAMES C. WYANT COLLEGE OF OPTICAL SCIENCES

In Partial Fulfillment of the Requirements

For the Degree of

MASTER OF SCIENCE

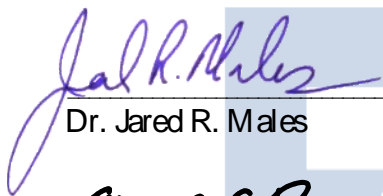
In the Graduate College

THE UNIVERSITY OF ARIZONA

2023

THE UNIVERSITY OF ARIZONA
GRADUATE COLLEGE

As members of the Master's Committee, we certify that we have read the thesis prepared by Avalon L. McLeod, titled Low Order Wavefront Sensing and Control on MagAO-X and recommend that it be accepted as fulfilling the dissertation requirement for the Master's Degree.



Dr. Jared R. Males

Date: 2023-05-01



Professor Ewan Douglas

Date: 5/3/2023

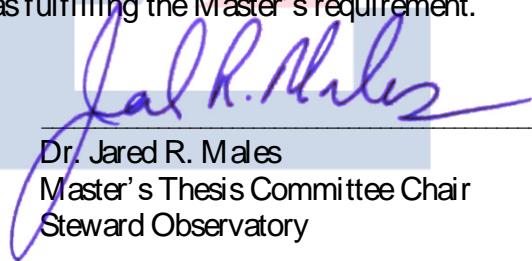


Professor Olivier Guyon

Date: 2023-06-08

Final approval and acceptance of this thesis is contingent upon the candidate's submission of the final copies of the thesis to the Graduate College.

I hereby certify that I have read this thesis prepared under my direction and recommend that it be accepted as fulfilling the Master's requirement.



Dr. Jared R. Males
Master's Thesis Committee Chair
Steward Observatory

Date: 2023-06-10

ARIZONA

Acknowledgements

I would like to thank my mother, father, and brother for supporting me throughout my entire education with the University of Arizona and always encouraging me to put my best foot forward in life and in studies. I would also like to thank my research group, the Extreme Wavefront Control Laboratory, for all their help inside and out of my research and the wonderful work environment I have been so fortunate to be a part of. I would like to especially thank my research advisor, Dr. Jared R. Males, for his invaluable mentorship in my career and education throughout my time with the XWCL. I also want to thank Dr. Olivier Guyon and Dr. Ewan S. Douglas for serving as part of my thesis review committee and encouraging me through the defense process. Finally, I would like to thank the classmates that I have had the pleasure of working with throughout my studies at the University of Arizona. I could not have gotten where I am without all of the aforementioned contributions, and I am very thankful to have gone through this experience with them all.

TABLE OF CONTENTS

ABSTRACT	11
1 INTRODUCTION	12
2 BACKGROUND	14
2.1 DIFFRACTION LIMITED IMAGING WITH GROUND BASED TELESCOPES.....	14
2.2 CORONAGRAPHY	16
2.3 PREVIOUS IMPLEMENTATIONS OF LOWFS&C AND CLOWFS&C	18
2.4 THE MAGAO-X INSTRUMENT.....	20
2.5 LOW ORDER WAVEFRONT SENSING AND CONTROL ON MAGAO-X	22
3 THEORY	25
3.1 THE FOURIER DESCRIPTION OF BEAM PROPAGATION IN MAGAO-X	25
3.2 THE PHASE DEGENERACY PROBLEM.....	28
3.3 LINEAR WAVEFRONT SENSING AND CONTROL	31
4 MODELING	33
4.1 MODELING MAGAO-X LOWFS&C CALIBRATIONS IN PYTHON.....	33
4.2 OPTIMIZATION METRICS	40
4.3 OPTIMIZATION RESULTS	42
4.3.1 <i>Optimization results for camlowfs</i>	43
4.3.2 <i>Optimization results for camsci1 and camsci2</i>	48
4.4 CONCLUSIONS FROM OPTIMIZATION.....	51
5 IMPLEMENTATION ON MAGAO-X	55
5.1 INTERFACING WITH MAGAO-X	55
5.2 METRICS FOR LOWFS&C AND CLOWFS&C PERFORMANCE ON MAGAO-X.....	61
5.3 IN-LAB TEST RESULTS.....	62
5.3.1 <i>Testing the sci2-Hα calibration</i>	63
5.3.2 <i>Testing the lowfs-z calibration</i>	69
5.3.3 <i>Testing the lowfs-z-c calibration</i>	75
5.3.4 <i>Additional notes</i>	87
5.4 ON-SKY RESULTS 2023A	88
5.4.1 <i>On-sky performance of LOWFS&C for PSF optimization</i>	90
5.4.2 <i>On-sky performance of LOWFS&C for coronagraph control</i>	98
5.4.3 <i>Additional notes</i>	104
6 CONCLUSIONS	104
7 APPENDIX A	107
7.1 LOWFS&C SIMULATION CODE.....	107
8 APPENDIX B	117
8.1 SCI2-H α TEST 1 CAMERA PARAMETERS	117
8.2 SCI2-H α TEST 2 CAMERA PARAMETERS	117
8.3 LOWFS-Z TEST 1 CAMERA PARAMETERS.....	117
8.4 LOWFS-Z TEST 2 CAMERA PARAMETERS.....	118
8.5 LOWFS-Z-C TEST 1 CAMERA PARAMETERS	118
8.6 LOWFS-Z-C TEST 2 CAMERA PARAMETERS	118
9 APPENDIX C	119
9.1 SCI2-HA ON-SKY TEST CAMERA PARAMETERS	119
9.2 SCI1-R ON-SKY TEST.....	119
9.3 LOWFS-Z-C ON-SKY TEST	119

10 APPENDIX D 120
 10.1 LOWFS&C CALIBRATIONS FROM 2023A 120
 10.2 CLOWFS&C CALIBRATIONS FROM 2023A 120
11 REFERENCES..... 121

LIST OF FIGURES

Figure 1. Model of MagAO-X on the Nasymth platform when used on-sky at the Magellan Clay telescope.....	13
Figure 2. High level depiction of an AO system showing the use of a wavefront sensor and deformable mirror to send a corrected wavefront to a science camera [5].	15
Figure 3. Outline of basic Lyot coronagraph with aperture (a), focal plane / Lyot mask (b), Lyot stop (c), and detector (d). On axis light is depicted in orange and off axis light is depicted in purple.	16
Figure 4. Non-coronagraphic vs. coronagraphic focal plane images simulated in python using Fraunhofer propagation.	17
Figure 5. MagAO-X upper and lower optical tables outlining the HOWFS&C (green) and science/coronagraphic (red) optical paths.....	21
Figure 6. Schematic showing reflected light off Lyot focal plane mask (FPM) reimaged to camlowfs for CLOWFS&C.	24
Figure 7. Simulation of perfect circular aperture showing Fraunhofer propagation to a focal plane.....	27
Figure 8. Simulation showing Fraunhofer propagation of normalized Magellan telescope aperture.	27
Figure 9. Even low order phase aberrations in the pupil plane with positive and negative phase components [$i\text{Asin}(\theta)$] and uniform amplitude components [$\text{Acos}(\theta)$].....	29
Figure 10. Odd low order phase aberrations in the pupil plane with positive and negative phase components [$i\text{Asin}(\theta)$] and uniform amplitude components [$\text{Acos}(\theta)$].....	29
Figure 11. Example of +/- vertical astigmatism at a focal plane.	30
Figure 12. Example of +/- vertical trefoil at a focal plane.....	30
Figure 13. Example of +/- vertical astigmatism and vertical trefoil at a defocused image plane.	31
Figure 14. Simulation of pixel responses within a $1.5 \lambda/D$ radius on a MagAO-X science camera in $H\alpha$ when $0 \text{ nm} - 150 \text{ nm}$ RMS astigmatism phase error is added to the DM.....	32
Figure 15. Depiction of a longitudinal defocus shift when applying Zernike defocus to the pupil plane.....	34
Figure 16. Testing defocus modeling with MagAO-X in z-band.	35
Figure 17. LOWFS&C calibration model summary.....	36
Figure 18. Modeled Zernike mode basis in the pupil plane with the obstructed aperture.	38
Figure 19. Example of modeled defocused reference image.	39
Figure 20. Example of modeled BF mask.	39
Figure 21. Modeled example of WFS modal response basis.....	40
Figure 22. Example self-response matrix for the Zernike mode basis.	41
Figure 23. SNR and standard deviation vs camlowfs defocus value in r-band.	43
Figure 24. Self-response matrix and ideally defocused PSF for camlowfs in r-band.....	43
Figure 25. SNR and standard deviation vs camlowfs defocus value in $H\alpha$	44
Figure 26. Self-response matrix and ideally defocused PSF in $H\alpha$ on camlowfs.	44
Figure 27. SNR and standard deviation vs camlowfs defocus value for i-band.	45
Figure 28. Self-response matrix and ideally defocused PSF for the i-band on camlowfs.	45
Figure 29. SNR and standard deviation vs. camlowfs defocus value with defocus range extended to 40 mm in i-band.....	46
Figure 30. SNR and standard deviation vs camlowfs defocus value in z-band.....	46

Figure 31. Self-response matrix and ideally defocused PSF z-band on camlowfs.	47
Figure 32. SNR and standard deviation vs. camlowfs defocus value with defocus range extended to 40 mm in z-band.	47
Figure 33. SNR and standard deviation vs camsci1/camsci2 defocus value in r-band.....	48
Figure 34. Self-response matrix and ideally defocused PSF in i-band on camsci1/camsci2.....	48
Figure 35. SNR and standard deviation vs camsci1/camsci2 defocus value for the H α filter (656 nm).	49
Figure 36. Self-response matrix and ideally defocused PSF in H α on camsci1/camsci2.....	49
Figure 37. SNR and standard deviation vs camsci1/camsci2 defocus value in i-band.....	50
Figure 38. Self-response matrix and ideally defocused PSF in i-band on camsci1/camsci2.....	50
Figure 39. SNR and standard deviation vs camsci1/camsci2 defocus value z-band.	51
Figure 40. Self-response matrix and ideally defocused PSF for z--band on camsci1/camsci2. ...	51
Figure 41. Plot of SNR values from LOWFS&C model optimization as a function of wavelength.	52
Figure 42. Plot of defocus locations from LOWFS&C model optimization as a function of wavelength.	53
Figure 43. SNR and standard deviation values for an extended defocus range in H α on camsci1/camsci2.	54
Figure 44. SNR and standard deviation value for an extended defocus range in z-band on camsci1/camsci2.	54
Figure 45. Example reference image and BF mask created by CACAO for an H α -narrow calibration on camsci2.	57
Figure 46. Example Zernike modal basis on DM NCPC used to train a LOWFS&C loop in H α on camsci2.	58
Figure 47. Example of Zernike mode WFS response images used to train LOWFS&C loop in H α on camsci2.	59
Figure 48. Example BF mask and reference image for reflected light calibration on camlowfs in z-band.....	61
Figure 49. sci2-H α calibration reference image and bright field mask.	63
Figure 50. Example open and closed loop WFS images for sci2-H α test 1.	64
Figure 51. Global gain, block gains, and leak applied to the LOWFS&C loop for sci2-H α test 1.	64
Figure 52. MSE over data acquisition time for sci2-H α test 1.	65
Figure 53. Mode reconstruction over data acquisition time for sci2-H α test 1.	66
Figure 54. Example open and closed loop WFS images for sci2-H α test 2.	66
Figure 55. Global gain, block gains, and leak applied to the LOWFS&C loop for sci2-H α test 2.	67
Figure 56. MSE over data acquisition time for sci2-H α test 2.	67
Figure 57. Mode reconstruction over data acquisition time for sci2-H α test 2.	68
Figure 58. lowfs-z calibration reference image and bright field mask.	69
Figure 59. Example open and closed loop WFS images for lowfs-z test 1.	70
Figure 60. Global gain, block gains, and leak applied to the LOWFS&C loop for lowfs-z test 1.	70
Figure 61. MSE over data acquisition time for lowfs-z test 1.	71
Figure 62. Mode reconstruction over data acquisition time for lowfs-z test 1.	71

Figure 63. Example open and closed loop WFS images for lowfs-z test 2.	73
Figure 64. Global gain, block gains, and leak applied to the LOWFS&C loop for lowfs-z test 2.	73
Figure 65. MSE over data acquisition time for lowfs-z test 1.	74
Figure 66. Mode reconstruction over data acquisition time for lowfs-z test 2.	74
Figure 67. lowfs-z-c reference image and bright field mask.	75
Figure 68. Global gain, block gains, and leak applied to the LOWFS&C loop for lowfs-z-c test 1.	76
Figure 69. Median coronagraphic image for the lowfs-z-c test 1.	76
Figure 70. Sparkle PSFs used to monitor relative change in Strehl for lowfs-z-c test 1.	77
Figure 71. Sparkle core sums over the data acquisition period of lowfs-z-c test 1.	77
Figure 72. Example reference subtracted cropped image and image with indication of radial pixel sum locations for lowfs-z-c test 1.	78
Figure 73. Radial pixel sums over the data acquisition period for lowfs-z-c test 1.	78
Figure 74. Running mean of radial pixel sums over the data acquisition period for lowfs-z-c test 1.	79
Figure 75. Running standard deviation of radial pixel sums over the data acquisition period for lowfs-z-c test 1.	79
Figure 76. Mean squared error of the WFS images over the data acquisition period for lowfs-z-c test 1.	80
Figure 77. Mode reconstruction over data acquisition period for lowfs-z-c test 1.	81
Figure 78. Global gain, block gains, and leak applied to the LOWFS&C loop for lowfs-z-c test 2.	82
Figure 79. Median image for the lowfs-z-c test 2.	82
Figure 80. Sparkle PSFs used for monitoring relative change in Strehl for lowfs-z-c test 2.	83
Figure 81. Sparkle PSF core sums over the data acquisition period for lowfs-z-c test 2.	83
Figure 82. Example dark subtracted cropped image and image with indication of radial pixel sum locations for lowfs-z-c test 2.	84
Figure 83. Radial pixel sums over the data acquisition period for lowfs-z-c test 2.	84
Figure 84. Running mean of radial pixel sums over the data acquisition period for lowfs-z-c test 2.	85
Figure 85. Running standard deviation of radial pixel sums over the data acquisition period for lowfs-z-c test 2.	85
Figure 86. Mean squared error of WFS images over the data acquisition period for lowfs-z-c test 2.	86
Figure 87. Mode reconstruction over data acquisition period for lowfs-z-c test 2.	86
Figure 88. Reference image and bright field mask for the sci2-H α calibration.	88
Figure 89. Reference image and bright field mask for the sci1-r calibration.	89
Figure 90. Reference image and bright field mask for the lowfs-z-c calibration.	89
Figure 91. Loop control parameters over data acquisition time for the sci2-H α on-sky test.	91
Figure 92. Dark subtracted images from the science image cube for the sci2-H α on-sky test. ...	92
Figure 93. 5x5 ROI PSF pixel sum over data acquisition time for the sci2-H α on-sky test.	92
Figure 94. Mean squared error over data acquisition time for the sci2-H α on-sky test.	93
Figure 95. Correction coefficients for the first 10 Zernike modes over the data acquisition period of the sci2-H α on-sky test.	94
Figure 96. Loop control parameters over data acquisition time for the sci1-r on-sky test.	95

Figure 97. Dark subtracted images from the science image cube for the sci1-r on-sky test.	96
Figure 98. 5x5 ROI PSF pixel sum over data acquisition time for the sci1-r on-sky test.	96
Figure 99. Mean squared error over data acquisition time for the sci1-r on-sky test.	97
Figure 100. Correction coefficients for the first 10 Zernike modes over the data acquisition period of the sci1-r on-sky test.....	97
Figure 101. Loop control parameters for the data acquisition period of lowfs-z-c on-sky evaluation.....	99
Figure 102. Median image for lowfs-z-c on-sky test.....	99
Figure 103. Sparkle PSF ROIs for lowfs-z-c on-sky test.....	100
Figure 104. Sparkle core sums over the data acquisition period for the lowfs-z-c on-sky test. .	100
Figure 105. Example dark subtracted cropped image and image with indication of radial pixel sum locations for lowfs-z-c on-sky test.	101
Figure 106. Radial pixel sums over the data acquisition period for the lowfs-z-c on-sky test. ..	101
Figure 107. Running mean of radial pixel sums over the data acquisition period for lowfs-z-c on-sky test.	102
Figure 108. Running standard deviation of radial pixel sums over the data acquisition period for lowfs-z-c on-sky test.	102
Figure 109. Mean squared error of WFS images over the data acquisition period for the lowfs-c-z on-sky test.	103
Figure 110. Correction coefficients for the first 10 Zernike modes over the data acquisition period of the lowfs-z-c on-sky test.....	103

LIST OF TABLES

Table 1. LOWFS&C relevant filters used in MagAO-X with indications to which cameras have those filters.....	22
Table 2. Summary of camlowfs optimization in simulation.	52
Table 3. Summary of camsci1/camsci2 optimization in simulation.	52
Table 4. Details for lab-tested calibrations including the camera used, filter used, and number of modes corresponding to each mode block.	63
Table 5. Details for on-sky tested calibrations including the camera used, filter used, and number of modes corresponding to each mode block.....	88
Table 6. Wavefront sensor camera parameters for sci2-H α test 1.....	117
Table 7. Focal plane camera parameters for sci2-H α test 1.	117
Table 8. Wavefront sensor camera parameters for sci2-H α test 2.....	117
Table 9. Focal plane camera parameters for sci2-H α test 2.	117
Table 10. Wavefront sensor camera parameters for lowfs-z test 1.....	117
Table 11. Focal plane camera parameters for lowfs-z test 1.....	117
Table 12. Wavefront sensor camera parameters for lowfs-z test 2.....	118
Table 13. Focal plane camera parameters for lowfs-z test 2.....	118
Table 14. Wavefront sensor camera parameters for lowfs-z-c test 1.....	118
Table 15. Focal plane camera parameters for lowfs-z-c test 1.	118
Table 16. Wavefront sensor camera parameters for lowfs-z-c test 2.....	118
Table 17. Focal plane camera parameters for lowfs-z-c test 2.	118
Table 18. Wavefront sensor camera parameters for sci2-h α on-sky test.....	119
Table 19. Focal plane camera parameters for sci2-h α on-sky test.	119
Table 20. Wavefront sensor camera parameters for sci1-r on-sky test.....	119
Table 21. Focal plane camera parameters for sci1-r on-sky test.....	119
Table 22. Wavefront sensor camera parameters for lowfs-z-c on-sky test.....	119
Table 23. Focal plane camera parameters for lowfs-z-c on-sky test.....	119
Table 24. LOWFS&C calibrations taken during the 2023A observing run.	120
Table 25. CLOWFS&C calibrations taken during the 2023A observing run.....	120

Abstract

Directly imaging extrasolar planets from ground-based telescopes requires advanced wavefront sensing and control (WFS&C) technologies to create and maintain high contrast images. The Extreme Adaptive Optics Instrument for the Magellan Clay 6.5 m telescope (MagAO-X) employs adaptive optics (AO) and coronagraphy to correct for atmospheric turbulence and achieve high contrasts in the visible to near-IR wavelengths. However, non-common path aberrations (NCPAs) unseen by the primary AO system, such as atmospheric dispersion and environmental influence on optical components downstream in the system, remain uncorrected for and degrade the achievable Strehl and contrast values in science images. This thesis presents an additional wavefront correction loop located in the science/coronagraphic arm of MagAO-X to correct for NCPAs and improve MagAO-X system performance. A 97-actuator ALPAO DM has been used in conjunction with low order (LO) WFS&C of up to 41 modes at the focal plane to improve science image Strehl and contrast values on sky at wavelengths as short as H-alpha (656 nm). The methods behind optimizing LOWFS&C configurations and on-sky data from observing at the Las Campanas Observatory are presented. Further applications of LOWFS and focal plane wavefront sensing are discussed, defining the advancements necessary for directly imaging difficult exoplanet targets.

1 Introduction

Thousands of extrasolar planets (exoplanets) have been discovered in the Milky Way Galaxy since the first exoplanet detection in the early 1990's [1]. These detections have been primarily made via indirect measurement techniques including the transit and radial velocity methods, with only a handful of exoplanets detected by direct imaging with ground based or space-based telescopes [2]. The transit and radial velocity detection methods rely on an exoplanet's orbit to be edge on with respect to the detection instrument. This results in a $\sim 0.5\%$ probability of detecting an exoplanet at 1 AU (Earth to the Sun distance) orbiting a star the size of our sun with these methods. Furthermore, direct spectroscopy of an exoplanet is needed to characterize its atmosphere and identify Earth-like or potentially habitable worlds. Direct imaging allows for the detection of exoplanets regardless of their orbiting geometry and provides the capability to perform spectroscopy on those imaged exoplanets. However, direct imaging poses a significant technical challenge, requiring the ability to image objects much fainter than their host star as well as spatially resolving these high contrast objects at very low angular separations. With this, imaging from ground-based telescopes requires advanced adaptive optics (AO) capabilities to correct for atmospheric turbulence and allow for diffraction-limited imaging.

The Extreme Adaptive Optics Instrument for the Magellan Clay 6.5 m telescope (MagAO-X) is an extreme adaptive optics (exAO) system optimized for high contrast imaging (HCI) in visible to near-infrared wavelengths to address this challenge. The ultimate science goal of this instrument is to directly image nearby exoplanets using reflected light from their host star. For detection of the closest known exoplanet to our solar system, Proxima Centauri b, MagAO-X will need to achieve 10^{-7} contrasts at roughly 37 mas of angular separation.

The instrument has been funded by the NSF MRI program since Sep 2016, regularly traveling between the University of Arizona (UA) for technical development, and Las Campanas Observatory (LCO) for on-sky engineering and science observations since its first light in 2019 [3]. MagAO-X also serves as a testbed for the upcoming era of extremely large telescopes, used to develop the technologies necessary for future ground-based exAO & HCI systems such as the Extreme Adaptive Optics System for the Giant Magellan Telescope (GMagAO-X).

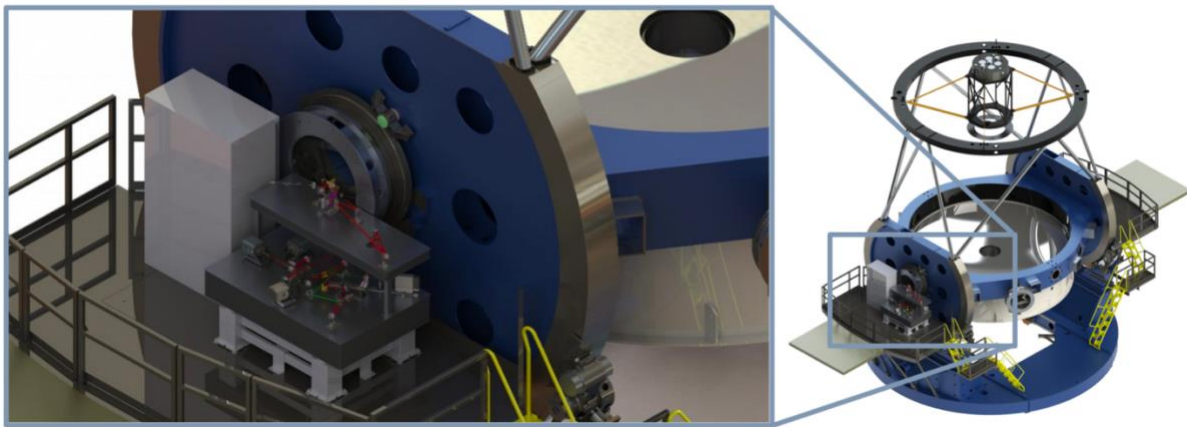


Figure 1. Model of MagAO-X on the Nasmyth platform when used on-sky at the Magellan Clay telescope.

MagAO-X is currently equipped with a 2040 actuator Boston Micromachines (BMC) deformable mirror (DM) controlled by a pyramid wavefront sensor (PyWFS) at up to 2 kHz for high order wavefront sensing and control (HOWFS&C). A supporting 97 actuator ALPAO DM is used for offloading low orders such as tip, tilt, and defocus to avoid actuator saturation on the 2k DM. This HOWFS&C loop takes place upstream of many optical components in the instrument, including the coronagraphs used to create high contrast images and the science cameras. Diffraction effects that are non-common path (NCP) to the HOWFS&C loop resulting from aberrations in the optics (static), variable states of instrument alignment (quasi-static), and atmospheric effects such as dispersion (dynamic) will degrade the quality of the science images and achievable coronagraph performance [4]. To improve the wavefront quality at the

coronagraph and science planes of the system, a secondary low order wavefront sensing and control (LOWFS&C) loop has been integrated into the science and coronagraphic arm of MagAO-X with an additional non-common path correcting (NCPC) 97 actuator ALPAO DM. A reflective focal plane mask in the coronagraph allows for rejected starlight to be reimaged and used for coronagraphic low order wavefront sensing and control (CLOWFS&C) during high contrast imaging. In non-coronagraphic imaging, science cameras can be used as low order wavefront sensors for PSF optimization to correct for static and quasi-static wavefront errors preceding a science observation.

2 Background

2.1 Diffraction limited imaging with Ground Based Telescopes

Diffraction limited imaging refers to an optical system's ability to eliminate all factors that degrade the achievable resolution of the system other than the fundamental diffraction limit caused by the aperture stop of the system. The achievable resolution can be represented as the minimum angular separation α of two point-sources that are distinguishable in a focal plane. In astronomical imaging, α is given by the approximate FWHM of the point spread function (PSF) resulting from a telescope with entrance pupil diameter D imaging at a wavelength λ .

$$\alpha = \frac{\lambda}{D}$$

It is important to note that a star's distance from our solar system and nearly-isotropic irradiance profile allows a star and any surrounding exoplanets to be considered point source objects. This makes it clear that the ability for a telescope to image an exoplanet at a given angular separation from its host star is fundamentally limited by the wavelength used for observation and the diameter of the telescope. A common metric for the performance of a diffraction limited

instrument is the Strehl ratio, or the ratio of peak intensity contained by an imaged PSF to the theoretical maximum.

Atmospheric turbulence will limit a ground-based telescope's resolving capabilities much before the diffraction limit can be reached. Employing adaptive optics (AO) in an optical system is a way to combat this. AO works by measuring the distortion of a wavefront via a wavefront sensor and providing a correction to the optical path with a device such as a deformable mirror.

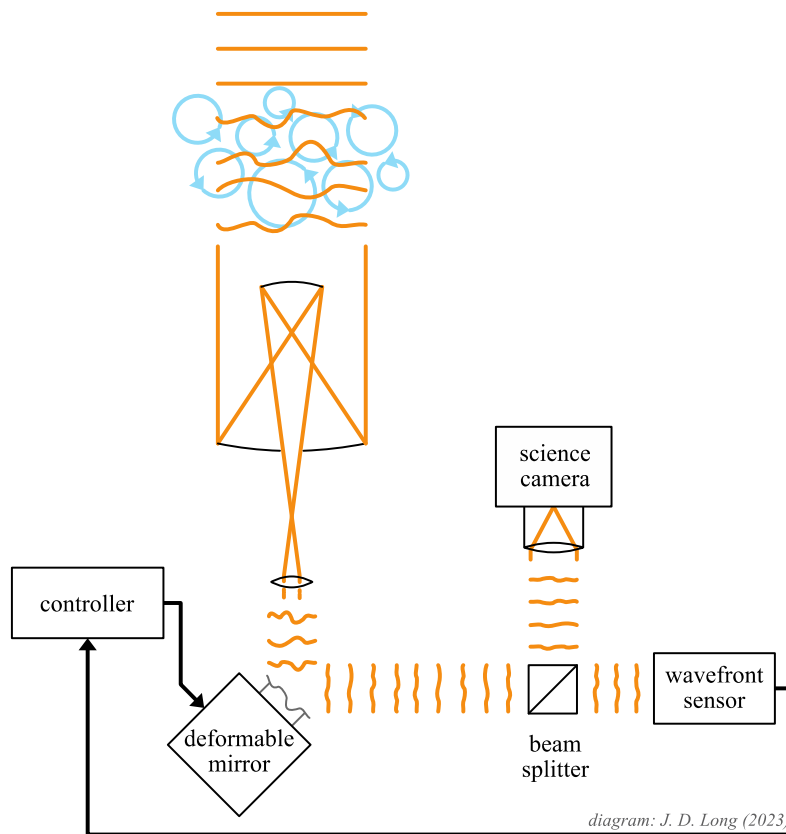


Figure 2. High level depiction of an AO system showing the use of a wavefront sensor and deformable mirror to send a corrected wavefront to a science camera [5].

Several AO systems have been developed for ground-based telescopes, primarily working in the infrared due to the challenges that come with wavefront control at lower wavelengths. Some visible AO systems have been developed for large diameter telescopes, including the Magellan AO system (MagAO) for the Magellan Clay 6.5 m telescope [6], and the Palomar Adaptive

Optics System (PALAO) for the Palomar 5 m telescope [7]. The Subaru Coronagraphic Extreme Adaptive Optics instrument (SCEAO) [8] and the SpectroPolarimetric High-contrast Exoplanet REsearch instrument (SPHERE) [9] are examples of ‘extreme’ AO systems that use adaptive optics along with high contrast imaging. Both SCEAO and SPHERE primarily work in the optical red and near-infrared wavelengths. MagAO-X has pioneered the challenge to perform AO and HCI at wavelengths as low as $H\alpha$ (656 nm), pushing the fundamental length scale to image planets close to their host star at high Strehl (> 0.7 at $H\alpha$) [3].

2.2 Coronagraphy

A coronagraph is used to block stellar light so that faint surrounding objects can be identified. The general construction of a coronagraph can be described by the Lyot coronagraph model [10] as depicted in Figure 3.

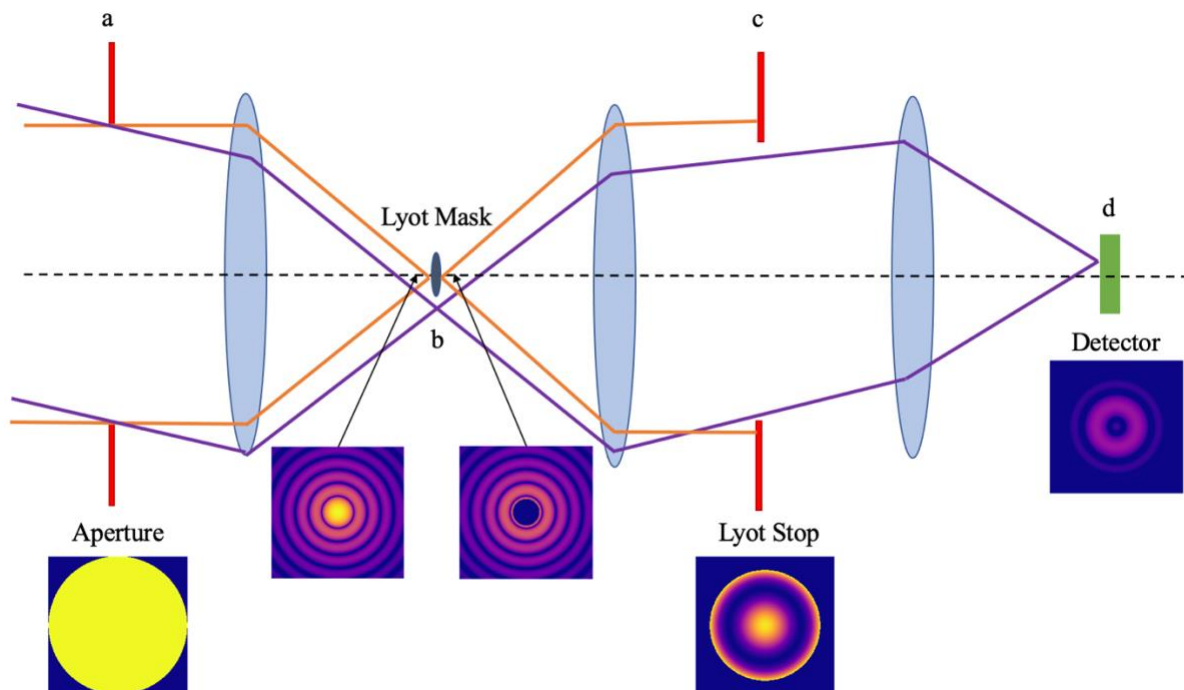


Figure 3. Outline of basic Lyot coronagraph with aperture (a), focal plane / Lyot mask (b), Lyot stop (c), and detector (d). On axis light is depicted in orange and off axis light is depicted in purple.

As shown in the figure above, on-axis light from an aperture is imaged to a coronagraphic mask located in the focal plane. This mask acts as an occulter and is sized on the order of several λ/D in radius. A $1 \lambda/D$ radius would allow for full obscuration of the PSF core, though real-world limitations (imperfect corrective abilities or optical components) typically lead to focal plane masks to be sized at several λ/D in radius. The beam is then reimaged to a pupil plane where a Lyot stop is located to block the remaining PSF core light. The off-axis light is not occulted by the Lyot mask and is imaged to a focal plane at the detector, creating the high-contrast image. Figure 4 shows a simulation of non-coronagraphic vs. coronagraphic focal plane images for a monochromatic input through a perfectly diffraction limited system. A $6 \lambda/D$ diameter Lyot mask and Lyot stop sized at 80% of the nominal pupil diameter are used. The coronagraphic image is normalized by the peak intensity of the non-coronagraphic PSF to represent achieved contrast.

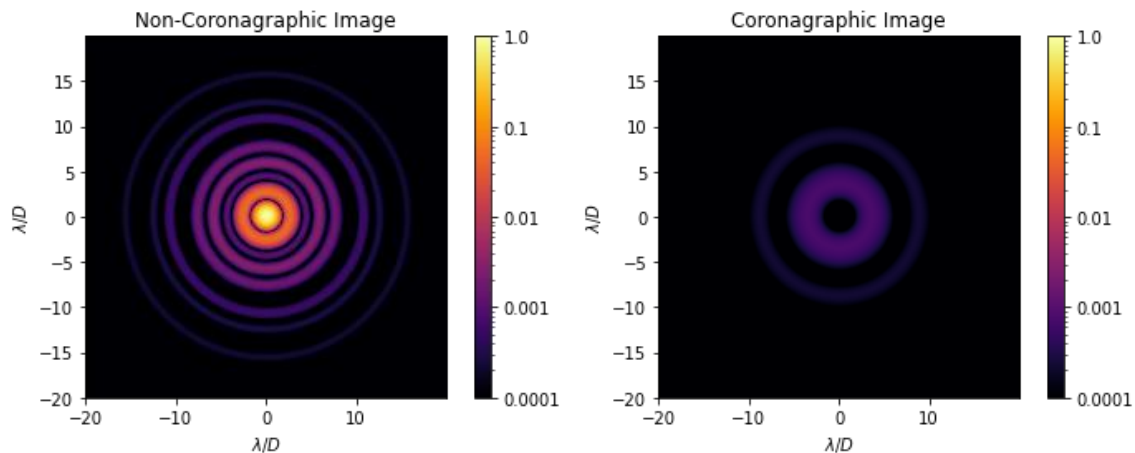


Figure 4. Non-coronagraphic vs. coronagraphic focal plane images simulated in python using Fraunhofer propagation.

The achieved contrast at a given point on a coronagraphic image is given by the ratio of the intensity at that point divided by the peak value of the non-coronagraphic PSF. The fundamental achievable contrast of a coronagraph is given as 1 minus the non-aberrated, non-

coronagraphic PSF of the telescope [11]. Several coronagraphs have been introduced to improve polychromatic performance, throughput, and account for aberrations that occur in non-ideal systems to approach this fundamental limit [11][12]. Among these undergoing implementation and testing on MagAO-X are the vector-Apodizing phase plate (vAPP) coronagraph [13] and phase-induced amplitude apodization coronagraph (PIAAC) [11][3].

2.3 Previous Implementations of LOWFS&C and CLOWFS&C

Focal plane wavefront sensing and control (FPWS&C) techniques including LOWFS&C and CLOWFS&C have been previously investigated through modeling, in lab verification, and on sky in various configurations.

CLOWFS&C has been demonstrated by Guyon et al. (2009) on the coronagraph testbed at Subaru telescope with the PIAA coronagraph [14]. The testbed CLOWFS&C configuration uses defocused rejected starlight from a PIAA coronagraph and largely investigates the ability for CLOWFS&C to correct for telescope pointing errors (tip/tilt on the primary and secondary mirrors). Correction parameters for low order modes is also discussed. The control loop was demonstrated to improve pointing errors within $3 \lambda/D$ at $0.55 \mu\text{m}$.

Guyon et al. (2009) also suggests modeling CLOWFS&C sensitivity as a function of defocus is essential for successful correction of other low order Zernike modes due to oscillatory behavior in sensitivity for orders like astigmatism and defocus.

Singh et al. (2014) describes simulations and laboratory results for CLOWFS&C with phase-mask coronagraphs [15]. A phase-mask coronagraph does not use a reflective FPM, leading to a suggested configuration that uses a reflective Lyot Stop: the Lyot-based low order wavefront sensor (LLOWFS). The reflective Lyot stop reimages the central PSF to a defocused focal plane for LOWFS&C because of limited signal to perform WFS&C in the pupil plane.

Tip/tilt errors were the primary focus of correction in this demonstration, though it was shown that defocus and astigmatism could be sensed with the LLOWFS. It was shown that tip/tilt could be controlled with a measurement accuracy of $\sim 10^{-2} \lambda/D$ at 638 nm. Noted shortcoming of the LLOWFS included a maximum tip/tilt amplitude that could be measured, high risk of modal misinterpretation when correcting other low order modes, and influence on the WFS from higher order aberrations.

LOWFS&C was demonstrated on-sky by Martinache et al. (2018) using focal plane science images and an asymmetric aperture [16]. The on-sky demonstration was done in an H-band ($1.65 \mu\text{m}$) filter with a $0.3 \mu\text{m}$ bandwidth at a total correction speed of 8 Hz. The loop was trained to control the tip/tilt through spherical Zernike modes and resulted in an $\sim 5\%$ increase in Strehl when implemented on the 0.77 magnitude on-sky target (Altair).

Miller et al. (2018) provides simulation and laboratory testbed results concerning how LOWFS&C can be implemented with the vAPP coronagraph on MagAO-X [13]. The vAPP uses an asymmetric reflective mask optimized to send 660 nm rejected starlight to a wavefront sensing image plane where LOWFS&C and linear dark field control (LDFC) [17] are implemented for NCPA control. LOWFS&C is used to correct for quasi-static aberrations (speckles) at low spatial separations at the focal plane, and LDFC is a linear control loop used for controlling higher spatial separation errors using only the brightest stellar bright field speckles. Implementing these FPWFS&C techniques was demonstrated to recover the raw contrast (6×10^{-5}) of the vAPP coronagraph across a $\sim 2\text{--}15 \lambda/D$ dark hole when 27 nm RMS wavefront error was assumed for NCPA errors in the visible.

2.4 The MagAO-X Instrument

When at the University of Arizona, MagAO-X is located in the extreme wavefront control laboratory (UA XWCL) in Steward Observatory. The instrument has an internal telescope pupil simulator that uses an NKT photonics supercontinuum source (SuperK) as an artificial point source object. Several neutral density (ND) filters are equipped both at the telescope simulator and science cameras to simulate stars of different brightness. This allows for telescope-simulation tests to be run while MagAO-X is not at LCO, including the calibration and testing of a WFS&C loop. Figure 5 shows a schematic of MagAO-X without its protective paneling to emphasize important components of the system. The BMC 2K DM (tweeter), ALPAO DM97 (woofer), and ALPAO DM97 (NCPC DM) are indicated in green. The cameras camsci1, camsci2, camlowfs, and camwfs are indicated in orange. The beam splitters responsible for dividing the light between the WFS and science/coronagraphic (sci/WFS B/S) arms are indicated in yellow. The upper portion of the bench contains the telescope simulator, tweeter, and woofer. A periscope is used to relay the pupil to the lower bench where the sci/WFS B/S splits the incoming light into the HOWFS&C arm and science/coronagraphic arm. There are two sci/WFS beam splitters available in MagAO-X that allow for an $H\alpha/IR$ of 65/35 split of the incoming beam. The science/coronagraphic beam reflects off the NCPC DM and is focused to the science cameras. A reflective component can be used in the coronagraphic/science beam to direct light to camlowfs.

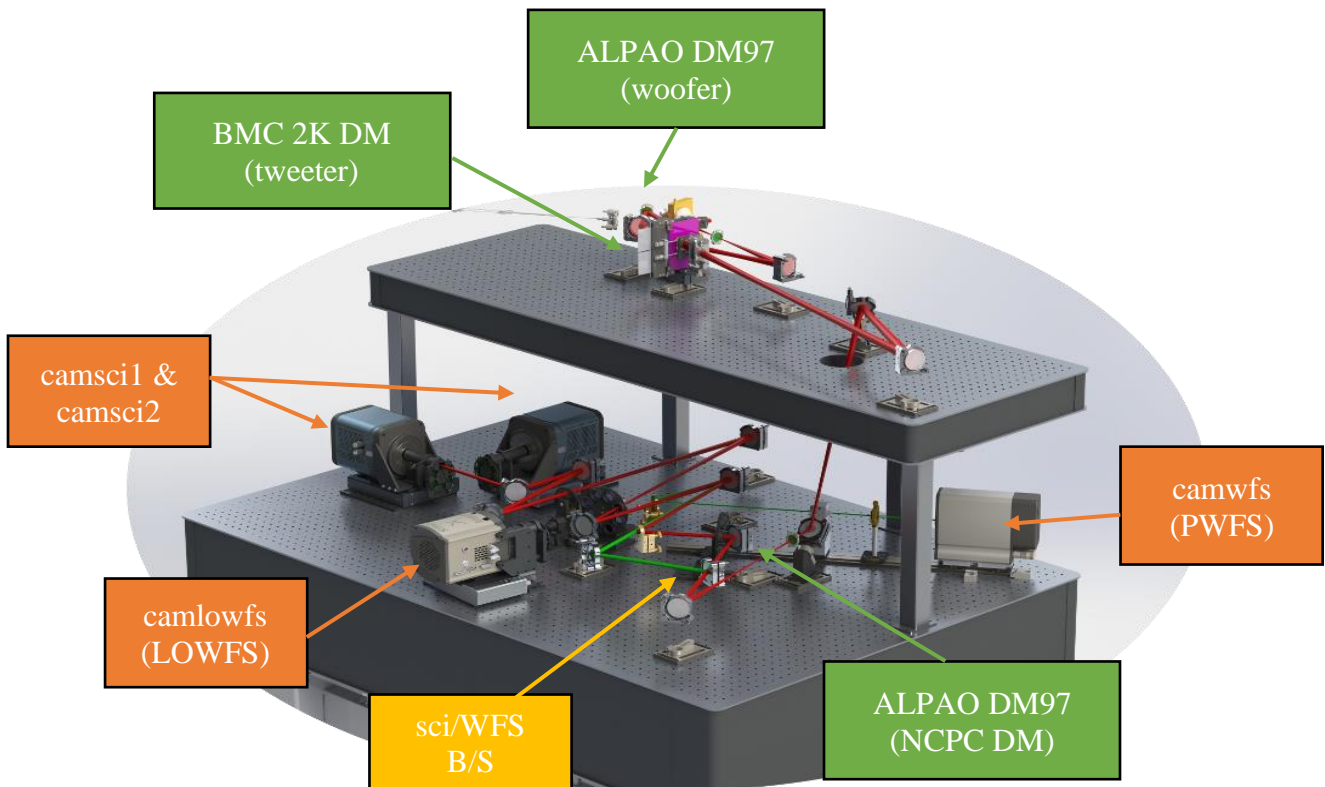


Figure 5. MagAO-X upper and lower optical tables outlining the HOWFS&C (green) and science/coronagraphic (red) optical paths.

The science cameras (camsci1 and camsci2) are Princeton Instruments ProEM HS: 1024BX3 detectors used for simultaneous science imaging. Camwfs is an OCAM2K EMCCD and is used as the WFS detector in the high order loop. Camlowfs is an Andor iXon Ultra 897 detector located in the coronagraphic arm of MagAO-X and is the dedicated detector for CLOWFS&C. The NCPC DM is used for implementing optical path corrections in the LOWFS&C and CLOWFS&C loops.

Several filters can be used for LOWFS&C with the science cameras or camlowfs in MagAO-X's current configuration. The relevant specifications for filters useful in performing LOWFS&C are given in table 1.

Table 1. LOWFS&C relevant filters used in MagAO-X with indications to which cameras have those filters.

Filter	Bandwidth [nm]	camsci1	camsci2	camlowfs
r (615 nm)	106	y	y	y
Ha (656 nm)	9	n	y	y
Ha-narrow (656 nm)	1	n	y	n
i (762 nm)	126	y	y	y
z (909 nm)	132	y	y	y

MagAO-X converts the incoming telescope beam to 9 mm in diameter at the pupil planes with F/69 imaging at the science cameras (~ 6 mas/pixel) and F/85.53 imaging at camlowfs (~ 6 mas/pixel). All DMs in MagAO-X are in pupil space, whereas all cameras have the capability to image both focal planes and pupil planes.

MagAO-X has several coronagraphs available for observers to use, the classical Lyot coronagraph being the most robust at this stage of the instruments' development. There are two Lyot masks available (chrome dot on a glass plate); one has a radius of $3 \lambda/D$ at H α (lyotsm) and the other with a radius of $5 \lambda/D$ at H α (lyotlg). Both masks are reflective, allowing for the occulted PSF to be reimaged to camlowfs. A flat mirror is present preceding the coronagraph allowing a full PSF to be imaged to camlowfs as well. With no coronagraph in place, the full PSF is imaged to the science cameras with no light reaching camlowfs.

2.5 Low order wavefront sensing and control on MagAO-X

NCPAs that result downstream of MagAO-X's HOWFS&C loop result in a loss of Strehl value at the focal planes and achievable contrasts when performing coronagraphy. The most prominent NCPAs are due to atmospheric dispersion, aberrations resulting from optics downstream of the HOWFS&C loop, and changes in alignment within MagAO-X. Atmospheric dispersion causes chromatically varying starlight to be spatially separated on the telescope primary and therefore imaged slightly differently through the optics of MagAO-X. Because the

HOWFS&C loop can only receive relatively broadband starlight, the narrow-band corrective abilities of this loop are limited. With this, MagAO-X is subject to many environmental changes when used on-sky, allowing the alignment of the system to change slightly throughout an observing night.

Due to their description of common optical aberrations and application to correcting wavefront errors at small inner working angles, the low order Zernike polynomials as described by Noll [18] are used to describe the NCPA's that the LOWFS&C loop can correct for. Not including piston, the first 10 low order Zernike modes include tip, tilt, defocus, astigmatism (oblique and vertical), coma (vertical and horizontal), trefoil (vertical and oblique), and spherical. The number of actuators needed to correct a given Zernike mode index is approximately 1:1, similar to that of a Fourier basis. This means to correct the first 9 modes, 9 actuators are needed in the DM/pupil plane. Actuators add in 2-dimensional space, so this results in a 3x3 actuator grid. Each actuator goes with 1 λ/D unit, meaning the wavefront sensor needs a $3^2 (\lambda/D)^2$ image plane to capture the information from the first 9 modes. If a sensor has 2 pixels per λ/D , this means a 6x6 pixel image plane is needed for sensing the first 9 modes. The science cameras have ~4 pixels per λ/D meaning a 16x16 pixel image is needed for detection of the first 10 Zernike modes (though the 4x4 actuator grid allows for correction of up to 16 modes). Camlowfs has ~6 pixels per λ/D , meaning a 24x24 pixel image is needed.

Both science cameras and camlowfs can be used to perform focal plane LOWFS&C, depending on what is useful to an observer. However, due to phase degeneracy with even electric fields at a symmetric pupil plane, either an asymmetrical aperture or an induced even pupil phase (like defocus or astigmatism) is required for focal plane LOWFS&C [19]. Both science cameras and camlowfs are on longitudinally translatable stages with defocusing capabilities up to

~30mm. Because of this, inducing defocus is the preferred method to eliminate phase degeneracy issues without the need to introduce additional components into MagAO-X.

Defocusing the wavefront sensing camera indicates that for LOWFS&C to be implemented during a non-coronagraphic science observation, only one of MagAO-X's two science cameras would be available for in-focus science data acquisition. This is not often the desired case as many science cases require simultaneously imaging at two different spectral bands. However, it is useful to use LOWFS&C on a science camera prior to the start of the observation to set an NCPC DM flat that will clean up static and quasi-static NCPAs. With this, a filter relevant to the science observation can be used to perform the LOWFS&C loop, improving on the broader-band HOWFS&C corrections. If the stellar target is bright enough it can be used to set the NCPC DM flat, otherwise a nearby bright target can be used.

When performing HCI, the reflected spot from the coronagraphic mask can be defocused for LOWFS&C without disturbing science acquisition. A high-level depiction on how the classical Lyot coronagraph has been set up to allow for this in MagAO-X is shown in Figure 6.

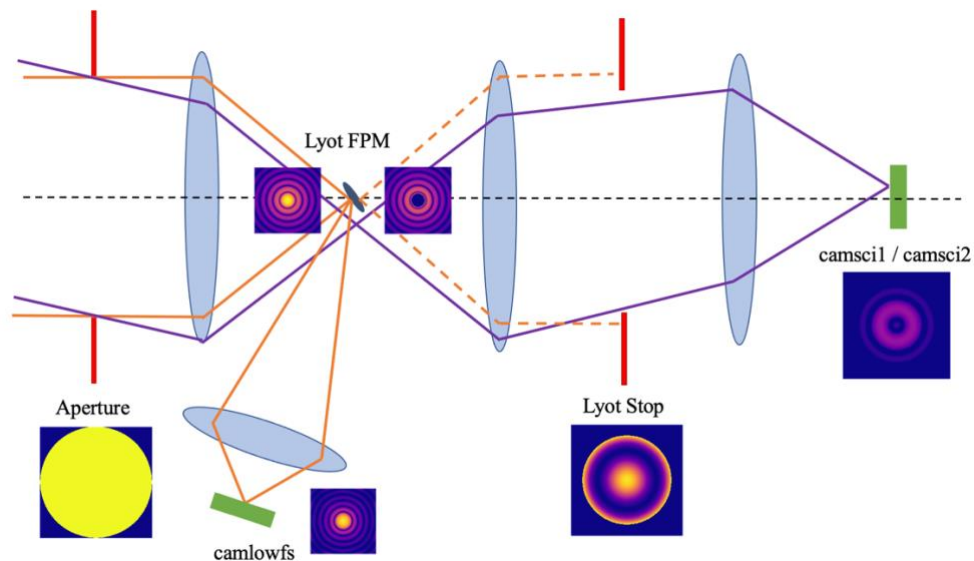


Figure 6. Schematic showing reflected light off Lyot focal plane mask (FPM) reimaged to camlowfs for CLOWFS&C.

The reflected spot off the tilted FPM is imaged to camlowfs for coronagraphic LOWFS&C (CLOWFS&C). Because the FPM is tilted, the reflected beam will be slightly elliptical but does not affect the ability for LOWFS&C to work on MagAO-X. Recall that MagAO-X has two FPMs, one of those being $6 \lambda/D$ in diameter and the other $10 \lambda/D$ in diameter. The $6 \lambda/D$ spot allows for CLOWFS&C of up to 36 low order modes as this is the spot size imaged to the WFS (given proper pixel dimensions on the WFS). Likewise, the $10 \lambda/D$ spot allows for CLOWFS&C of up to 100 low order modes but eliminates the ability to detect faint companions within $5 \lambda/D$.

3 Theory

3.1 The Fourier description of beam propagation in MagAO-X

The relationship between pupil and focal planes must be understood to relate DM corrections to focal plane WFS images. MagAO-X is a near diffraction limited system with large imaging F/#s so Fraunhofer diffraction is used to explain this relationship. Furthermore, the Fraunhofer description for imaging the real components of an electric field from a pupil to a focal plane by lens or reflective element is mathematically equivalent to the Fourier transform (FT), given for two-dimensions as [20]:

$$F(\xi, \eta) = FT[f(x, y)] = \int_{-\infty}^{\infty} \int_{-\infty}^{\infty} f(x, y) e^{-i2\pi(\xi x + \eta y)} dx dy$$

where $F(\xi, \eta)$ is the Fourier transform of $f(x, y)$.

Likewise, the translation of a focal plane image to pupil plane image is given by the inverse Fourier transform (IFT) [20]:

$$f(x, y) = IFT[F(\xi, \eta)] = \int_{-\infty}^{\infty} \int_{-\infty}^{\infty} F(\xi, \eta) e^{i2\pi(\xi x + \eta y)} d\xi d\eta$$

An electric field in the pupil plane E_P is comprised of an amplitude component $A(x,y)$ and phase component $\theta(x,y)$:

$$E_P(x, y) = A(x, y)e^{i\theta(x,y)} = A(x, y) \cos[\theta(x, y)] + iA(x, y)\sin[\theta(x, y)]$$

The electric field in the focal plane E_F is thus given as:

$$E_F(\xi, \eta) = FT[E_P] = a(\xi, \eta) + ib(\xi, \eta)$$

where a and b are functions generally comprised of $FT[A(x, y) \cos[\theta(x, y)]]$ and $FT[iA\sin[\theta(x, y)]]$. An optical system can only image the intensity of light at the focal plane I_F , otherwise considered its PSF (note that coordinate plane indications have been dropped):

$$I_F = |E_F|^2 = |a|^2 + |b|^2$$

To illustrate an example of pupil-to-focal plane imaging, a perfect circular aperture with radius r and electric field with uniform phase (plane wave) is transformed to the focal plane. In this example, the aperture, wave amplitude, and wavelength are all normalized. The aperture is described by the cylinder function:

$$Cyl(x, y) = \begin{cases} 1 & \text{when } \sqrt{x^2 + y^2} \leq r \\ 0 & \text{when } \sqrt{x^2 + y^2} > r \end{cases}$$

Because the field at the pupil is a uniform, the focal plane image is simply the Fourier transform of the aperture function. The well-known Fourier transform for the cylinder function is the Bessel function of the first kind. When imaged with an optical system, this is known as an airy pattern or an ideal PSF.

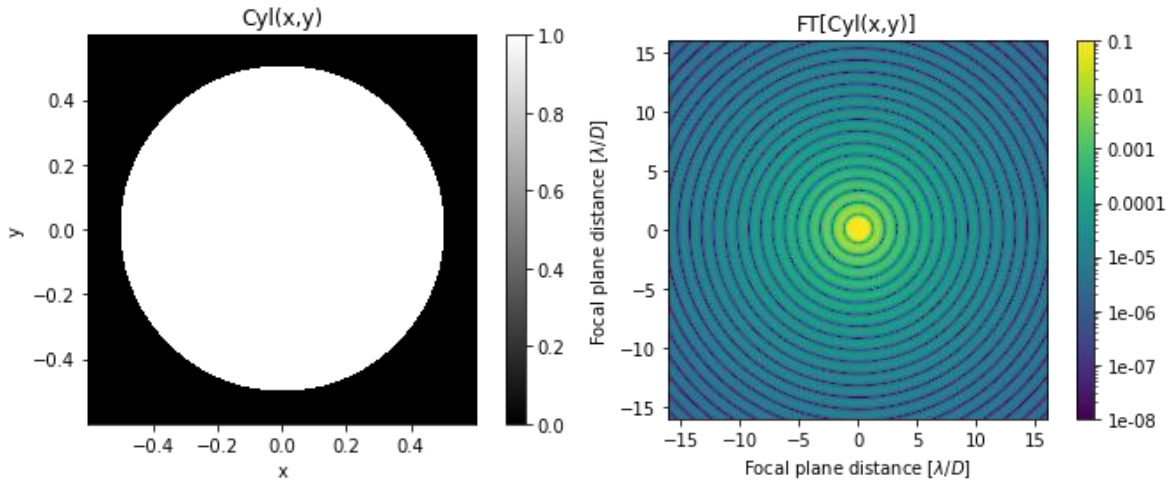


Figure 7. Simulation of perfect circular aperture showing Fraunhofer propagation to a focal plane.

As mentioned, Fraunhofer propagation is used to model beam propagation through MagAO-X for simulating LOWFS&C. Recall that DM and aperture planes are in pupil space, and image planes are located in focal plane space. The slightly more complex aperture of the Magellan Clay 6.5 m telescope is modeled:

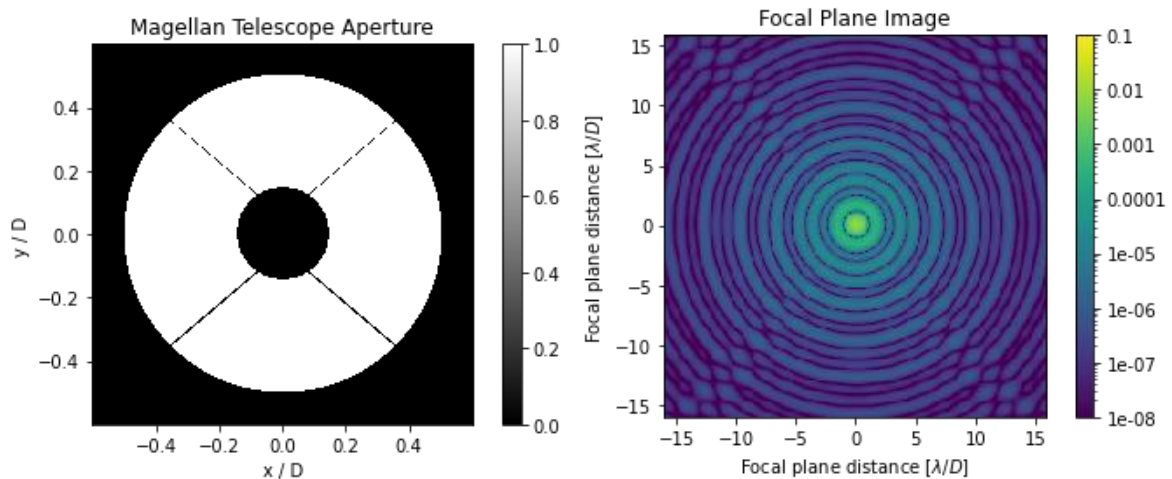


Figure 8. Simulation showing Fraunhofer propagation of normalized Magellan telescope aperture.

The Fraunhofer relationship is also used to describe the propagation of a uniform electric field $E(x,y)$ through the Lyot coronagraph on MagAO-X. The propagation to the science cameras

on MagAO-X with telescope aperture function $P(x,y)$, Lyot FPM $M(\xi,\eta)$, and Lyot stop $S(x,y)$ is given as:

$$\text{Field at Lyot FPM} = E_{focal\ 1}(\xi,\eta) = FT[P(x,y)]$$

$$\text{Transmitted field at Lyot FPM} = E_{focal\ T}(\xi,\eta) = E_{focal\ 1}(\xi,\eta) \cdot M(\xi,\eta)$$

$$\text{Field at Lyot stop} = E_{pupil}(x,y) = IFT[E_{focal\ T}(\xi,\eta)]$$

$$\text{Transmitted field at Lyot stop} = E_{pupil\ T}(x,y) = E_{pupil}(x,y) \cdot S(x,y)$$

$$\text{High contrast focal plane field} = E_{focal\ 2}(x,y) = FT[E_{pupil\ T}(x,y)]$$

The propagation to camlowfs is given as:

$$\text{Reflected field at Lyot FPM} = E_{focal\ R}(\xi,\eta) = E_{focal\ 1}(\xi,\eta) \cdot [1 - M(\xi,\eta)]$$

$$\text{Field at WFS imaging lens} = E_{pupil\ R}(x,y) = IFT[E_{focal\ R}(\xi,\eta)]$$

$$\text{WFS focal plane field} = E_{focal\ 3}(x,y) = FT[E_{pupil\ R}(x,y)]$$

3.2 The Phase Degeneracy Problem

For a focal plane intensity profile $I_F = |a|^2 + |b|^2$, the focal plane phase ϕ is given as:

$$\phi = \frac{b}{a}$$

Because a and b are not known independently when imaging I_F , directly sensing the pupil plane phase at the focal plane is not possible. This is known as the phase degeneracy problem. A pupil phase aberration (mode) can still be corrected through focal plane wavefront sensing if certain symmetry properties of Fraunhofer diffraction are met, though these properties are not met with all low order modes the LOWFS&C loop aims to correct for on MagAO-X.

A function $f(x)$ is even if and only if $f(-x) = f(x)$ and odd if and only if $f(-x) = -f(x)$. Even low order Zernike phase polynomials (defined in pupil space) include defocus, astigmatism

(oblique and vertical), and spherical aberrations. Figure 9 shows examples of these with positive and negative phase components.

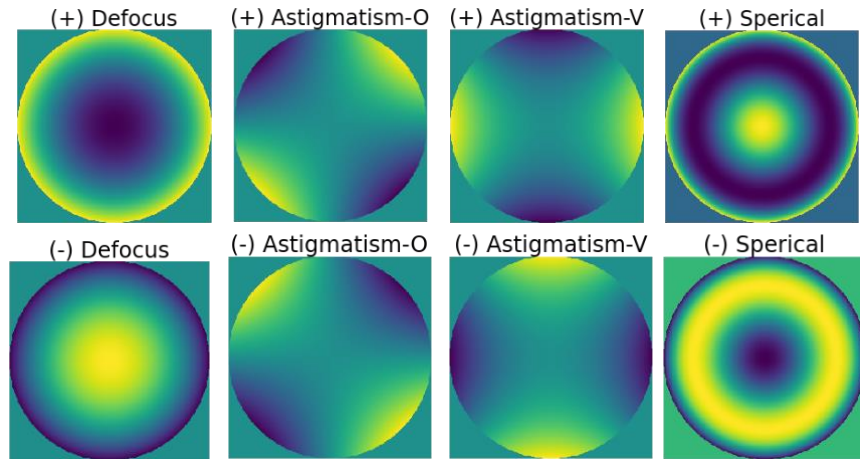


Figure 9. Even low order phase aberrations in the pupil plane with positive and negative phase components [$iA\sin(\theta)$] and uniform amplitude components [$A\cos(\theta)$].

Odd low order Zernike phase polynomials include tip/tilt, coma (vertical and horizontal), and trefoil (vertical and oblique). Figure 10 shows examples of these with positive and negative phase components.

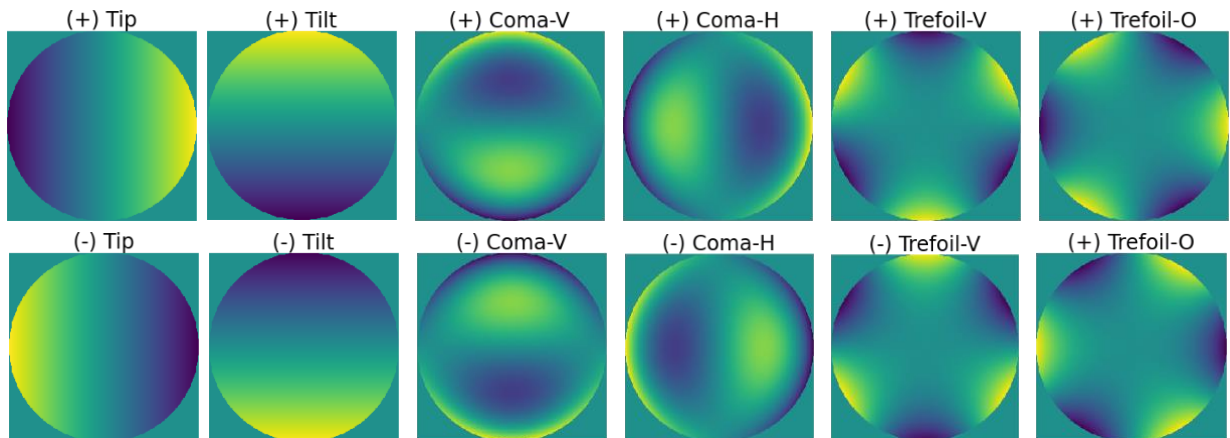


Figure 10. Odd low order phase aberrations in the pupil plane with positive and negative phase components [$iA\sin(\theta)$] and uniform amplitude components [$A\cos(\theta)$].

The symmetry properties of Fraunhofer propagation state that a pupil plane electric field E_P with even amplitude and phase will result in a PSF that is also even [20]. Because the Fourier

transform is a Hermitian operator, if a pupil plane electric field is conjugated E_P^* , the focal plane electric field will be flipped and conjugated:

$$E_P^* = Ae^{-i\theta}$$

$$FT[E_P^*] = E_F^*(-r)$$

In other words, the PSF will flip, but because it is even there will be no detectable change in the intensity seen by the optical system. An example is given for vertical astigmatism in Figure 11.

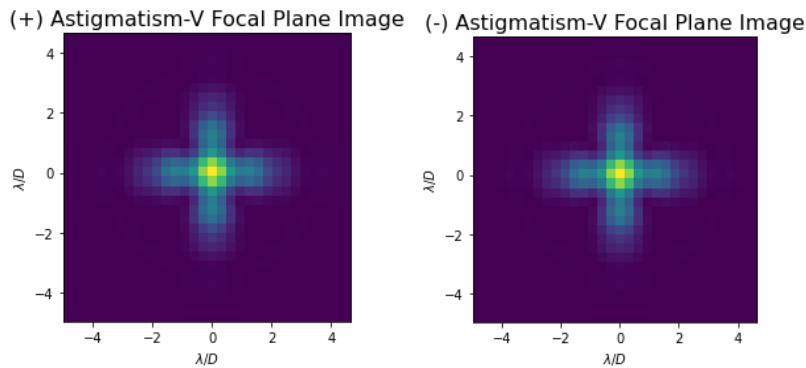


Figure 11. Example of +/- vertical astigmatism at a focal plane.

Conversely, the properties of Fraunhofer propagation state that if either the amplitude or phase component of E_P are odd, the resulting PSF will be odd [20]. If the sign of the phase component in the pupil electric field is then flipped, the morphology of the PSF will change.

Figure 12 shows this property for vertical trefoil.

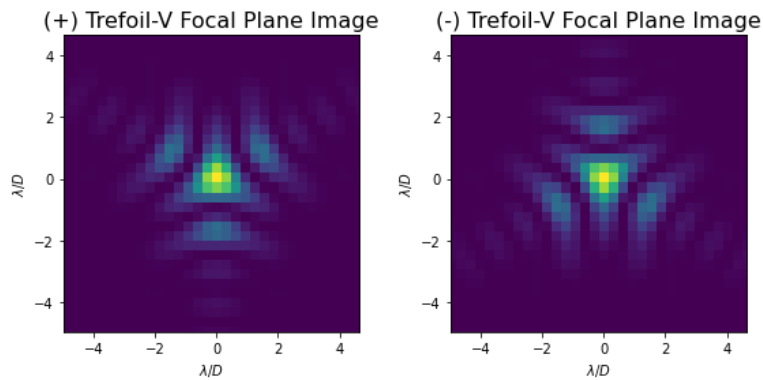


Figure 12. Example of +/- vertical trefoil at a focal plane.

To perform WFS&C of even modes, either the amplitude or phase component needs to be manipulated such that the real part of the electric field is probed and therefore creates uneven symmetry in the PSF. Two ways of doing this are:

1. Introducing an uneven aperture at the pupil.
2. Introducing an even phase aberration at the pupil.

Because Zernike defocus can be produced by physically moving the location of a WFS, this method of probing the real part of the electric field is easily implemented with MagAO-X.

Examples for defocused WFS images for vertical astigmatism and vertical trefoil are seen to have clear morphology changes in Figure 13.

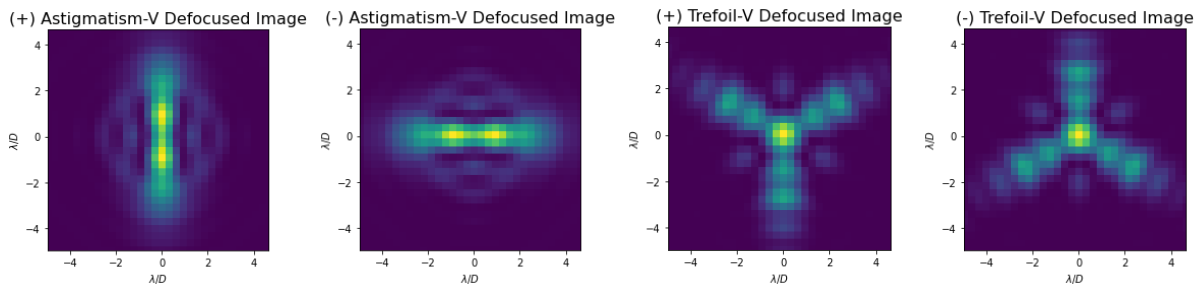


Figure 13. Example of +/- vertical astigmatism and vertical trefoil at a defocused image plane.

3.3 Linear wavefront sensing and control

LOWFS&C on MagAO-X is implemented with a linear control algorithm, meaning that it relies on a linear relationship between changes in electric field amplitudes in the pupil plane and electric field changes in the focal plane. Recall that what is sensed by an optical system at the focal plane goes with the FT^2 of the pupil plane. To create an approximately linear relationship between the pupil and focal planes, the aberrated focal plane image must be ideal-PSF (reference) subtracted. This approximation is valid when changes in OPL induced by wavefront errors in the pupil plane are very small (sub-wavelength). Figure 14 shows the

amplitude response for focal plane image pixels with increasing RMS probe amplitudes of astigmatism added to the DM.

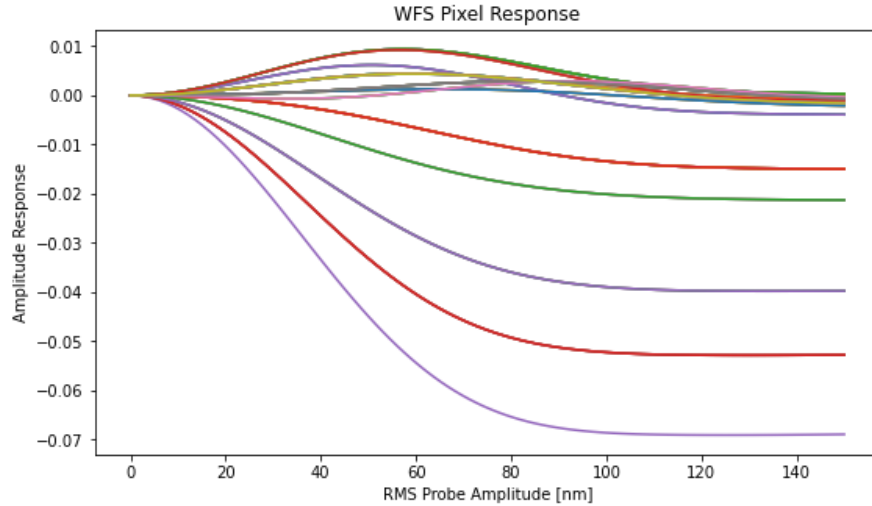


Figure 14. Simulation of pixel responses within a $1.5 \lambda/D$ radius on a MagAO-X science camera in $H\alpha$ when $0 \text{ nm} - 150 \text{ nm}$ RMS astigmatism phase error is added to the DM.

For the dynamic range in which a linear response in the focal plane is upheld, the following linear algorithm can be used for LOWFS&C:

$$Dv = s$$

D is the interaction (response) matrix between the DM and the WFS and is created by calibrating the loop for a given set of input parameters and modal basis. In other words, this response matrix must be determined before a LOWFS&C loop is closed and defines what the LOWFS&C loop will be able to identify and correct. The correction vector v contains the commands sent to the DM when actively sensing modes in the image plane. Finally, s is the wavefront measurement vector and contains all pixel values for a given modal response at the WFS. Solving this system provides the least squares solution for wavefront correction. When using a LOWFS&C loop in practice, the system is solving for the correction vector so that correction coefficients are applied to the DM modal basis. Therefore, the pseudoinverse of the response matrix (considering D is often a non-square matrix) $R = D^{-l}$ must be found. This is known as the reconstruction matrix.

$$v = Rs$$

For a focal plane image with a region of interest (ROI) of size $(n \times n)$ and correction of k modes, the sizes of each of these components are as follows:

$s \rightarrow [n^2 \times 1]$ This is a column vector resulting from stacking each column of the WFS image.

$D \rightarrow [n^2 \times k]$ This stores the WFS shape for a given mode.

$R \rightarrow [k \times n^2]$ This is the pseudoinverse of D .

$v \rightarrow [k \times 1]$ This stores the modal amplitudes applied to the modal basis used to train the loop.

As stated, the response matrix will only provide accurate WFS&C when the pupil/DM plane amplitudes result in a linear response in the focal/WFS plane. This implies that when linearity is not upheld, the control loop will provide inaccurate corrections and can drive the PSF into a state worse than when the loop was open (no correction loop initiated). In practice, this can occur when atmospheric turbulence causes the aberrated phase amplitudes at the DM to be too large to correct.

4 Modeling

4.1 Modeling MagAO-X LOWFS&C calibrations in Python

To model LOWFS&C performance on MagAO-X and ultimately optimize defocus location, a simulation was created in Python. This model communicates defocus in mm of the cameras in MagAO-X to a shift in the focal plane of the simulation. The Fraunhofer propagator was used to relate DM shapes to wavefront sensor images for perfectly monochromatic inputs. A phase shift defined by the defocus Zernike polynomial was induced at the DM to compensate for a longitudinal defocus of the WFS [21]. Figure 15 depicts this relationship, indicating in orange where the simulated image plane will result when using Fraunhofer propagation on a uniform

pupil phase versus a Zernike defocus pupil phase. The simulated defocus amount, which is the distance a camera would be moved on its translation stage within MagAO-X, is indicated in blue. This is the user-chosen value used to find the shape of the Zernike defocus polynomial at the pupil plane for simulation, and is ultimately what is optimized for LOWFS&C performance on MagAO-X.

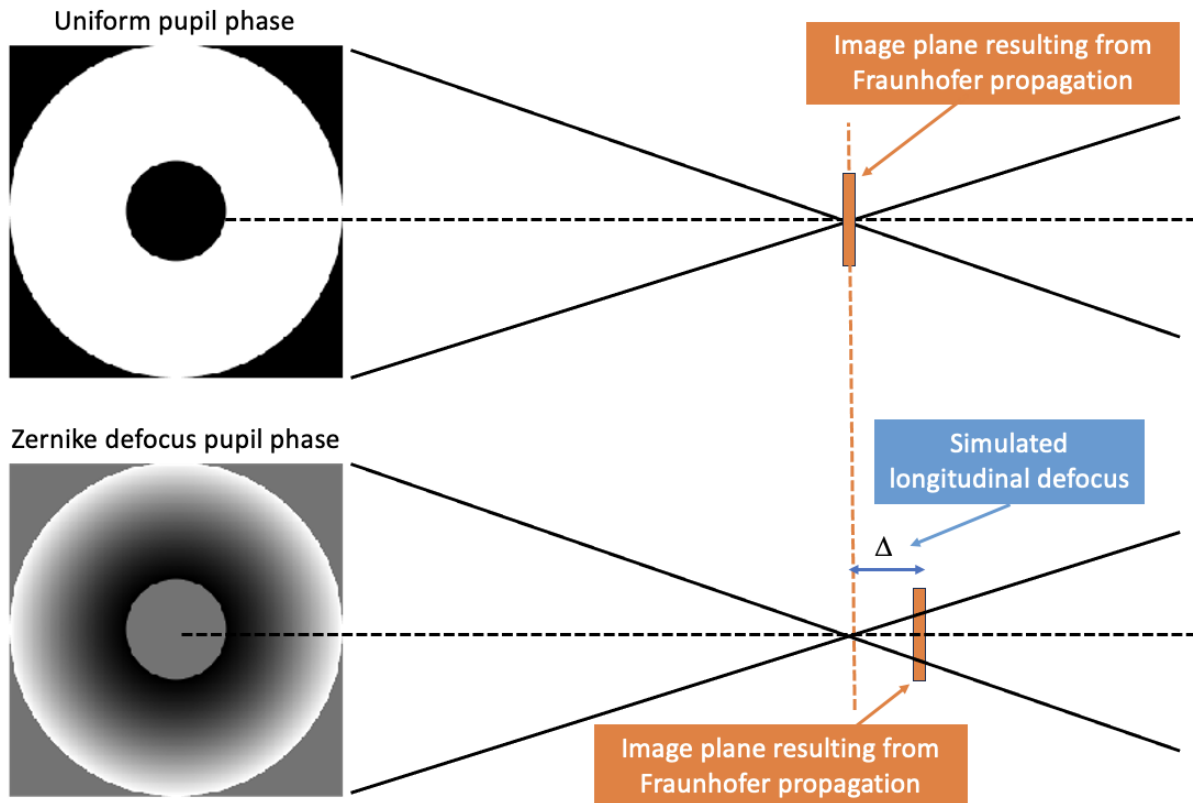


Figure 15. Depiction of a longitudinal defocus shift when applying Zernike defocus to the pupil plane.

The known parameters of the system include the longitudinal defocus amount Δ , F-number F , and wavelength λ . The peak to valley error P in the pupil plane resulting from a focal plane shift Δ is given as:

$$P[m] = \frac{-\Delta}{8 * F^2}$$

The RMS wavefront error w is then given as:

$$w [m] = \frac{P}{\sqrt{12}}$$

The RMS phase error Z_ϕ is calculated by multiplying w by a factor of $\frac{2\pi}{\lambda}$:

$$Z_\phi [rad] = w * \frac{2\pi}{\lambda}$$

The Zernike aberration term for defocus $Z_{defocus}$ can be found with the RMS phase error and normalized radial position on the DM:

$$Z_{defocus} [rad] = \sqrt{3}(2\rho^2 - 1)Z_\phi$$

$$0 < \rho < 1$$

$Z_{defocus}$ is added as a phase apodizer in the pupil plane of the simulation for a given Δ value and known camera/filter configuration. This accuracy of the model was confirmed using camsci1 on MagAO-X in z-band. The top row of Figure 16 contains camsci1 images and the bottom row contains simulated camsci1 defocus images. The defocus amounts from left to right are 0 mm, 20 mm, 30 mm, and 50 mm.

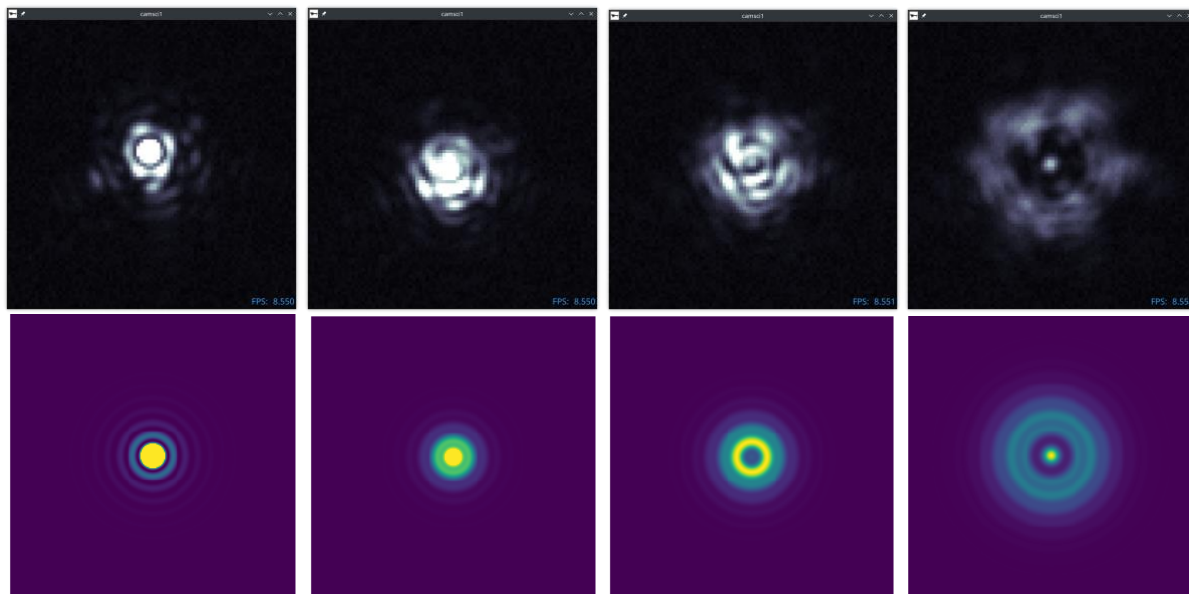


Figure 16. Testing defocus modeling with MagAO-X in z-band.

The necessary components for modeling a LOWFS&C loop include a DM, a linearly independent mode basis defined at the DM/pupil plane (Zernike modes used here), and a linear control algorithm with respect to the defocused pupil plane. Figure 17 gives a summary of the steps taken to train the LO loop at a given defocused image plane (run a model calibration).

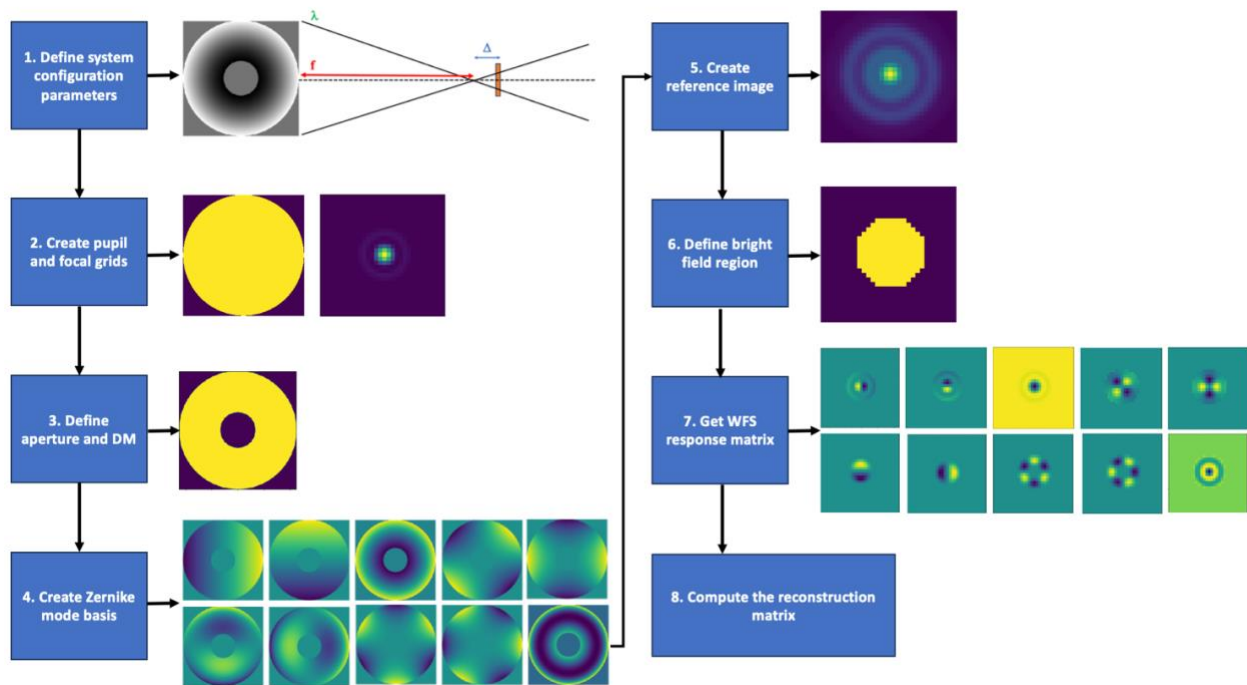


Figure 17. LOWFS&C calibration model summary.

The following is a break-down of each step shown in Figure 17 (see Appendix A for LOWFS&C simulation Python code).

1. Define system configuration parameters.
 - a. Wavelength
 - b. F/#
 - c. Defocus amount [mm]
 - d. Pixel pitch
2. Create pupil and focal grids using input parameters.

- a. Pupil grid is set to 256 x 256 pixels for efficient sampling. Using smaller grid sizes (64 x 64) created sampling effects in the focal plane images that do not reflect what it seen on MagAO-X and added significant inaccuracy to the model. Using larger grid sizes (1024 x 1024) did not cause significant change in WFS images indicating there was no need for the increase in computing expense for model accuracy.
 - b. Focal grids are set to 32x32 to reflect the true region of interest (ROI) size used for calibrating on MagAO-X. This image size was determined through testing preliminary calibrations on MagAO-X, providing the necessary number of λ/D units for the required modal corrections. By keeping the ROI small, the cameras have the capability to run at faster speeds and therefore perform LOWFS&C at higher correction rates.
3. Define obstructed aperture and DM at pupil plane.
 4. Create Zernike mode basis defined at the DM plane.
 - a. The DM modal basis ($k=10$) is shown in Figure 18. By index, these include tip (0), tilt (1), defocus (2), oblique astigmatism (3), vertical astigmatism (4), vertical coma (5), horizontal coma (6), vertical trefoil (7), oblique trefoil (8), and spherical (9).

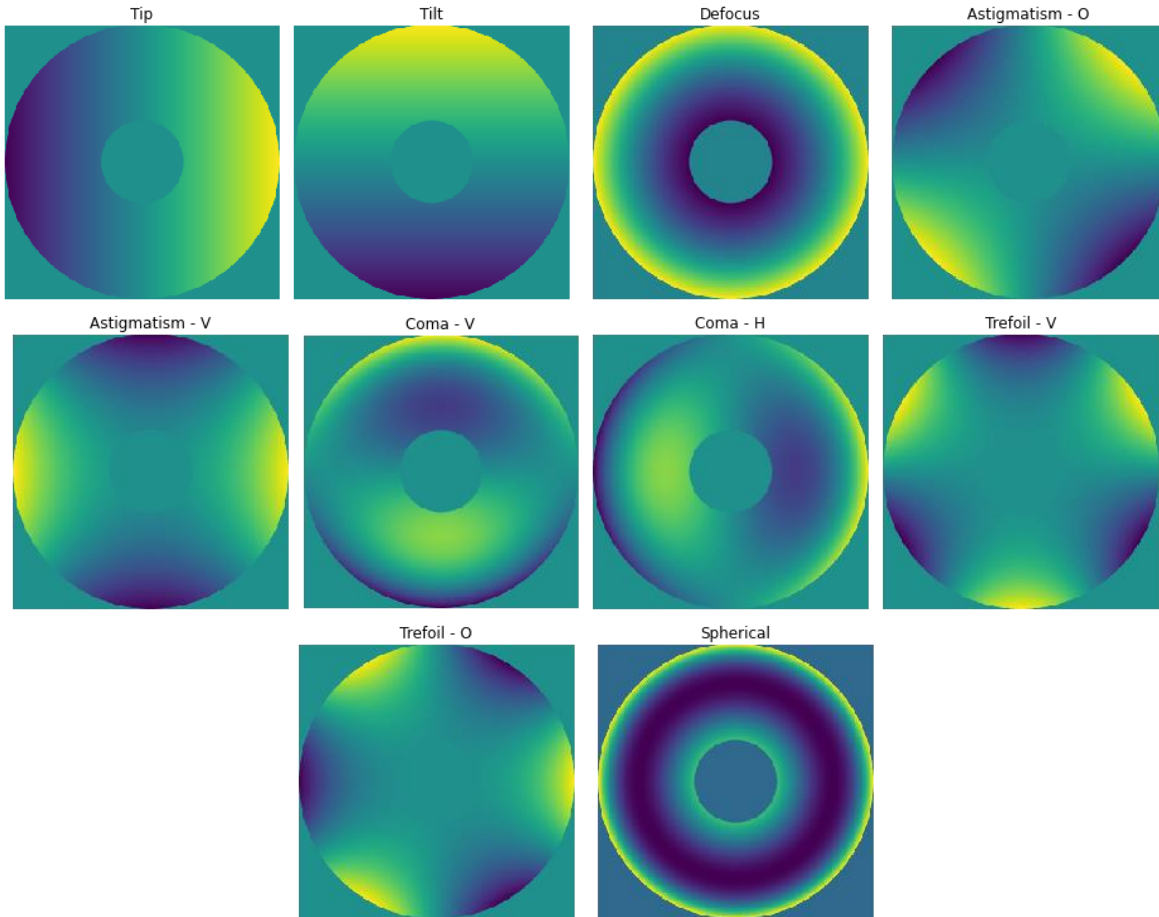


Figure 18. Modeled Zernike mode basis in the pupil plane with the obstructed aperture.

5. Propagate flat wavefront to defocused image plane and take the reference image. This image will be subtracted from all modal response images at the WFS for calibration and closed loop operation (provides modal response vector s). When calibrating on MagAO-X, this image should be as close to the ideal defocused PSF as possible as it defines the maximum achievable image quality when implementing the LOWFS&C loop.

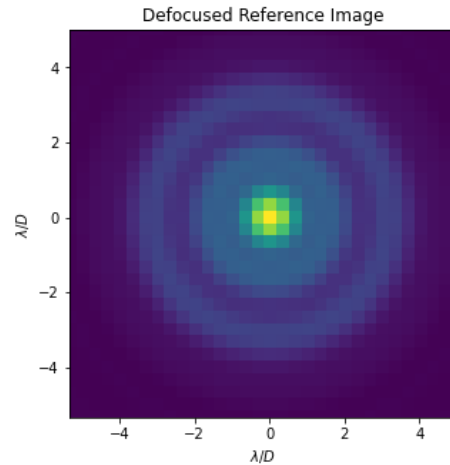


Figure 19. Example of modeled defocused reference image.

6. Define a ‘bright field’ pixel region in the focal plane image to be used for modal control.
 - a. A bright field (BF) mask is used to eliminate the use of non-linearly responding pixels in the WFS image. In simulation, the BF mask is set to include all pixels within a $2 \lambda/D$ radius, as this will allow for calibration of all 10 low order Zernike modes and eliminates the use of dark field (DF) signal.

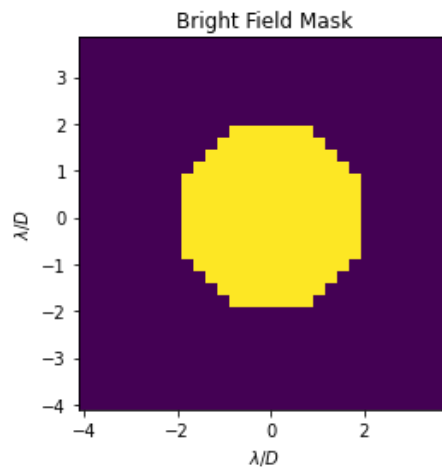


Figure 20. Example of modeled BF mask.

7. Poke the DM with each Zernike mode at an RMS probe amplitude of +10 nm and -10 nm. This is the amplitude component $A(r)$ of E_P and is chosen such that the response stays well within the linear range and produces a sufficiently strong response signal. The

reference image is subtracted from both images, and the resulting (+) response image is subtracted from the (-) response image. The differential image is normalized by twice the probe amplitude. The final normalized image for each mode is then stored as a column vector to the response matrix D . An example WFS response set is given in Figure 21.

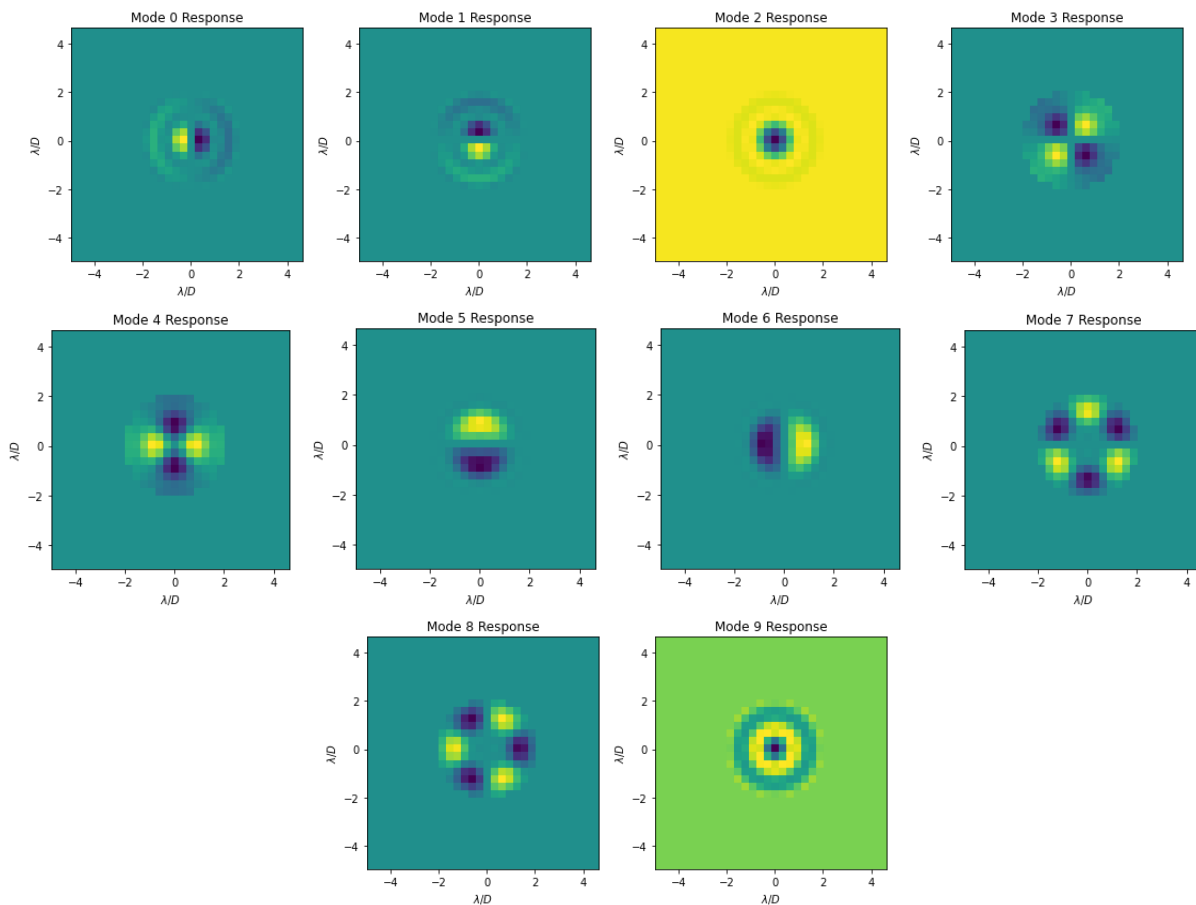


Figure 21. Modeled example of WFS modal response basis.

8. Take the inverse of D to find the reconstruction matrix R .
 - a. Tikhonov regularization is used with a $1e-5$ relative strength condition to find R .

4.2 Optimization metrics

To test the performance of a modeled calibration, the DM is poked with the same 10 Zernike phase aberrations used to train the model at a poke amplitude equal to twice the training probe amplitude. The dot product of the calibrated reconstruction matrix and reference

subtracted WFS image is used to find the set of modal coefficients (correction vector ν). This is applied to the DM mode basis and applied to the DM to correct the wavefront. Gain and leakage parameters are set to 1 for the simulation as to predict ideal responses. Gain refers to a local or global multiplier on the correction vector typically used to lower the magnitude of the correction when using LOWFS&C in lab or on-sky with MagAO-X. Leak is another multiplier and is used to dampen the corrective shape on the DM prior to applying the correction vector. This parameter is also typically adjusted on-sky or in the lab based on a loop's tendency to diverge. Leak is usually set between 0.95 and 1 where lower values can allow for loop stability but can also cause inadequate correction as the DM actuators will be too dampened to offer any useful correction. Both adjustments have to do with accounting for the optical gain of the MagAO-X LOWFS&C configuration which is currently uncharacterized. Preliminary findings indicate the optical gains of MagAO-X change over time and is variable with astronomical seeing.

A signal to noise ratio (SNR) metric is used to evaluate simulated calibration performance. To find SNR, the correction vector for each mode response is normalized by twice the probe amplitude, meaning a perfect correction will have a value of 1 at the index corresponding to the modal basis poked at the DM. This can be represented by the self-response matrix (self RM) of the system, which plots the correction vector vs. poke mode index:

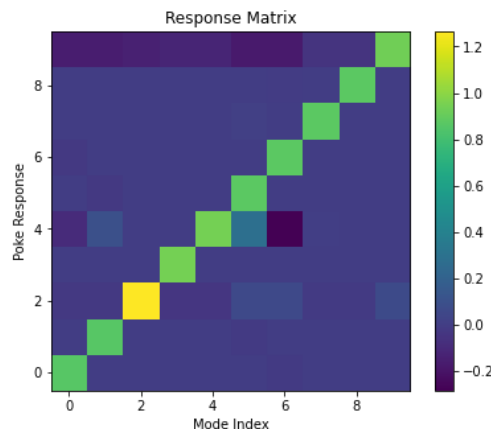


Figure 22. Example self-response matrix for the Zernike mode basis.

All non-zero poke response values at indices other than that of the mode index are referred to as crosstalk, and the sum of the absolute value of these (from the normalized self RM) is the noise. The signal is the sum of all poke responses (from the normalized self RM) at the mode index, or simply the sum of the diagonal. The ratio of these provides the SNR.

It is important to consider that a very high SNR does not necessarily indicate good calibration performance. For example, a signal of 10 could result from perfect reconstruction, or a reconstruction with one mode response along the diagonal that is 10-times the poke amplitude and zeroes elsewhere. Clearly the latter case does not represent a good calibration, so a metric to evaluate deviation from the ideal case is needed. This metric is found by finding the standard deviation σ of the poke responses x along the diagonal with a mean value μ of 1 and k modes:

$$\sigma = \sqrt{\frac{\sum_1^k (x - \mu)^2}{k}}$$

The peak SNR value is reported as the optimal defocus for all camera and filter combinations in the following section. The standard deviation at each focus position is observed to ensure the point of highest SNR does not result from extreme deviations from the ideal case but is not included in the calculation of where optimal defocus is.

4.3 Optimization results

The ideal focus location is found on camlowfs (F/85.53) and the science cameras (F/69) for the H α , r, z, and i filters. It is important to note that the maximum dynamic range for defocusing each of the cameras are 29 mm (camsci1), 30.5 mm (camsci2), and 30 mm (camlowfs). All optimal defocus locations were found with precision to 0.01 mm.

4.3.1 Optimization results for camlowfs

The optimal defocus location, self-RM and reference PSF are given for each filter.

4.3.1.1 The r (615 nm) filter

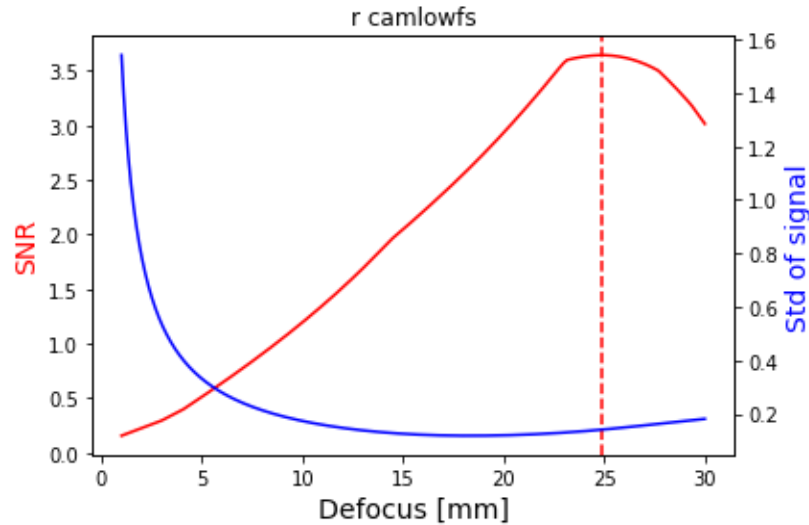


Figure 23. SNR and standard deviation vs camlowfs defocus value in r-band.

Figure 23 indicates that the optimal defocus location for high SNR is 24.89 mm and produces an SNR of 4.27. The standard deviation of the signal indicates good poke response behavior. The reference image and self-RM shown in Figure 24 result from this optimal defocus value.

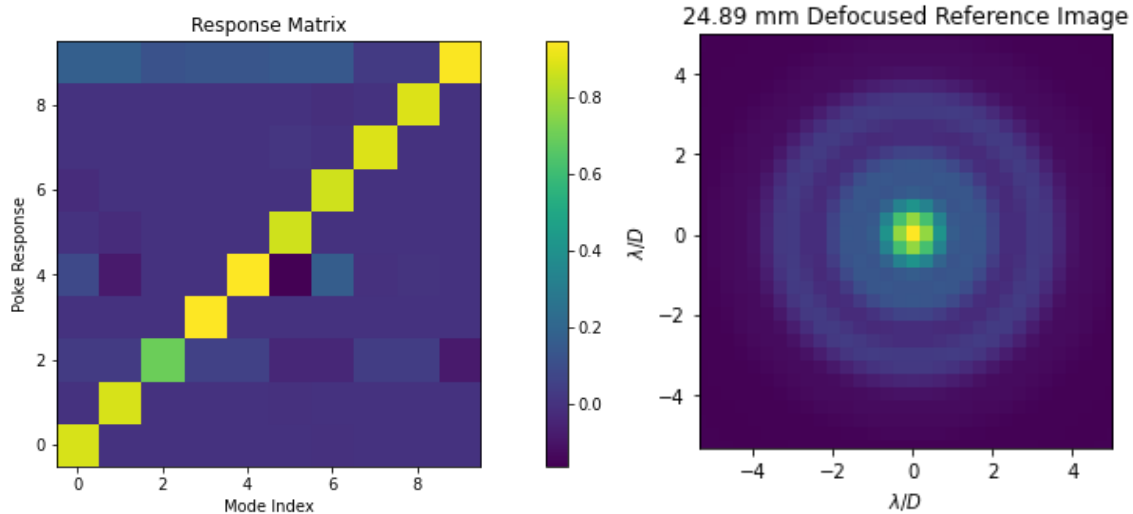


Figure 24. Self-response matrix and ideally defocused PSF for camlowfs in r-band.

4.3.1.2 The $H\alpha$ (656 nm) filter:

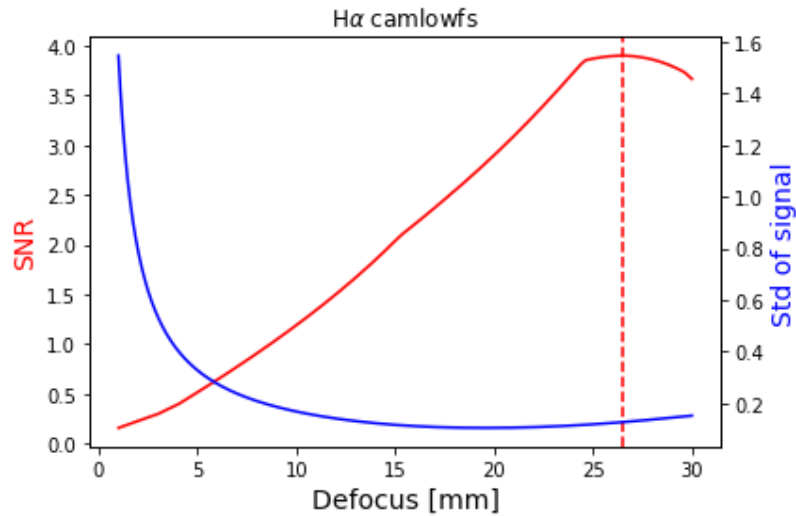


Figure 25. SNR and standard deviation vs camlowfs defocus value in $H\alpha$.

Figure 25 indicates that the optimal defocus location for high SNR is 26.47 mm and produces an SNR of 4.27. The standard deviation of the signal indicates good poke response behavior. The reference image and self-RM shown in Figure 26 result from this optimal defocus value.

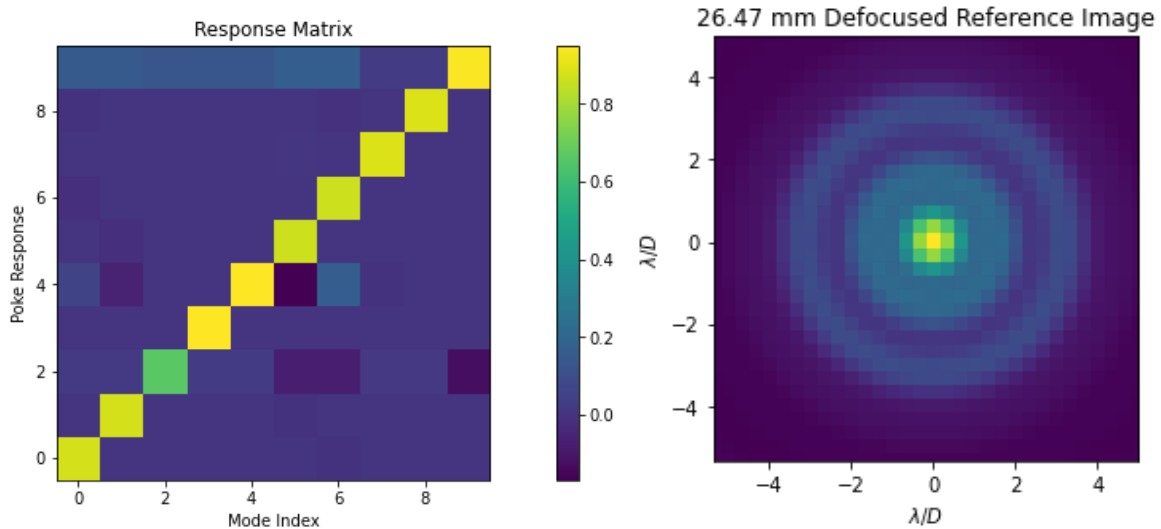


Figure 26. Self-response matrix and ideally defocused PSF in $H\alpha$ on camlowfs.

4.3.1.3 The *i* (762 nm) filter:

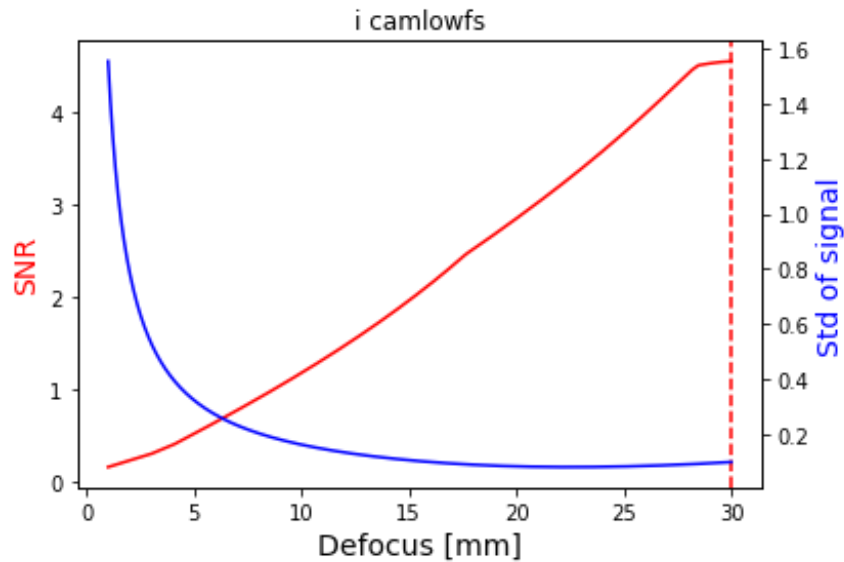


Figure 27. SNR and standard deviation vs camlowfs defocus value for *i*-band.

Figure 27 indicates that the optimal defocus location for high SNR is 30 mm and produces an SNR of 5.37. The standard deviation of the signal indicates good poke response behavior. The reference image and self-RM shown in Figure 28 result from this optimal defocus value.

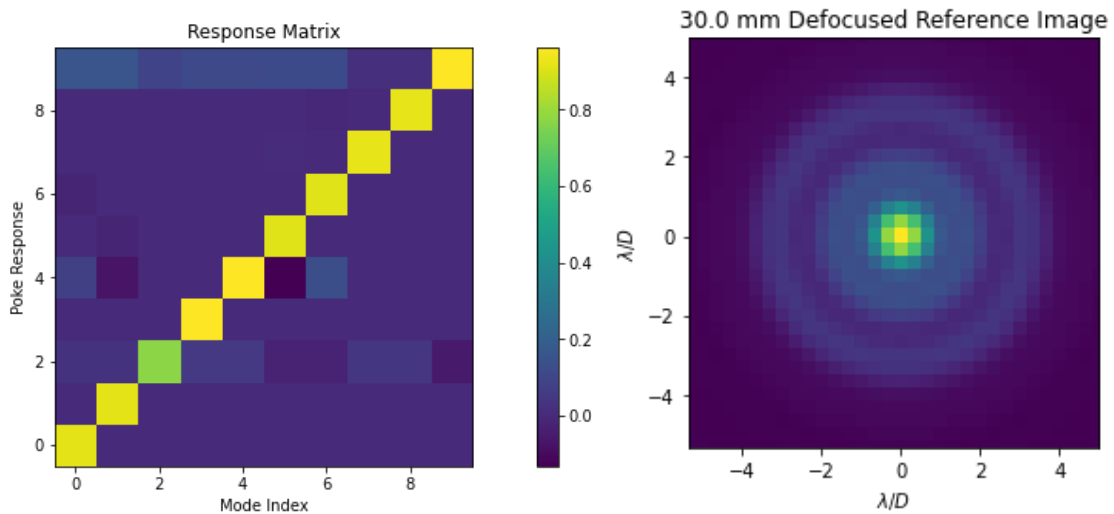


Figure 28. Self-response matrix and ideally defocused PSF for the *i*-band on camlowfs.

It should be noted that the allowable defocus range of camlowfs does not reveal the true local peak of the optimal defocus value in *i*-band.

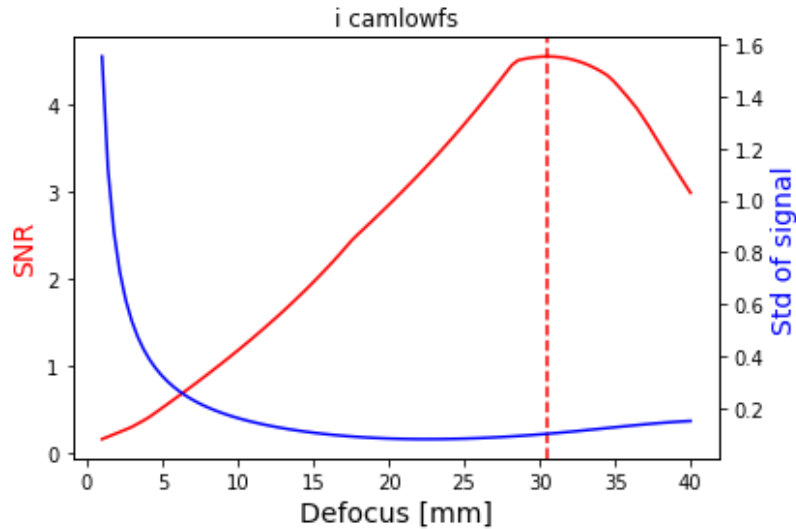


Figure 29. SNR and standard deviation vs. camlowfs defocus value with defocus range extended to 40 mm in i-band.

Figure 29 indicates that an SNR of 5.38 can be achieved by defocusing camlowfs 30.55 mm, though this defocus amount cannot be implemented currently on MagAO-X.

4.3.1.4 The z (909 nm) filter:

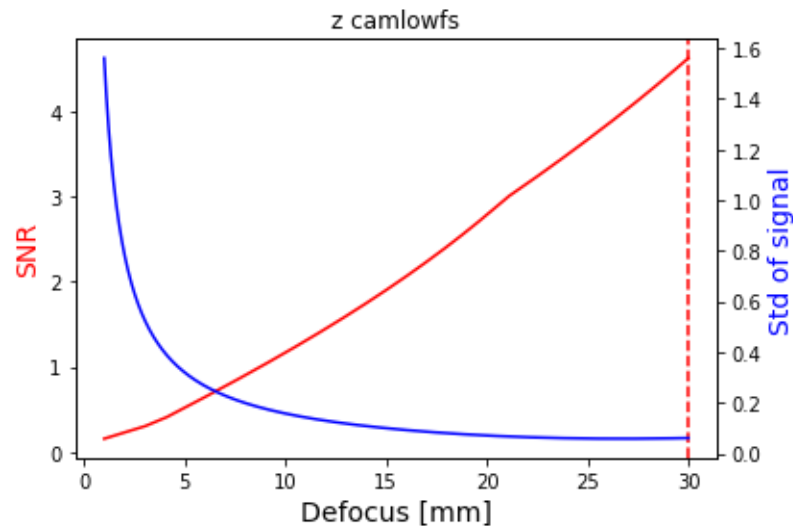


Figure 30. SNR and standard deviation vs camlowfs defocus value in z-band.

Figure 30 indicates that the optimal defocus location for high SNR is 30 mm and produces an SNR of 5.47. The standard deviation of the signal indicates good poke response

behavior. The reference image and self-RM shown in Figure 31 result from this optimal defocus value.

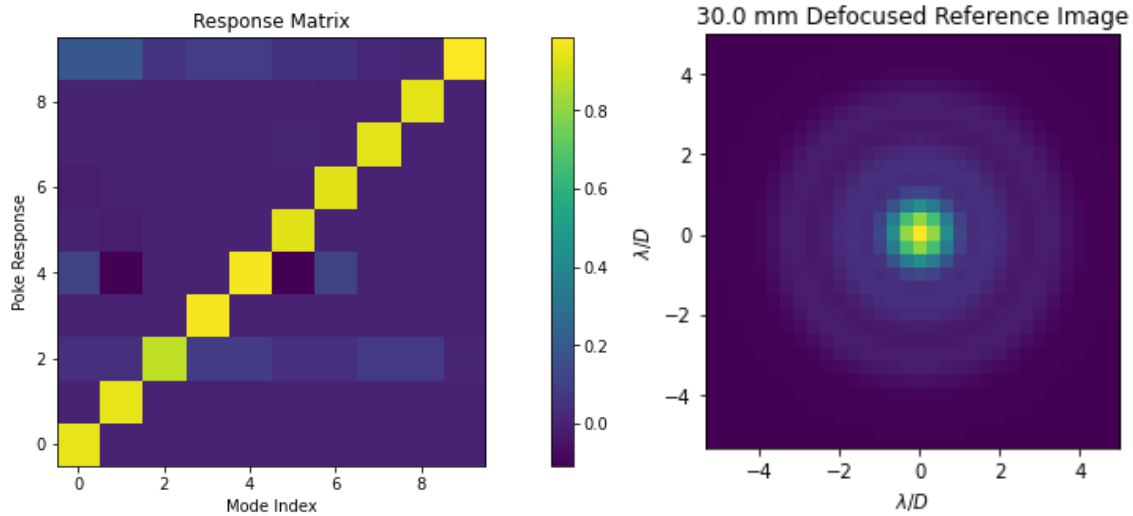


Figure 31. Self-response matrix and ideally defocused PSF z-band on camlowfs.

Again, the allowable defocus range of camlowfs does not allow for the local optimal defocus to be used with LOWFS&C on MagAO-X. Figure 32 shows that a defocus amount of 36.24 would result in an SNR 6.49.

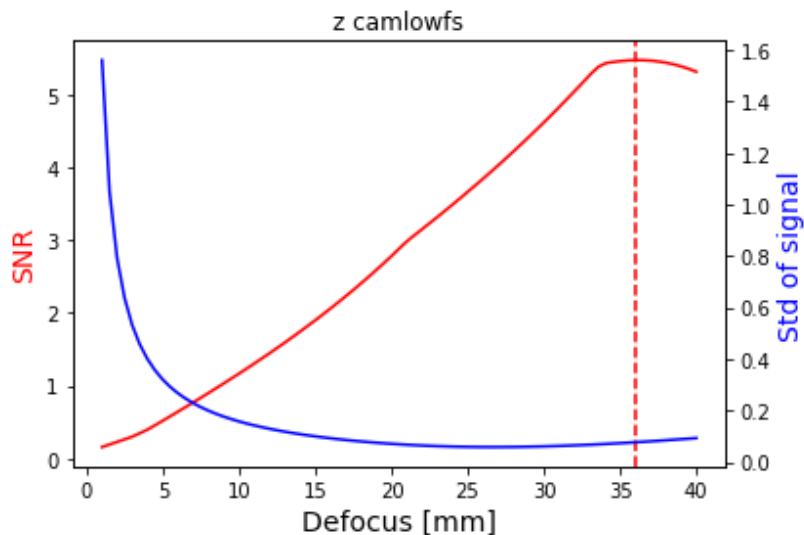


Figure 32. SNR and standard deviation vs. camlowfs defocus value with defocus range extended to 40 mm in z-band.

4.3.2 Optimization results for camsci1 and camsci2

The optimal defocus location, self-RM and reference PSF are given for each filter. Because camsci1 and camsci2 have the same F/#, all of the following results apply to both cameras.

4.3.2.1 The r (615 nm) filter:

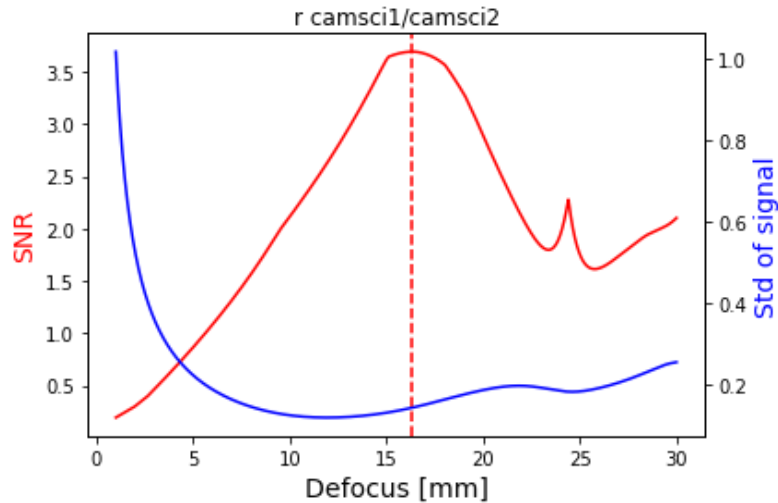


Figure 33. SNR and standard deviation vs camsci1/camsci2 defocus value in r-band.

Figure 33 indicates that the optimal defocus location for high SNR is 16.34 mm and produces an SNR of 4.28. The standard deviation of the signal indicates good poke response behavior. The reference image and self-RM shown in Figure 34 result from this optimal defocus value.

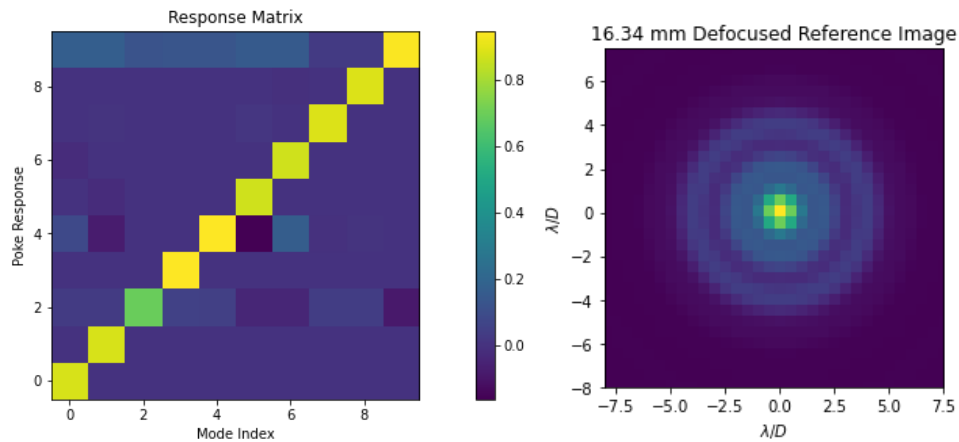


Figure 34. Self-response matrix and ideally defocused PSF in i-band on camsci1/camsci2.

4.3.2.2. The $H\alpha$ (656 nm) filter:

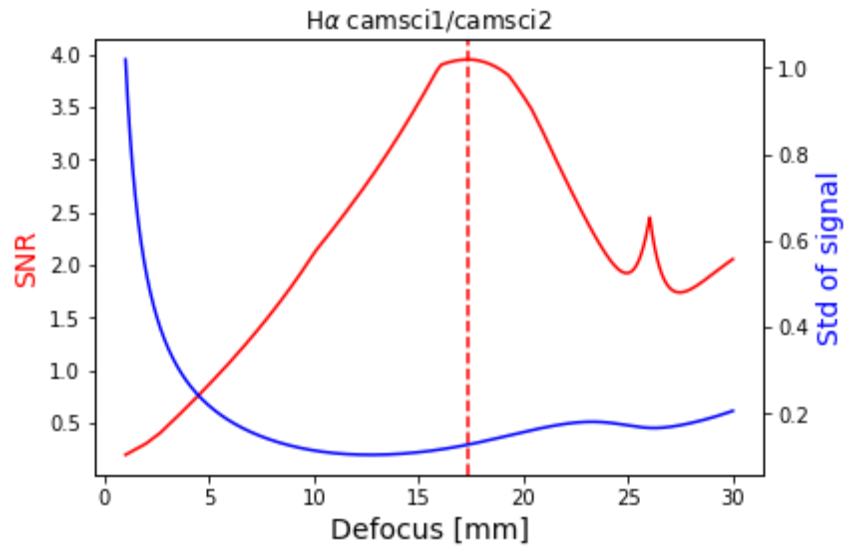


Figure 35. SNR and standard deviation vs camsci1/camsci2 defocus value for the $H\alpha$ filter (656 nm).

Figure 35 indicates that the optimal defocus location for high SNR is 17.37 mm and produces an SNR of 4.59. The standard deviation of the signal indicates good poke response behavior. The reference image and self-RM shown in Figure 36 result from this optimal defocus value.

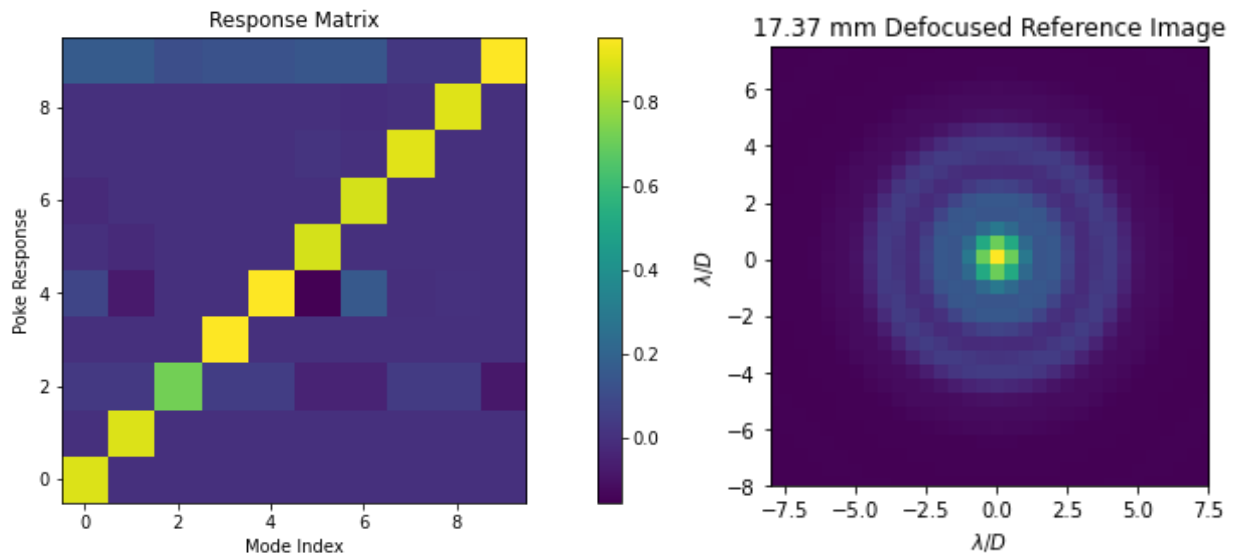


Figure 36. Self-response matrix and ideally defocused PSF in $H\alpha$ on camsci1/camsci2.

4.3.2.3 The i (762 nm) filter:

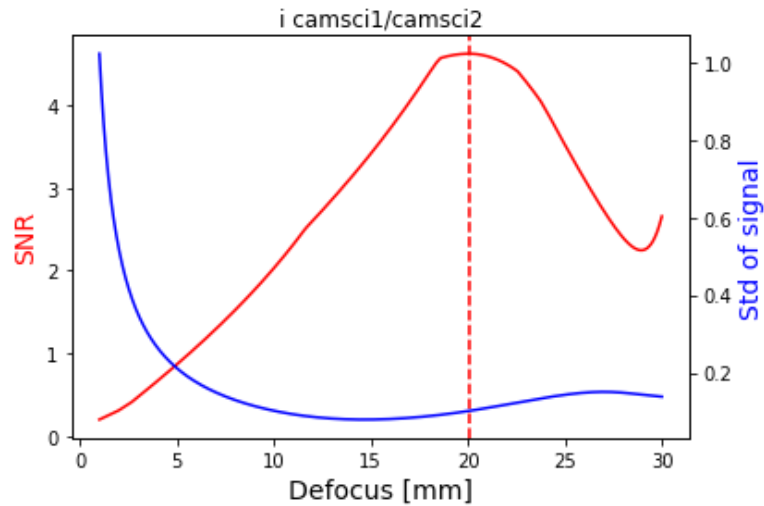


Figure 37. SNR and standard deviation vs camsci1/camsci2 defocus value in i -band.

Figure 37 indicates that the optimal defocus location for high SNR is 20.05 mm and produces an SNR of 5.39. The standard deviation of the signal indicates good poke response behavior. The reference image and self-RM shown in Figure 38 result from this optimal defocus value.

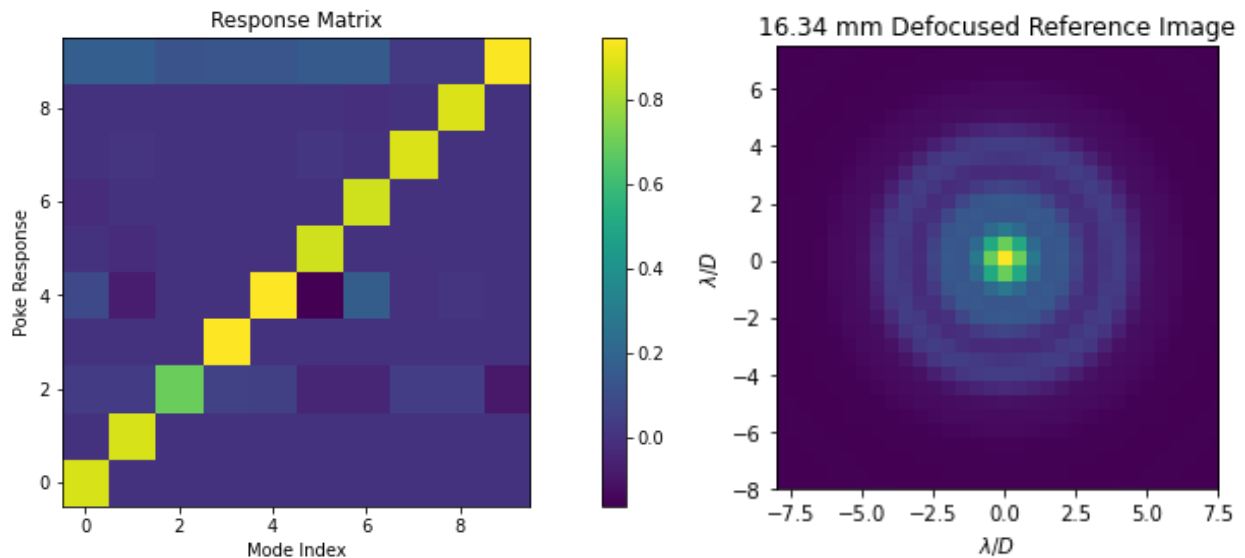


Figure 38. Self-response matrix and ideally defocused PSF in i -band on camsci1/camsci2.

4.3.2.4 The z (909 nm) filter:

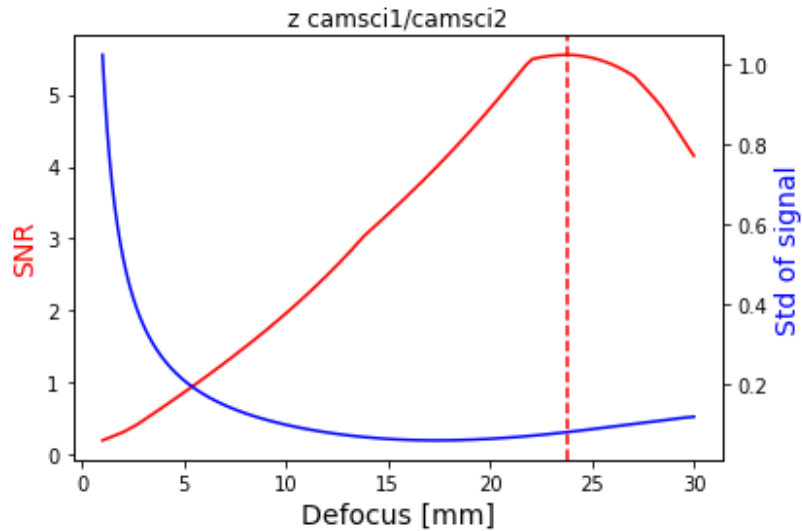


Figure 39. SNR and standard deviation vs camsci1/camsci2 defocus value z -band.

Figure 39 indicates that the optimal defocus location for high SNR is 23.76 mm and produces an SNR of 6.51. The standard deviation of the signal indicates good poke response behavior. The reference image and self-RM in Figure 40 result from this optimal defocus value.

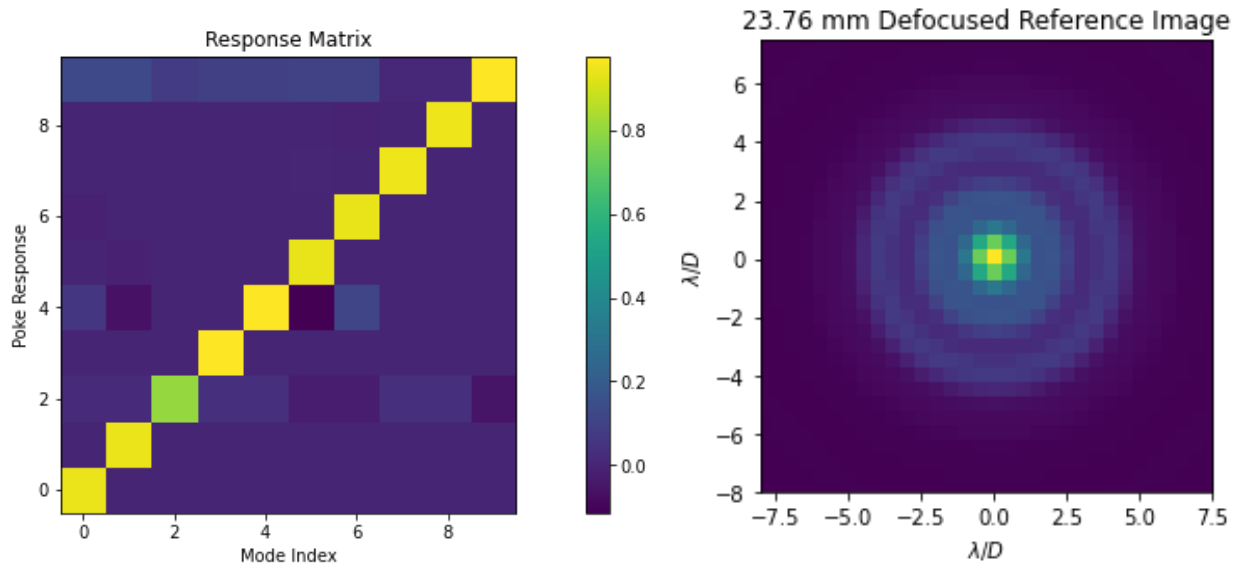


Figure 40. Self-response matrix and ideally defocused PSF for z -band on camsci1/camsci2.

4.4 Conclusions from optimization

The optimization results are summarized in Tables 2 and 3:

Table 2. Summary of camlowfs optimization in simulation.

Filter	Wavelength [nm]	Defocus [mm]	SNR
r	615	24.89	4.27
Ha	656	26.47	4.58
i	762	30.55	5.38
z	909	36.24	6.49

Table 3. Summary of camsci1/camsci2 optimization in simulation.

Filter	Wavelength [nm]	Defocus [mm]	SNR
r	615	16.34	4.28
Ha	656	17.37	4.59
i	762	20.05	5.39
z	909	23.76	6.51

Figure 41 shows the relationship between SNR and wavelength for both camlowfs and camsci1/camsci2.

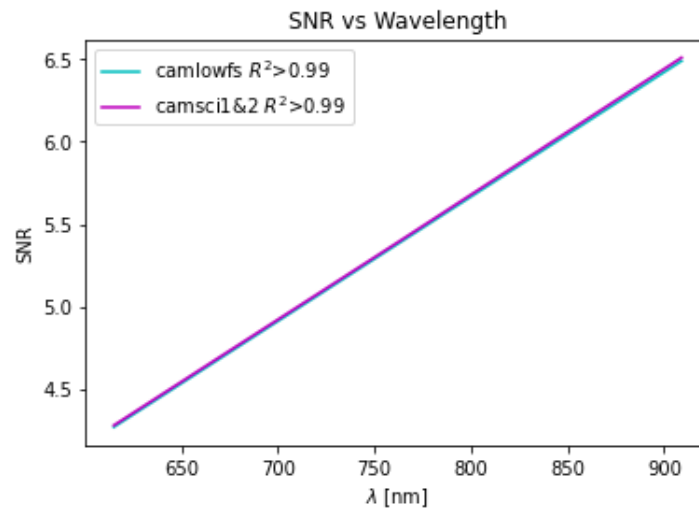


Figure 41. Plot of SNR values from LOWFS&C model optimization as a function of wavelength.

Running a linear regression on the SNR data relationships resulted in R^2 values > 0.99 for both data sets. The slopes from both linear regressions were ~ 0.00755 with the camsci1/camsci2 values producing an SNR value 0.125 greater than the camlowfs values on average. This indicates that the lower F/# system consistently performs better than that of the higher F/# over this wavelength range.

Figure 42 shows the relationship between the optimal defocus position and wavelength for both camlowfs and camsci1/camsci2.

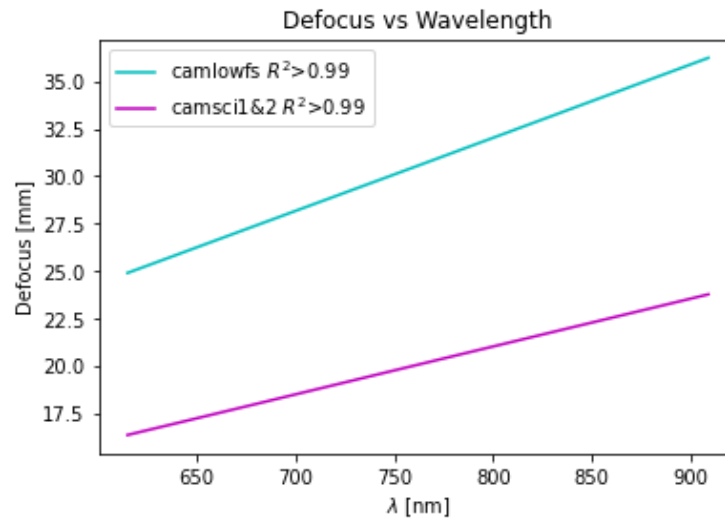


Figure 42. Plot of defocus locations from LOWFS&C model optimization as a function of wavelength.

Linear regressions were run on both defocus data relationships, and it was again found that both resulted in R^2 values > 0.99 . However, the slopes between the data sets varied. The camlowfs relationship produced a slope of ~ 0.0386 and the camsci1/camsci2 relationship produced a slope of ~ 0.0252 . This indicates that the higher F/# system has a quicker rate of change for defocus amount as a function of wavelength as well as produces greater defocus values at every wavelength than the lower F/# system over this range.

It is also worthy to note that when viewing the SNR vs defocus relationship over a larger range than that achievable with focus stages on MagAO-X, a semi-regular oscillatory behavior is observed. An example in the H α filter on camsci1/camsci2 is given in Figure 43.

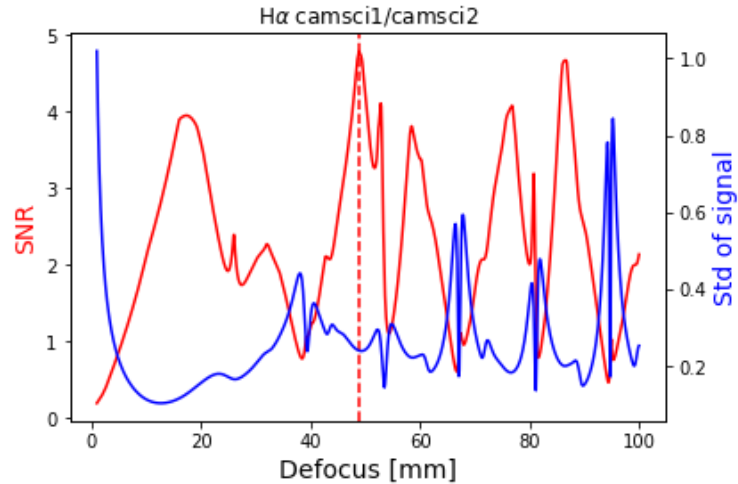


Figure 43. SNR and standard deviation values for an extended defocus range in H α on camsci1/camsci2.

The optimal defocus value for this defocus range is 48.89 mm. Recalling the relationship between longitudinal defocus and pupil plane phase (see section 4.1), when the pupil plane defocus phase is 2π , Δ can be written as:

$$\Delta_{2\pi} = 16\lambda F^2$$

Therefore, for camsci1/camsci2 at H α , the expected defocus corresponding to a 2π phase shift is 49.97 mm. The oscillatory behavior is examined in z-band as shown in Figure 44. With this configuration, $\Delta_{2\pi}$ is expected to be at 69.24 mm.

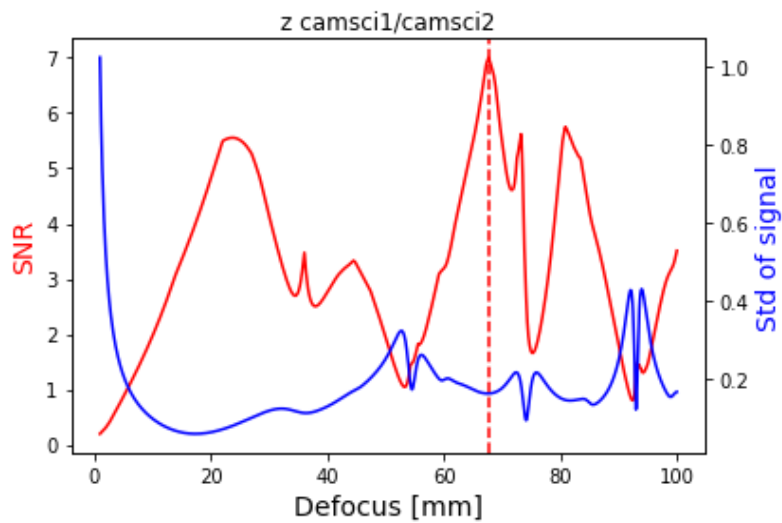


Figure 44. SNR and standard deviation value for an extended defocus range in z-band on camsci1/camsci2.

Figure 44 indicates that the optimal defocus value for this defocus range is 67.70 mm.

Considering all approximations and assumptions inherent to the model along with the SNR metric algorithm, it can be suggested that the true optimal defocus location for LOWFS&C of the first 10 Zernike modes corresponds to a 2π phase shift in the pupil plane. With this, all local optimal defocus positions achievable (or within 10 mm of achievable) on MagAO-X correspond to a $\sim 0.68\pi$ phase shift in the pupil plane. The semi-regular oscillations of SNR with respect to defocus position likely have to do with the nature of phase wrapping.

5 Implementation on MagAO-X

5.1 Interfacing with MagAO-X

A LOWFS&C loop should be calibrated with the lab source in MagAO-X only after proper steps have been taken to increase the quality of the PSF. The calibration itself is largely managed with the Compute and Control for Adaptive Optics (CACAO) real-time software package installed on the instrument [22], though the user must ensure the system is set up properly and run the CACAO commands in the correct order.

MagAO-X must be properly aligned, and the primary / high order loop should be closed. This will get the lab-source PSF to the quality needed for the MagAO-X “eye doctor” [23] software to dial in residual (typically low order) wavefront errors. Once the PSF on the science cameras is corrected as much as possible with the wavefront sensing filter of interest, the WFS camera should then be moved to the proper defocus location as indicated in Tables 2 and 3. A 32 x 32 ROI should be selected, and the camera speed should be adjusted such that it is running as fast as possible while reading an adequate number of counts (somewhere between 25% to 65% of the maximum count allowance for that camera). Adjusting the available ND filters, along with

the ADC and vertical shift speeds of the camera is useful to do this. It is critical to ensure MagAO-X is set up to look at the correct camera for LOWFS&C as there are multiple cameras that have the capability to perform LOWFS&C.

Once the ideal PSF is defocused and all adjustments have been made to ensure proper signal at the correct filter, the CACAO software is used to perform the loop calibration. The following steps are followed to do this:

1. Take a dark with the WFS camera such that it can be recognized by the CACAO processes.
2. Perform a latency test to ensure the WFS camera is adequately synced with the shapes on the NCPC DM.
 - a. The CACAO name for this process is *mlat*.
3. Initiate image acquisition such that CACAO is receiving the WFS images.
 - a. The CACAO name for this process is *acquWFS*.
4. Take a Hadamard response.
 - a. The CACAO name for this process is *acqlin_zRM*. This response matrix provides the bright field mask and determines the number of modes the WFS setup can correct for. An example bright field mask resulting from this process is shown in Figure 45 and is comparable to that shown in Figure 20. The larger BF region in the CACAO calibrated loop allows for higher order control, up to 38 in this example H α -narrow calibration on camsci2.

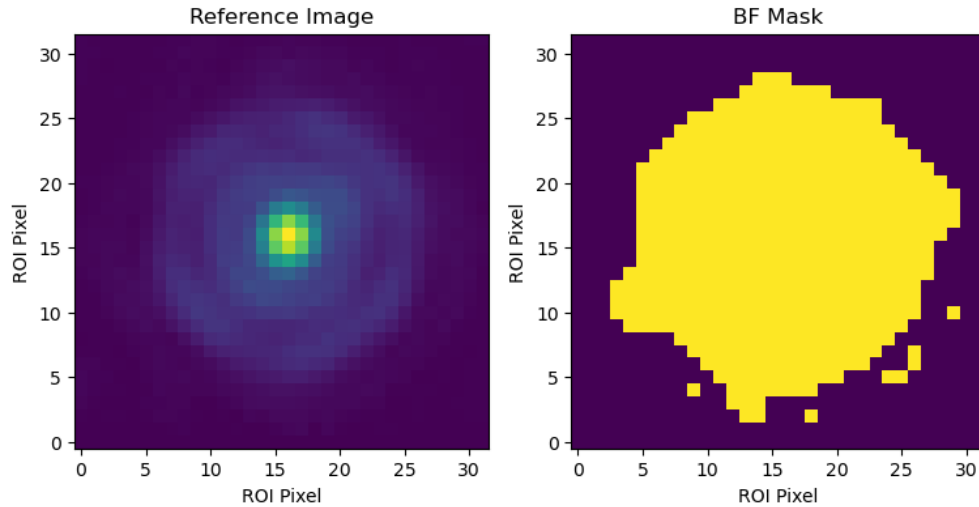


Figure 45. Example reference image and BF mask created by CACAO for an $H\alpha$ -narrow calibration on *camsci2*.

5. Perform a low order Fourier response.
 - a. The CACAO name for this process is *acqlin_loRM*. This is where the low order Zernike modes are applied to the NCPC DM and the WFS response images are reference subtracted and recorded. An example of the DM modes and WFS response images are shown in Figure 46 and Figure 47 and are comparable to Figures 18 and 21 respectively. Note that the index of the modeled tip (0) and tilt (1) modes have been switched with respect to the modeled modes. Also note that the WFS response images are flipped with respect to those modeled due to parity changes that occur within MagAO-X. These differences are irrelevant as the functionality of the basis remains the same as what was done in the model.

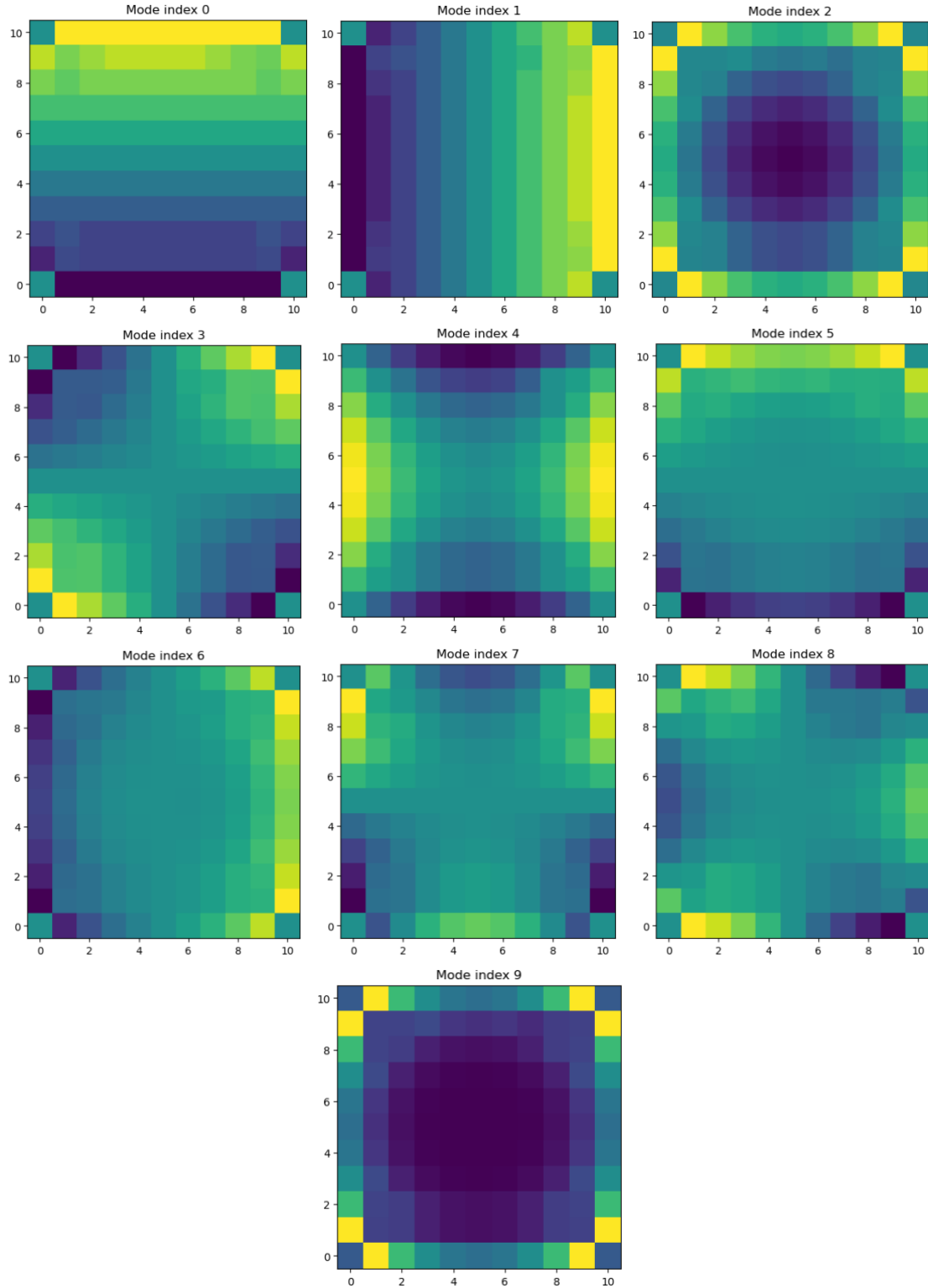


Figure 46. Example Zernike modal basis on DM NCPC used to train a LOWFS&C loop in $H\alpha$ on camsci2.

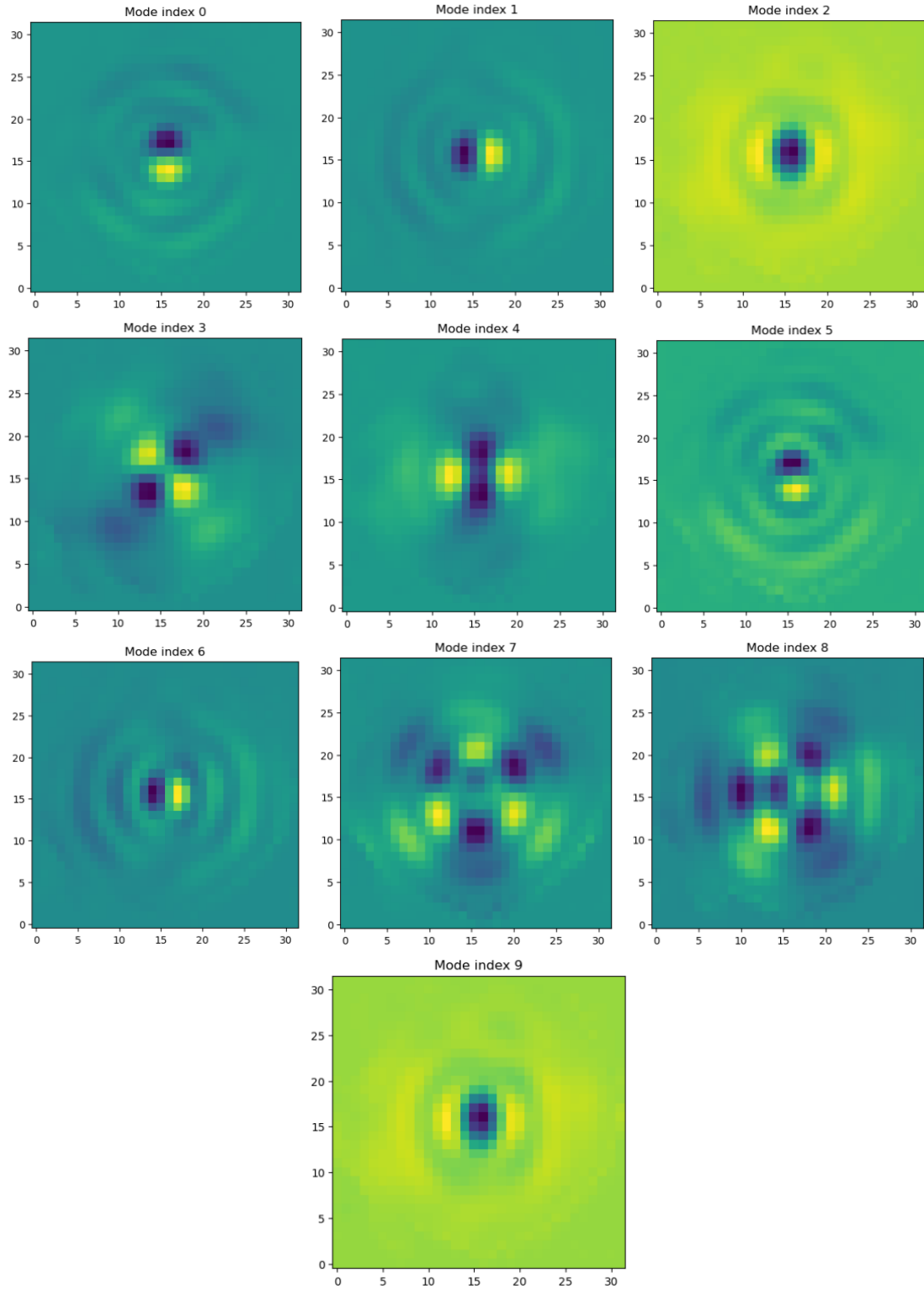


Figure 47. Example of Zernike mode WFS response images used to train LOWFS&C loop in $H\alpha$ on camsci2.

6. Compute the Fourier response matrix.
 - a. The CACAO name for this process is *compFCM*. This follows the same linear principles as outlined in Section 4.4 and what was implemented in the LOWFS&C model.
7. Archive the calibration such that it can be applied when performing LOWFS&C in lab or on-sky.
 - a. The resulting calibration sorts the correctable modes into mode blocks. When using a calibration, these blocks can have individual gains applied to them as to select what modes are used in the LOWFS&C loop and the magnitude of their correction (0-100%).

Once a calibration has been taken, it can be tested on the lab source. The correct calibration must be applied for the appropriate filter and camera as they were when the loop was trained. Parameters used to set the speed of the camera such as the exposure time, ND filters, ADC, and vertical shift speeds for the calibration *do not* need to be matched; the calibrated loop should be able to perform if adequate signal is incident on the WFS camera.

When performing a calibration for a reflected PSF off the Lyot mask, the coronagraph should be aligned first and the reflected PSF should be used for the calibration. This is because slight differences in alignment between when MagAO-X is performing nominal and high-contrast imaging will cause the ideal PSF to be different among these two scenarios. Figure 48 shows a reference image for a defocused reflected-light camlowfs calibration with the z filter.

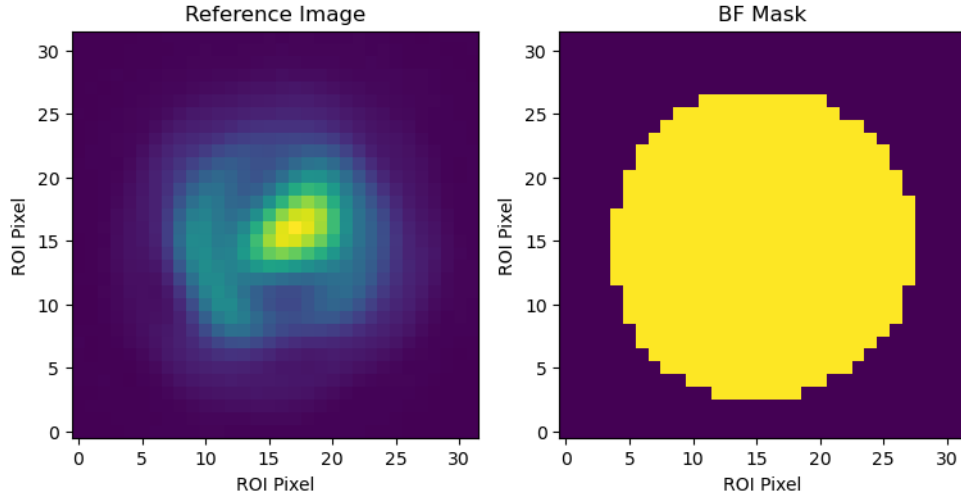


Figure 48. Example BF mask and reference image for reflected light calibration on camlowfs in z-band.

5.2 Metrics for LOWFS&C and CLOWFS&C performance on MagAO-X

Several metrics are used to evaluate the performance of a LOWFS&C calibration on MagAO-X. Dark subtracted WFS images X_i of size N are evaluated by calculating the mean squared error (MSE) of the images in open and closed loop to the reference image μ used for the calibration.

$$MSE = \frac{\sum (X_i - \mu)^2}{N}$$

Note that X_i and μ are normalized such that the sum of each image is 1. It is expected that when the loop is closed, the MSE will be reduced as the loop is converging WFS images towards the reference.

WFS images are also evaluated through finding the modal reconstructions at each frame. When the loop is closed, the modal reconstructions are expected to converge to a steady state. The algorithm used for evaluating this for a dark subtracted WFS image X_i with normalized reference image μ_{norm} (sum of image =1) is as follows:

1. Multiply X_i by the BF mask corresponding to the calibration used for the loop to get X_{iBF} .

2. Normalize $X_{i\ BF}$ such that the sum of all pixels is equal to 1.
3. Apply the BF mask to μ_{norm} and subtract this from $X_{i\ BF}$.
4. Calculate the modal response v (as given in Section 3.3).

LOWFS&C is also evaluated with dark subtracted science plane images by monitoring relative Strehl. When there is no coronagraph in place, the intensity contained in the central PSF is monitored during open and closed loop operation. When there is a coronagraph in place, the 2k DM is used to create copies of the PSF at a user defined angular separation from the central PSF (sparkles), and the intensity contained in the cores of these PSF copies is monitored. Furthermore, the relative achieved contrast of the coronagraphic image is evaluated by summing pixels at low λ/D radial increments relevant to the LOWFS&C corrections. The running mean and standard deviation of these radial pixel sums are observed to evaluate the loop's influence on stability in the high-contrast region of the coronagraphic images. A decrease in mean value and standard deviation in radial sums indicate that more starlight light is contained in the PSF core (blocked by the FPM) and temporal variations are being minimized. This corresponds to positive CLOWFS&C performance, as stability in the dark-field region and increase in blocked starlight is ideal for coronagraphic imaging.

5.3 In-lab Test Results

The following in-lab tests correspond to two non-coronagraphic LOWFS&C calibrations (sci2-H α , lowfs-z) and one CLOWFS&C calibration (lowfs-z-c). The details for those calibrations are given in table 4 with camera configurations for each test summarized in Appendix B.

Table 4. Details for lab-tested calibrations including the camera used, filter used, and number of modes corresponding to each mode block.

Name	Camera	Filter	Total # of Modes	Number of Modes in Block					
				Block 0	Block 1	Block 2	Block 3	Block 4	Block 5
sci2-H α	camsci2	H α -narrow	38	2	1	6	9	10	10
lowfs-z	camlowfs	z	37	2	1	6	8	10	10
lowfs-z-c	camlowfs	z	34	2	1	5	6	11	9

Vertical lines are used in time-dependent plots to indicate loop commands including ‘loop closed’, ‘loop paused’, and ‘loop zero’ based on log data saved on MagAO-X. Closing the loop indicates correction signals are being actively sent to the DM. Pausing the loop means no correction signals are being sent to the DM but any former correction-shapes on the DM at that point will remain. Zeroing the loop clears any shape on the DM at that point but does not stop corrective commands from being sent.

5.3.1 Testing the sci2-H α calibration

The following lab tests correspond to the sci2-H α calibration. This calibration was taken after rigorous PSF optimization on the science cameras with the MagAO-X eye doctor software. Both the calibration and following tests were performed in a cleanroom environment with the lab source prior to MagAO-X being placed on the Magellan Clay Nasymth platform. The calibration reference image and bright field mask are shown in Figure 49.

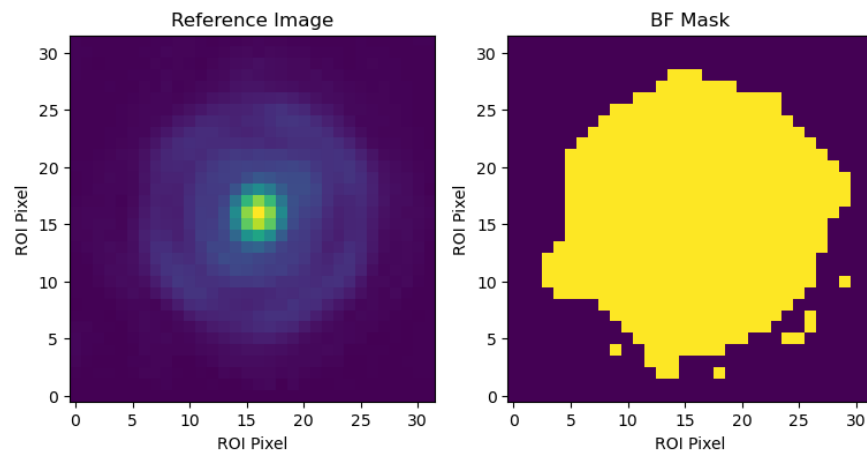


Figure 49. sci2-H α calibration reference image and bright field mask.

5.3.1.1 Sci2-H α test 1:

For test 1, tip/tilt, defocus, vertical astigmatism, vertical coma, horizontal coma, vertical trefoil, and spherical aberrations were introduced to the system. Figure 50 shows open and closed loop images from this test. The images are normalized such that the sum of each image is 1.

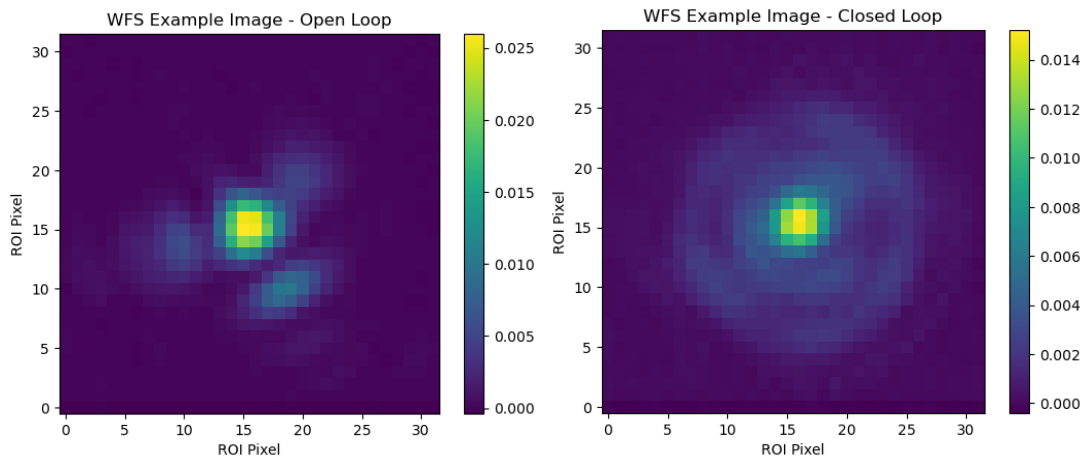


Figure 50. Example open and closed loop WFS images for sci2-H α test 1.

The loop parameters over the data acquisition time are given in Figure 51.

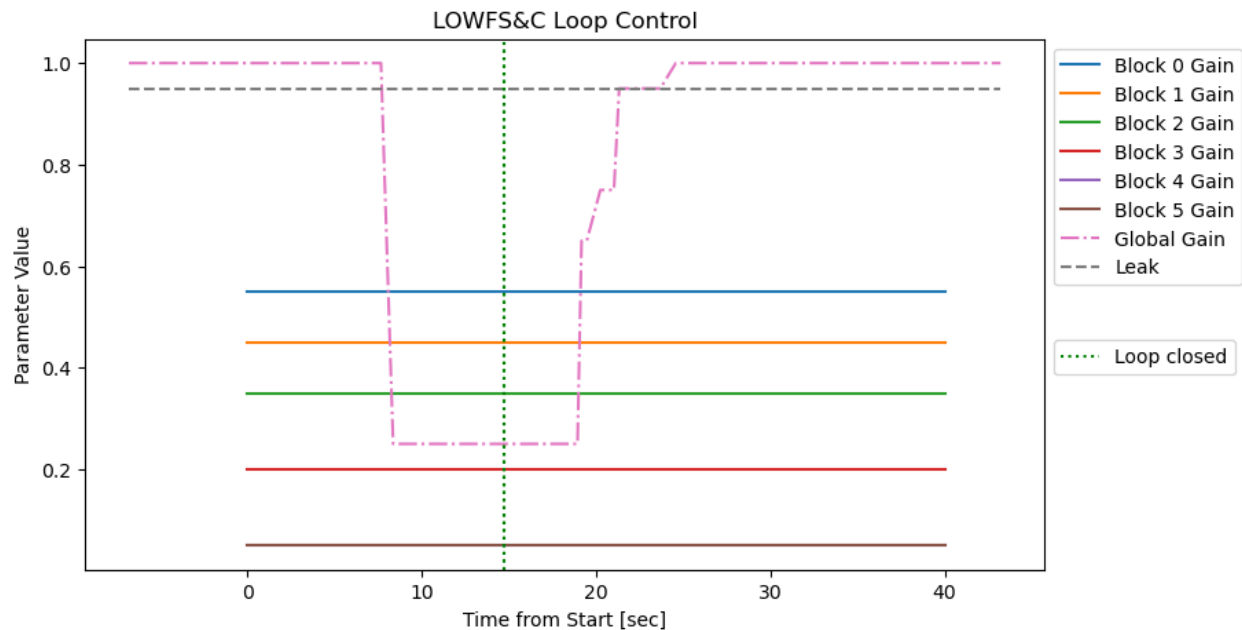


Figure 51. Global gain, block gains, and leak applied to the LOWFS&C loop for sci2-H α test 1.

The loop was zeroed and paused prior to data acquisition. Gains for blocks 3 and 4 overlap here.

It was quickly found that when implementing a LOWFS&C loop, it is best to start with low gains (individual or global) and step the gain values up once the loop has been closed. If gains are initially set high and the LOWFS&C loop is closed in this state, it is very common for the loop to instantly run away (significantly degrade the PSF quality).

The MSE metric was used on the WFS images to evaluate convergence to the reference image as shown in Figure 52.

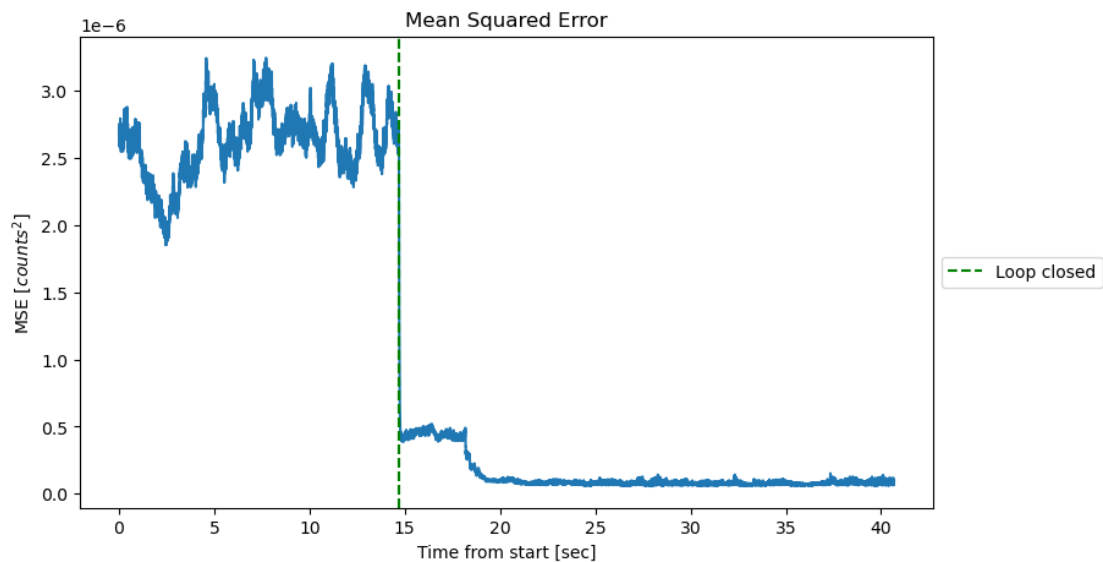


Figure 52. *MSE over data acquisition time for sci2-H α test 1.*

Figure 52 indicates a ~96% decrease in MSE based on average values from before the loop was closed and after the loop had settled (about 20 seconds after data acquisition started).

The mode reconstruction metric was used on the WFS images to evaluate modal response before and after the loop was closed as shown in Figure 53.

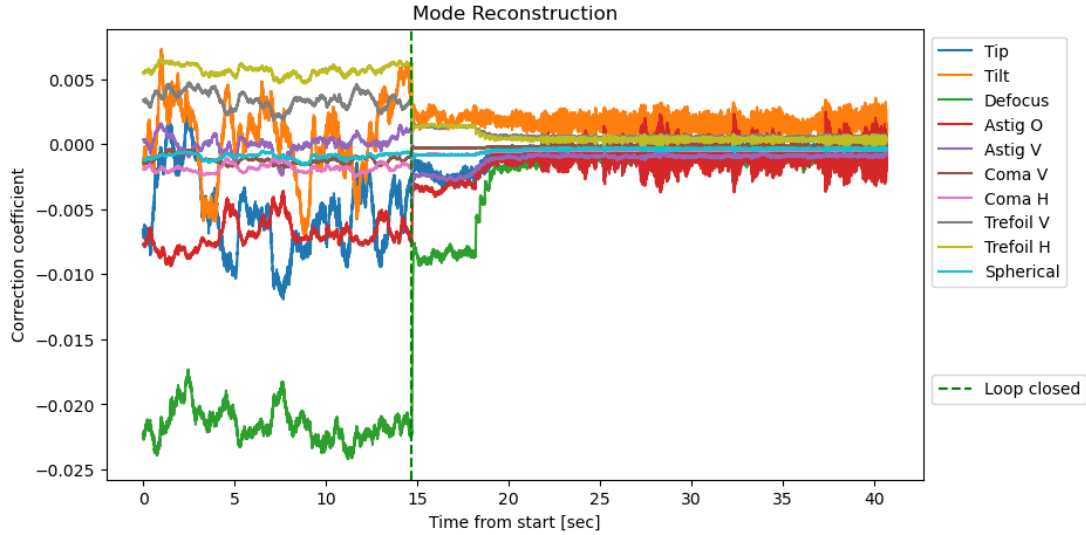


Figure 53. Mode reconstruction over data acquisition time for sci2-H α test 1.

Figure 53 indicates that the correction coefficients for the first 10 Zernike modes converge once the loop is closed, indicating the closed loop is stable.

5.3.1.2 Sci2-H α test 2:

For test 2, tip/tilt, defocus, vertical astigmatism, oblique astigmatism, vertical coma, horizontal coma, vertical trefoil, horizontal trefoil, and spherical aberrations were introduced to the system. Figure 54 shows open and closed loop images from this test. The images are normalized such that the sum of each image is 1.

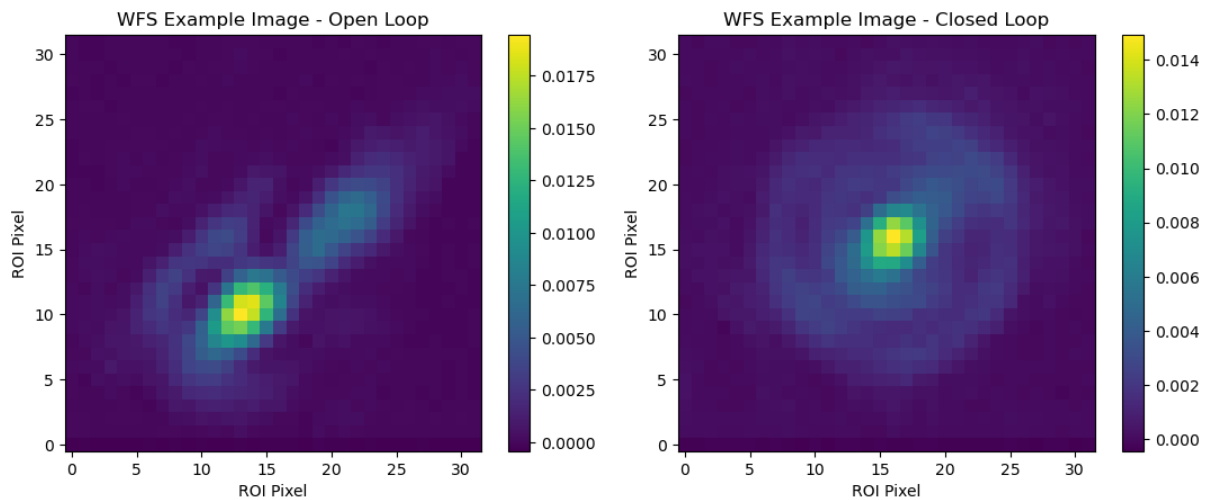


Figure 54. Example open and closed loop WFS images for sci2-H α test 2.

The loop parameters over the data acquisition time are given in Figure 55.

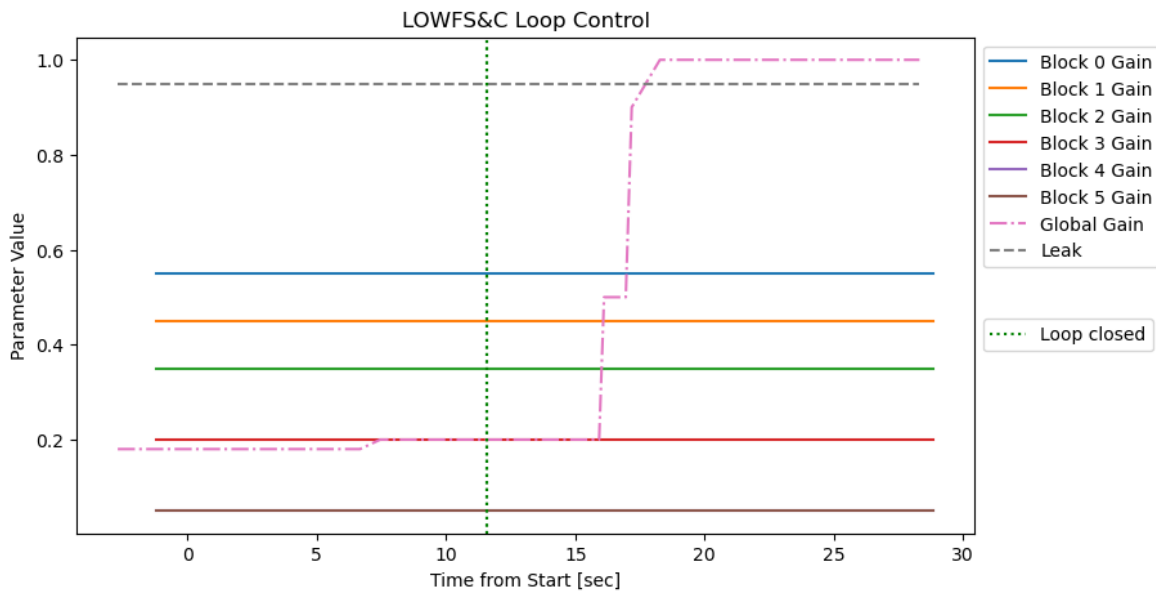


Figure 55. Global gain, block gains, and leak applied to the LOWFS&C loop for sci2-H α test 2.

The loop was zeroed and paused prior to data acquisition. Gains for blocks 3 and 4 overlap here.

As in test 1, the global gain was set low initially and walked up.

The MSE metric was again used to evaluate WFS image convergence towards the reference as shown in Figure 56.

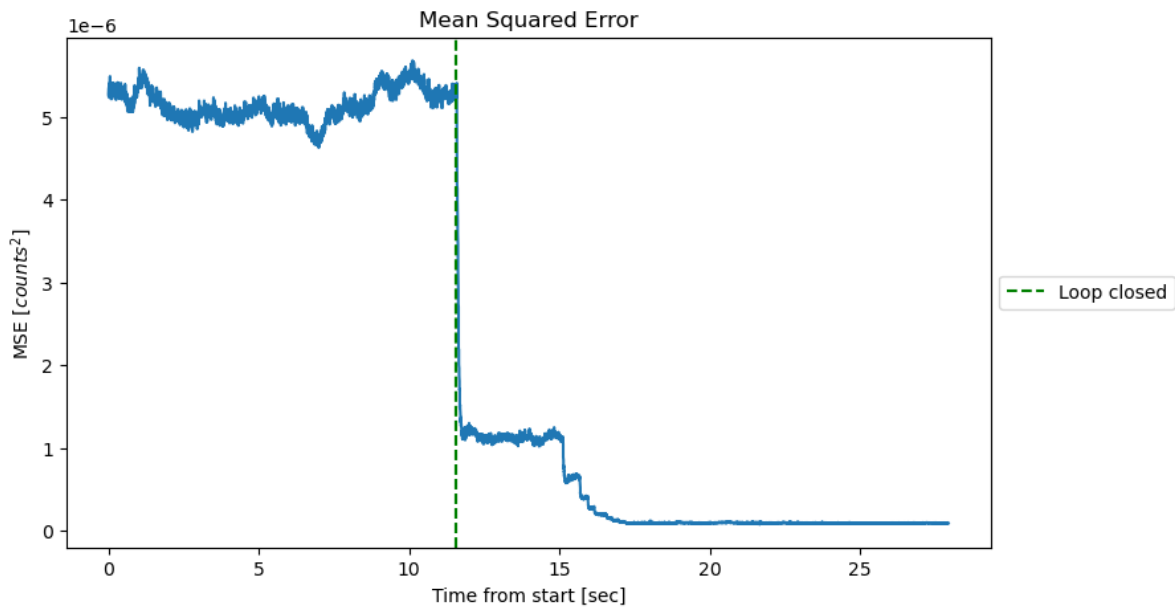


Figure 56. MSE over data acquisition time for sci2-H α test 2.

Figure 56 indicates a ~99% decrease in MSE based on average values from before the loop was closed and after the loop had settled (about 18 seconds after data acquisition started).

The mode reconstruction metric was used on the WFS images to evaluate modal response before and after the loop was closed as shown in Figure 57.

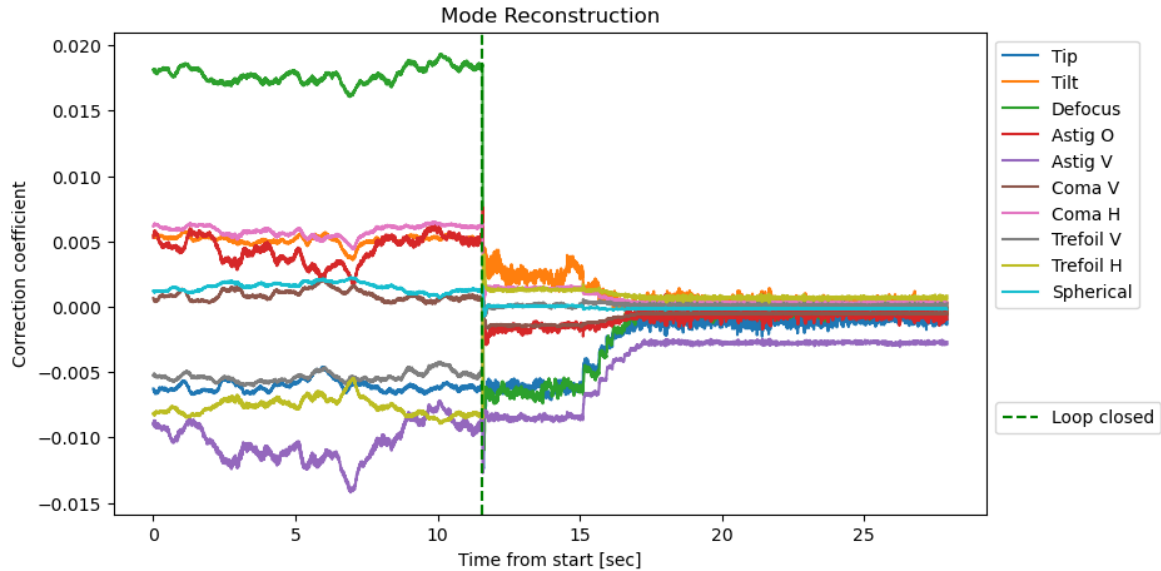


Figure 57. Mode reconstruction over data acquisition time for sci2-H α test 2.

Figure 57 indicates that the correction coefficients for the first 10 Zernike modes converge once the loop is closed, indicating the closed loop is stable. The effect of raising the global gain is easily seen in figures 56 and 57 as there are clear steps after the loop was closed that correspond to increases in global gain seen in Figure 55.

5.3.1.3 Conclusions

Both tests indicate that this calibration is likely capable of LOWFS&C on-sky under seeing conditions that allow for wavefront errors at the WFS to remain in the linear regime. The rather extreme errors applied during test 2 result in a defocused PSF considerably worse than what is typically expected after primary AO correction under good seeing conditions, further suggesting this calibration will perform successfully on sky.

5.3.2 Testing the lowfs-z calibration

The following lab tests correspond to the lowfs-z calibration. This calibration was taken after rigorous PSF optimization on the science cameras with the MagAO-X eye doctor software. Both the calibration and following tests were performed in a cleanroom environment with the lab source prior to MagAO-X being placed on the Magellan Clay Nasymth platform. The calibration reference image and bright field mask are shown in Figure 58.

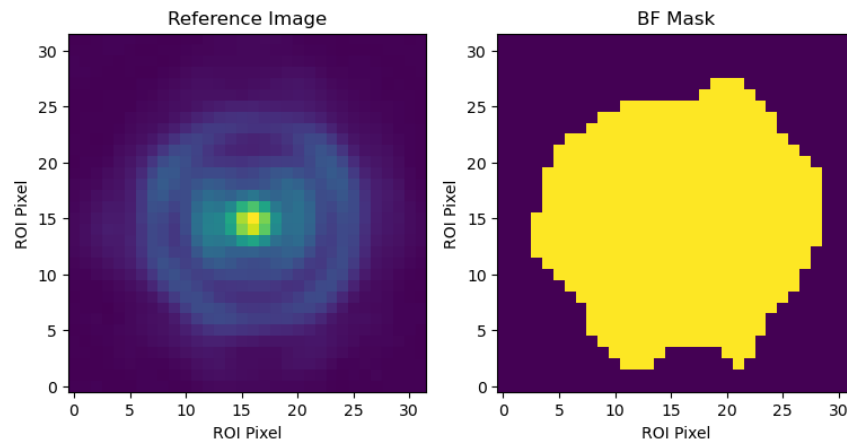


Figure 58. lowfs-z calibration reference image and bright field mask.

5.3.2.1 Lowfs-z test 1:

For test 1, tip, defocus, vertical astigmatism, oblique astigmatism, horizontal coma, horizontal trefoil, and spherical aberrations were introduced to the system. Figure 59 shows open and closed loop images from this test. The images are normalized such that the sum of each image is 1.

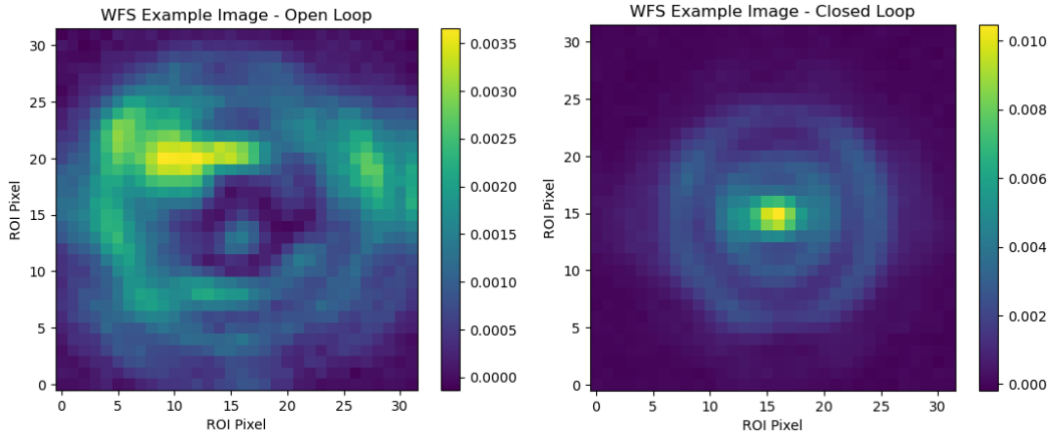


Figure 59. Example open and closed loop WFS images for lowfs-z test 1.

The loop parameters over the data acquisition time are given in Figure 60.

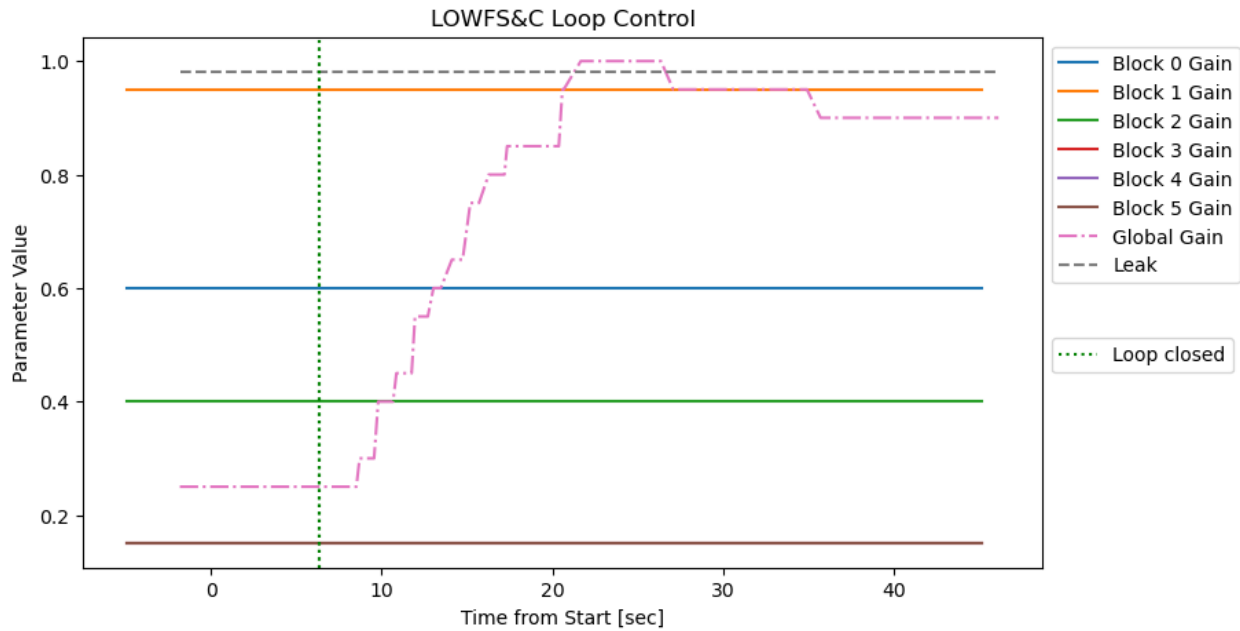


Figure 60. Global gain, block gains, and leak applied to the LOWFS&C loop for lowfs-z test 1.

The loop was zeroed and paused prior to data acquisition. Gains for blocks 3 and 4 overlap here.

The MSE metric was used on the WFS images to evaluate their convergence towards the reference image as shown in Figure 61.

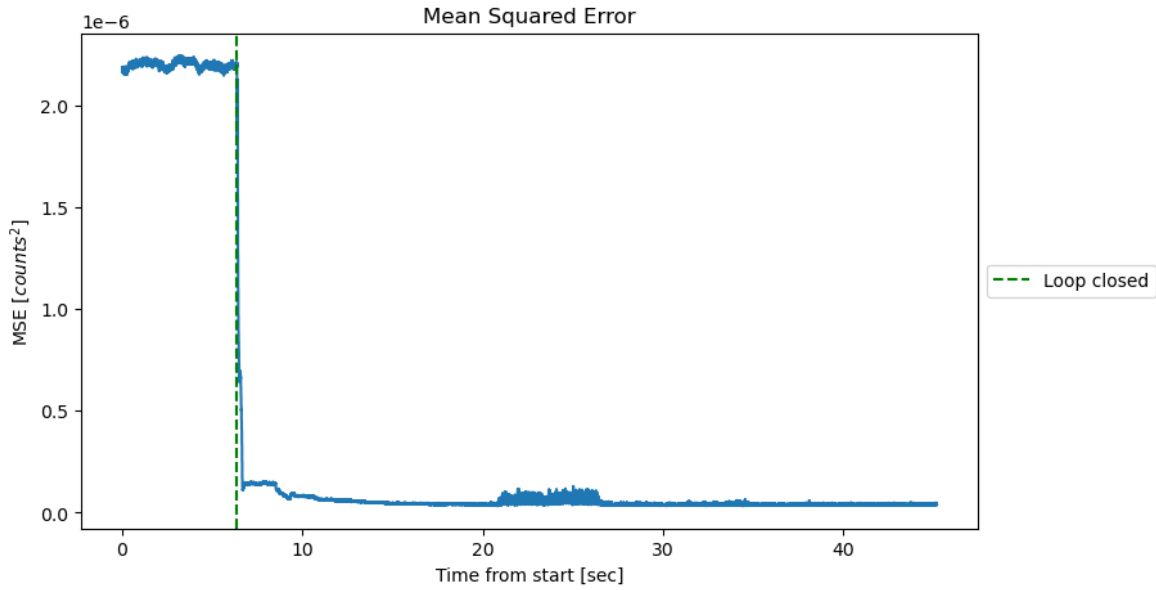


Figure 61. MSE over data acquisition time for lowfs-z test 1.

Figure 61 indicates a $\sim 97\%$ decrease in MSE based on average values from before the loop was closed and after the loop had settled (about 35 seconds after data acquisition started).

The mode reconstruction metric was used on the WFS images to evaluate modal response before and after the loop was closed as shown in Figure 62.

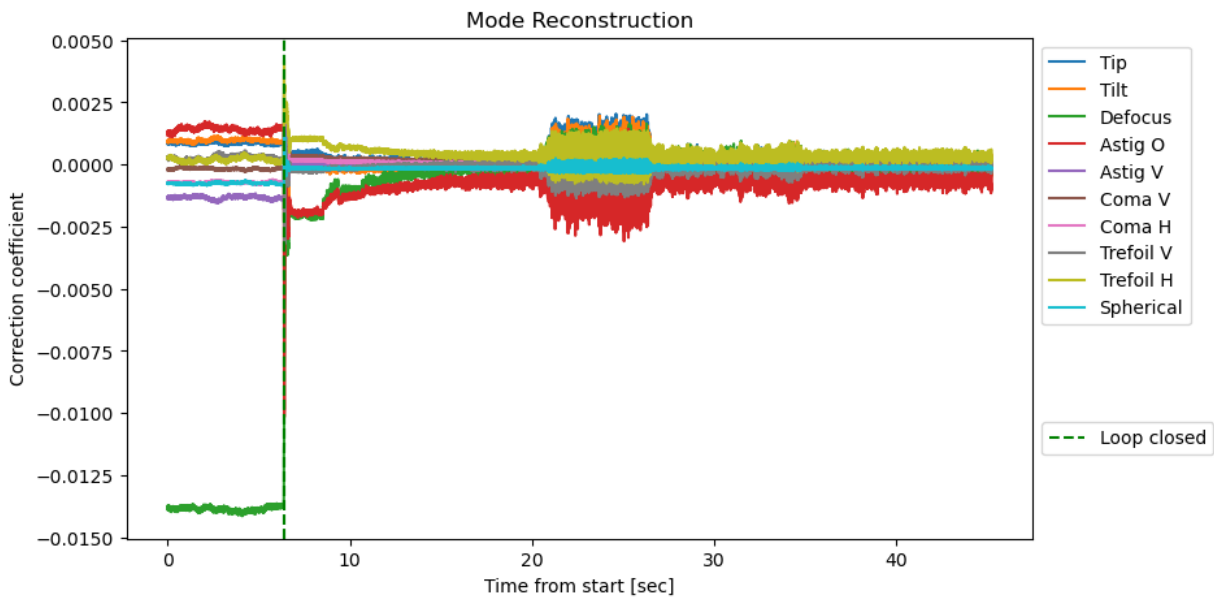


Figure 62. Mode reconstruction over data acquisition time for lowfs-z test 1.

Figure 62 indicates that the correction coefficients for the first 10 Zernike modes converge once the loop is closed, indicating the closed loop is stable. However, comparing Figure 62 and Figure 60 illustrates an important relationship between the modal response convergence and gain value. It is seen that when the global gain is brought to 1 (around 20 seconds from start), the modal response begins to diverge indicating this gain is too high for optimal loop performance. When the global gain parameter is stepped back down (around 25 and 35 seconds from start), the modal responses converge again but do not perform as well as before the global gain was brought to 1. This relationship has two important implications:

- 1) If the gain values are too large, loop performance can degrade.
- 2) Even if the gain is brought back down, the performance may still not be ideal.

Because of this, it proved beneficial to zero the global gain and ‘loop zero’ if a loop began to diverge. This was especially useful on-sky when the LOWFS&C loop was being optimized before a science observation.

5.3.2.2 Lowfs-z test 2:

For test 2, tilt, defocus, oblique astigmatism, vertical coma, horizontal trefoil, vertical trefoil, and spherical aberrations were introduced to the system. Figure 63 shows open and closed loop images for this test. The images are normalized such that the sum of each image is 1.

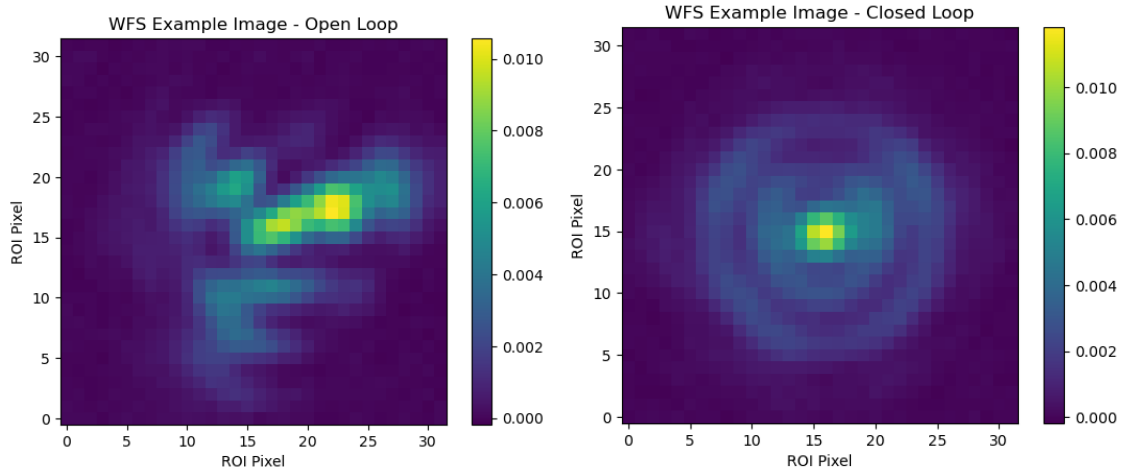


Figure 63. Example open and closed loop WFS images for lowfs-z test 2.

The loop parameters over the data acquisition time are given in Figure 64.

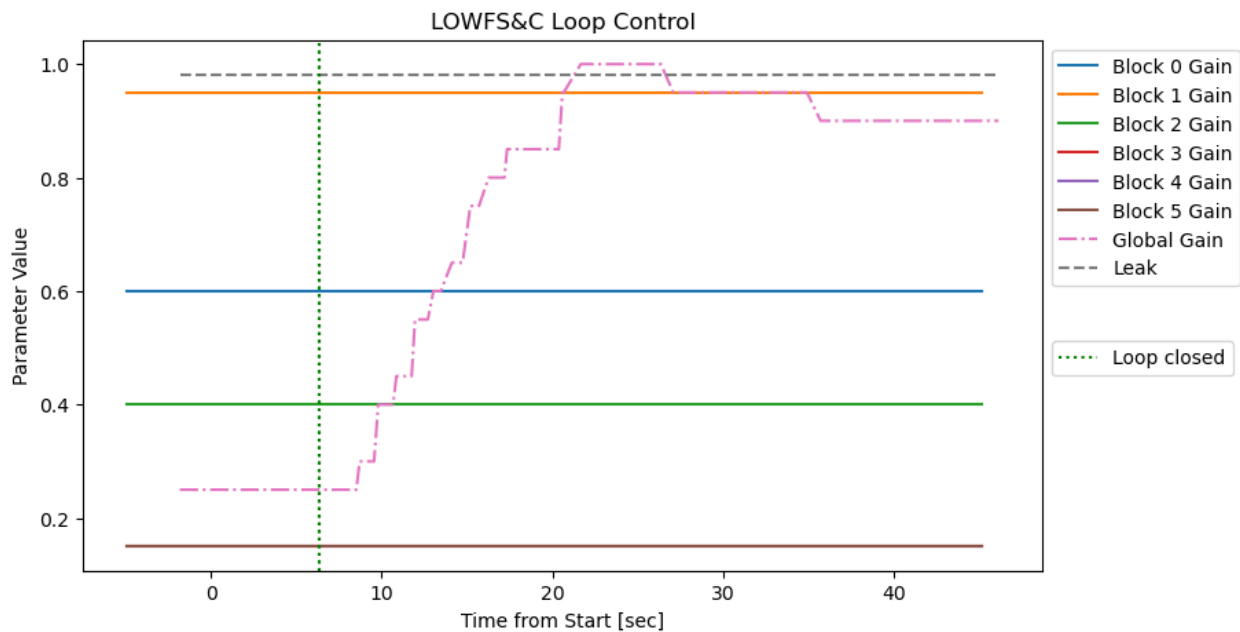


Figure 64. Global gain, block gains, and leak applied to the LOWFS&C loop for lowfs-z test 2.

The loop was zeroed and paused prior to data acquisition. Gains for blocks 3 and 4 overlap here.

The MSE metric was used on the WFS images to evaluate their convergence towards the reference image as shown in Figure 65.

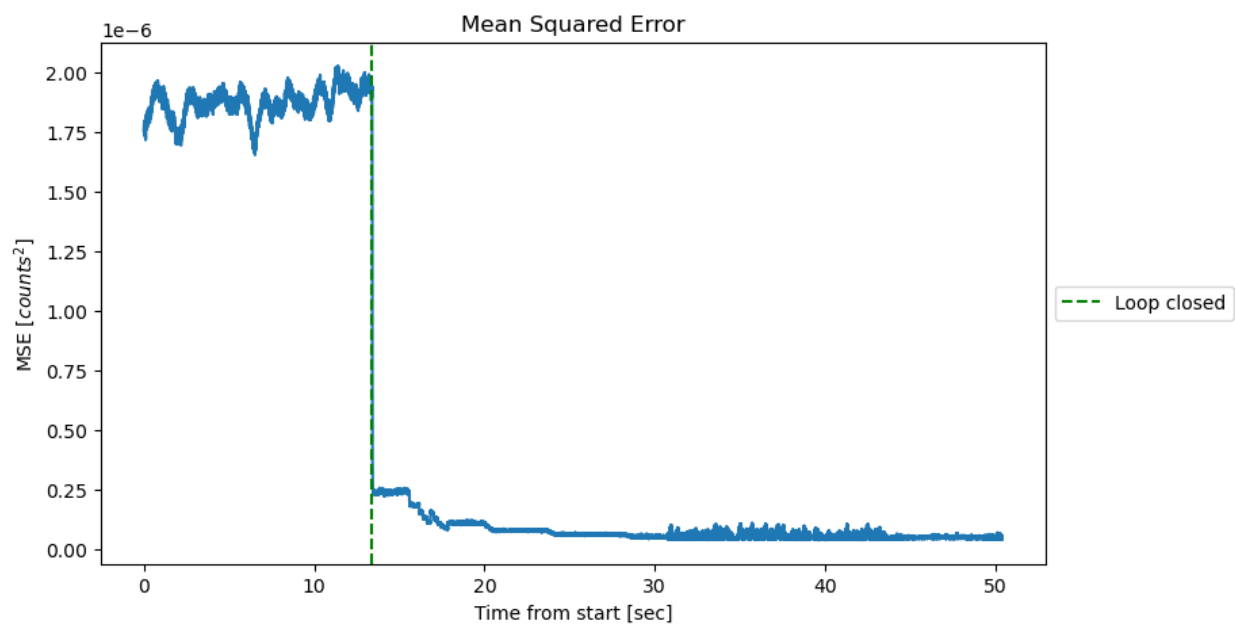


Figure 65. MSE over data acquisition time for lowfs-z test 1.

Figure 65 indicates a ~97% decrease in MSE based on average values from before the loop was closed and after the loop had settled (about 25 seconds after data acquisition started).

The mode reconstruction metric was used on the WFS images to evaluate modal response before and after the loop was closed as shown in Figure 66.

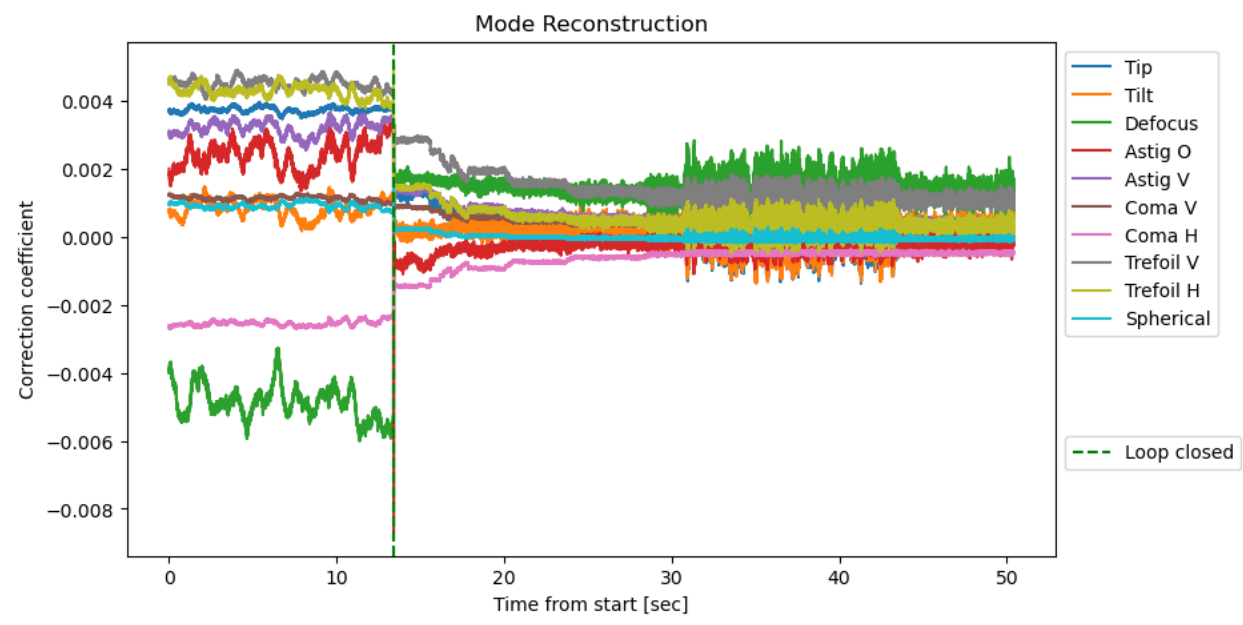


Figure 66. Mode reconstruction over data acquisition time for lowfs-z test 2.

The modal response again converges after the loop is closed, and similar behavior with the gain / correction coefficient as in lowfs-z test 1 is observed.

5.3.2.3 Conclusions

The induced wavefront errors of both lowfs-z tests are again significantly worse than what is expected after the primary AO correction. Considering the results from both tests, it is expected that the lowfs-z calibration will perform successfully on-sky if linear conditions are met.

5.3.3 Testing the lowfs-z-c calibration

The following lab tests correspond to the lowfs-z-c calibration, a CLOWFS&C calibration in which reflected light off of the Lyot focal plane mask is used for the reference PSF. This calibration was taken after semi-rigorous PSF optimization on the science cameras with the MagAO-X eye doctor software. Both the calibration and following tests were performed after MagAO-X was moved to the Magellan Clay Nasymth platform. The calibration reference image and bright field mask are shown in Figure 67.

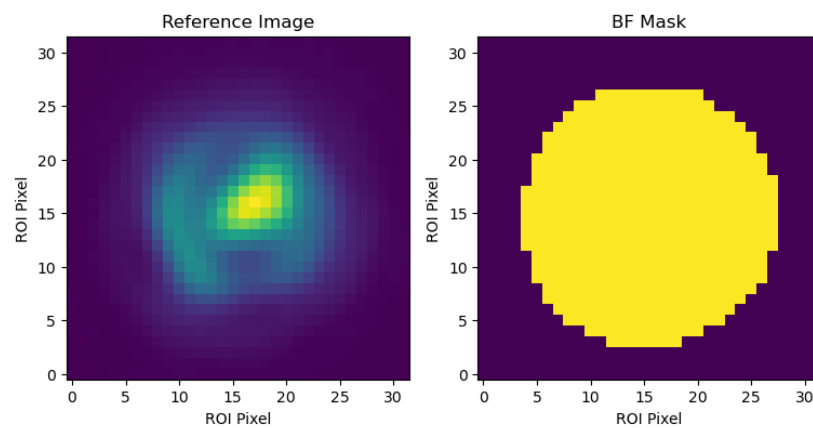


Figure 67. *lowfs-z-c reference image and bright field mask.*

5.3.3.1 Lowfs-z-c test 1:

For test 1, the lowfs-z-c calibration is tested without injecting any wavefront errors into the system but was performed after alignment had been lost from when the calibration was taken. No Lyot stop is in place for this test. The loop control parameters for the data set are given in Figure 68.

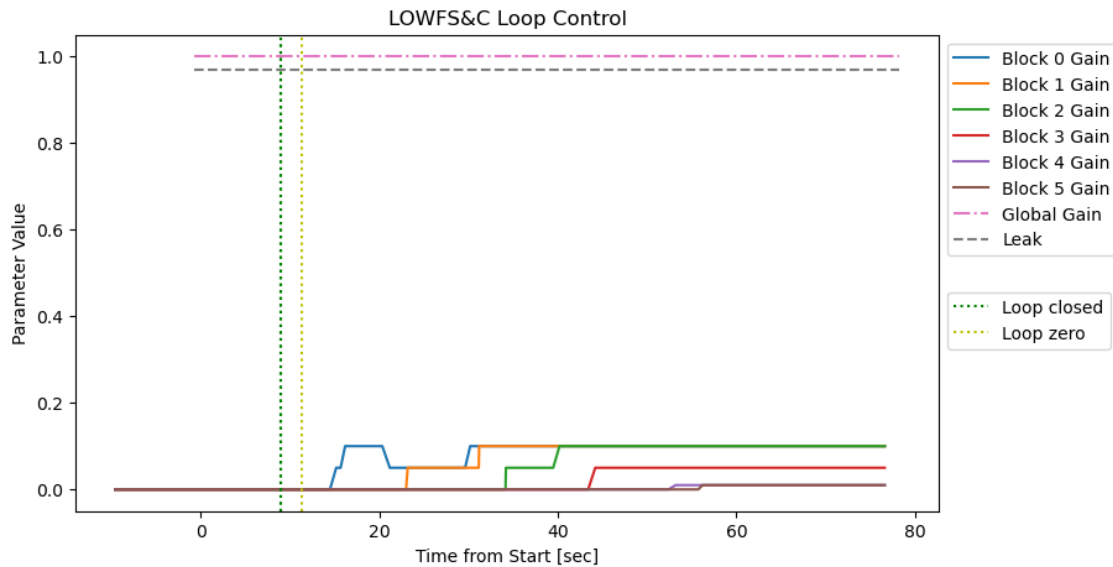


Figure 68. Global gain, block gains, and leak applied to the LOWFS&C loop for lowfs-z-c test 1.

It is seen that by the end of the data acquisition period all gains are raised, meaning the CLOWFS&C loop is closed on 34 modes during this test. The median coronagraphic image for the data set is shown in Figure 69.

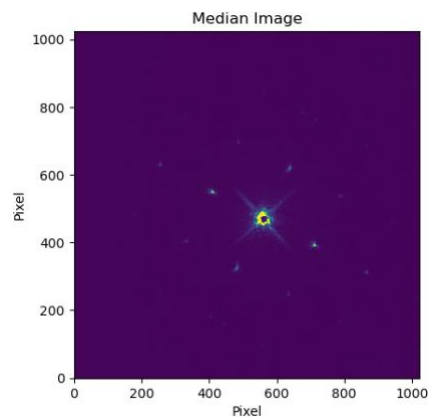


Figure 69. Median coronagraphic image for the lowfs-z-c test 1.

The PSF copies (sparkle) cores used to monitor relative change in Strehl are shown in Figure 70.

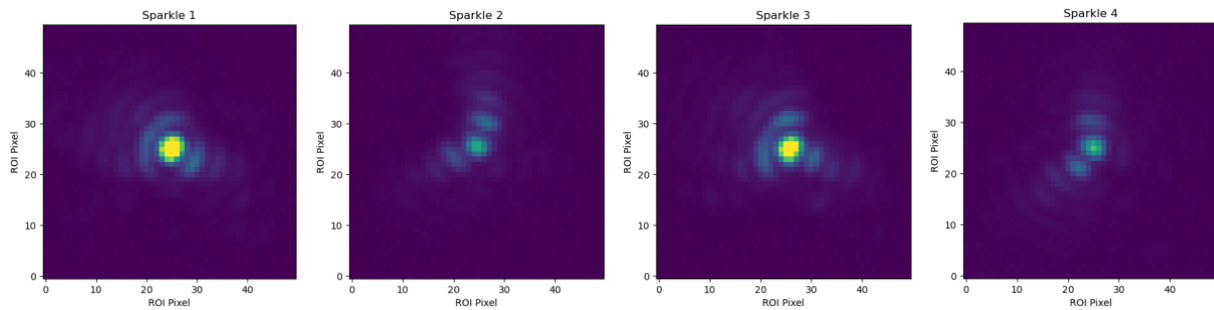


Figure 70. Sparkle PSFs used to monitor relative change in Strehl for lowfs-z-c test 1.

Figure 71 shows the sparkle core sums over the data acquisition period. The values are very similar for all sparkles, making the different plot lines for the 4 sparkle cores indistinguishable.

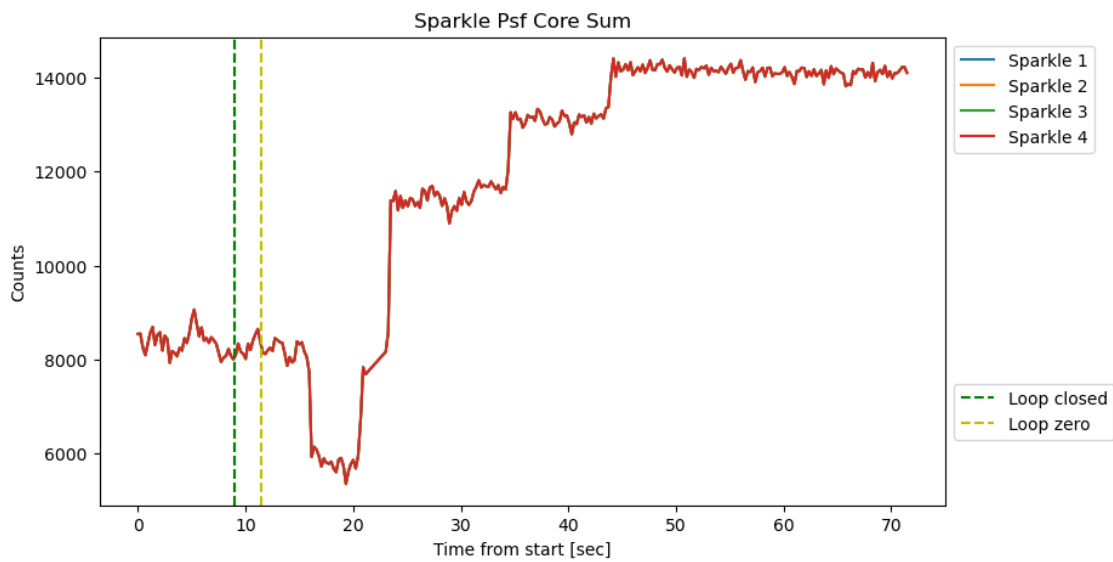


Figure 71. Sparkle core sums over the data acquisition period of lowfs-z-c test 1.

Figure 71 indicates a ~75% increase in relative Strehl from closing the CLOWFS&C loop.

Raising the tip/tilt block too high initially causes a dip around 15 seconds but after it is brought back down and stepped up slowly with the remaining blocks the loop performs well.

Pixel sums are taken at several radial distances on the coronagraphic image as indicated in Figure 72.

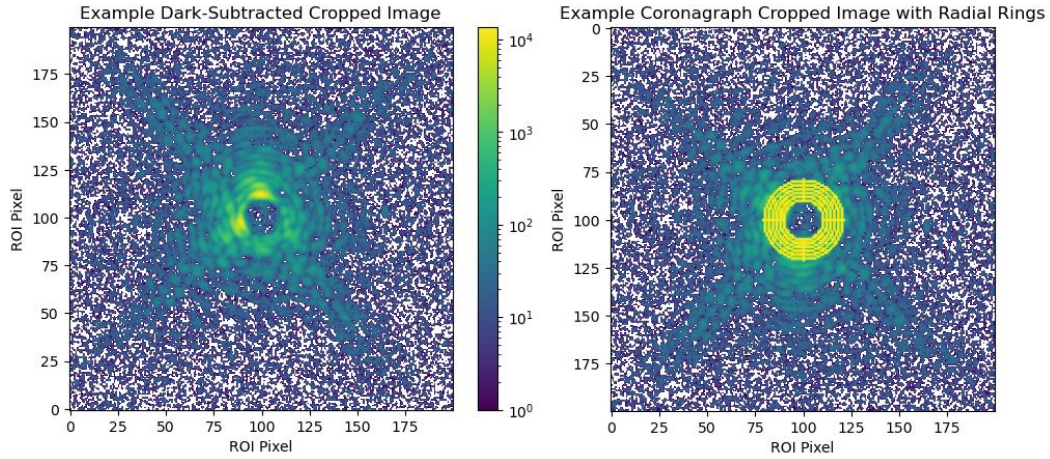


Figure 72. Example reference subtracted cropped image and image with indication of radial pixel sum locations for lowfs-z-c test 1.

The resulting radial sums are given in Figure 73.

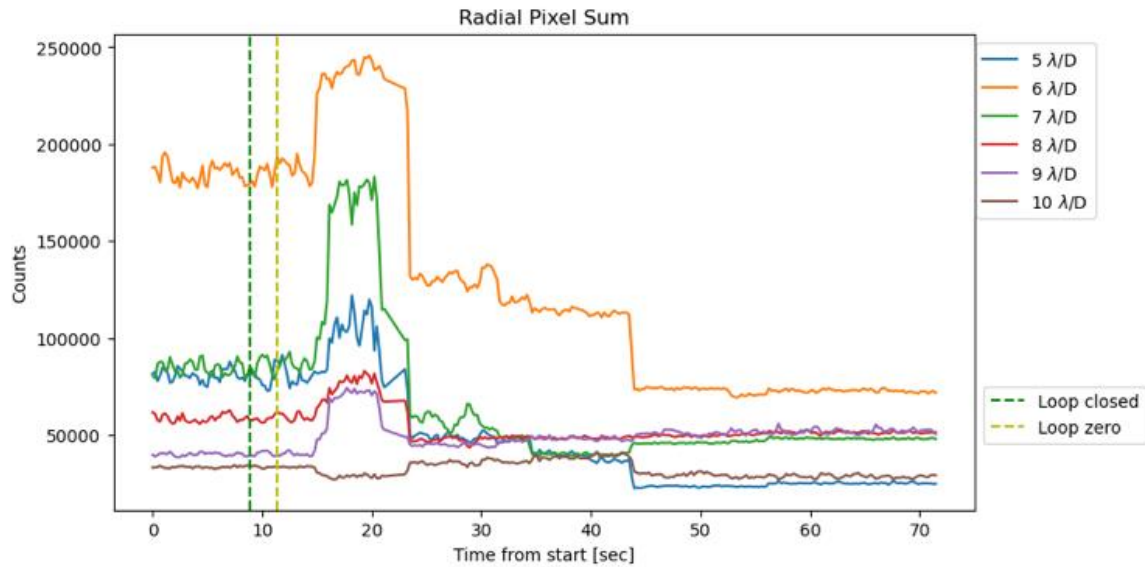


Figure 73. Radial pixel sums over the data acquisition period for lowfs-z-c test 1.

The running mean and standard deviation of the radial pixel sums are given in Figures 74 and 75.

The means and standard deviations shown are calculated using a 10-image sample size, shifting one image for each step.

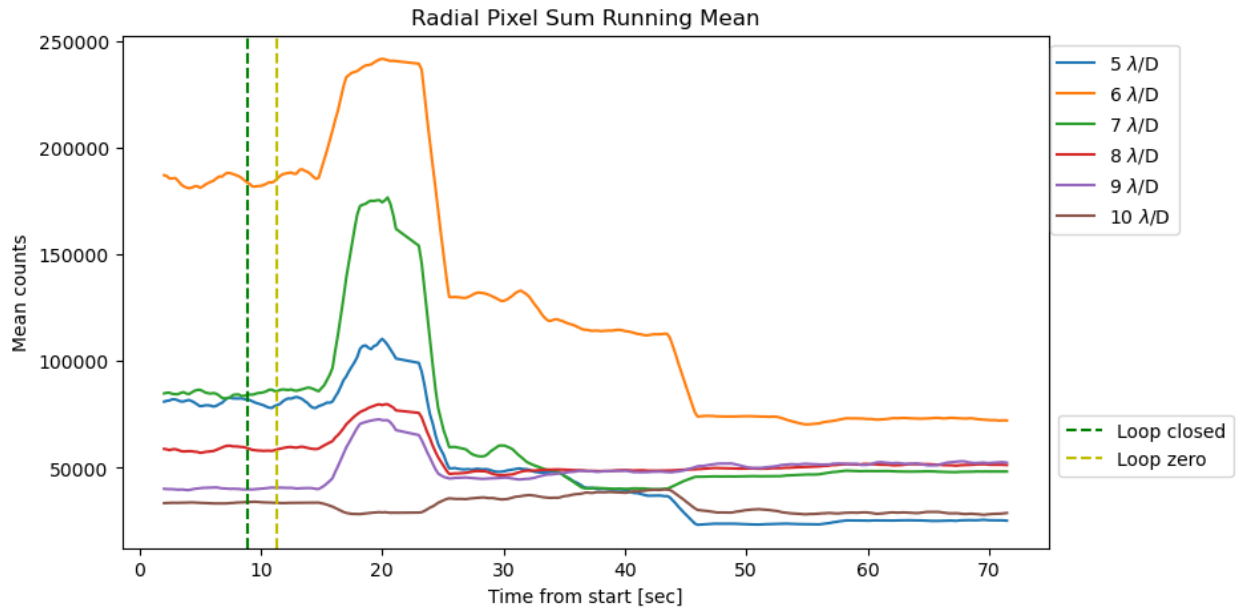


Figure 74. Running mean of radial pixel sums over the data acquisition period for *lowfs-z-c test 1*.

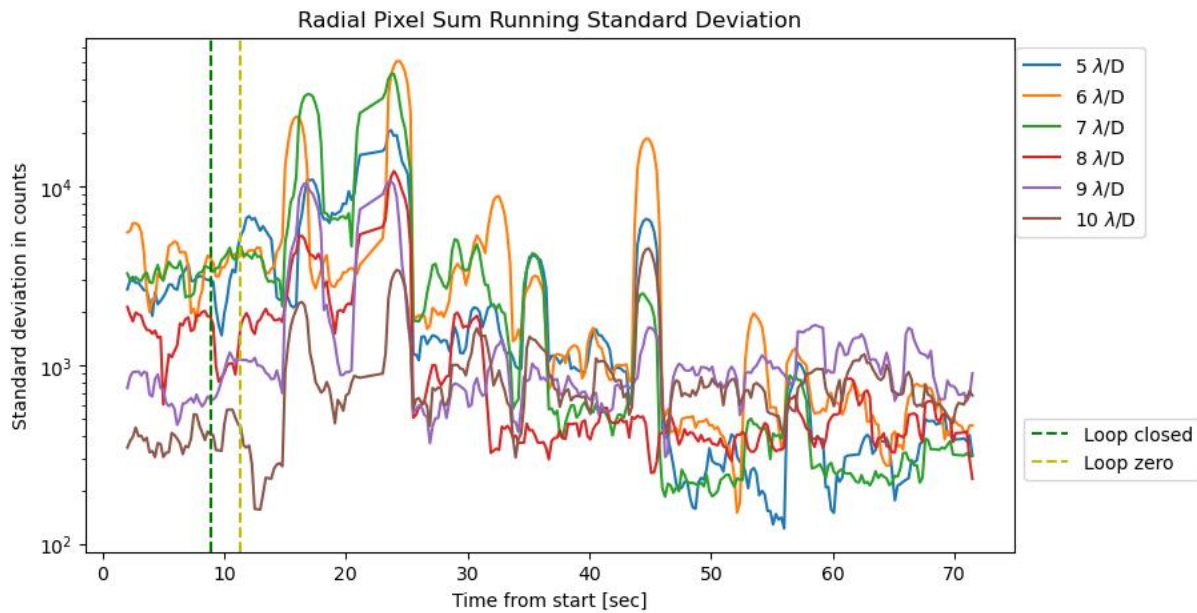


Figure 75. Running standard deviation of radial pixel sums over the data acquisition period for *lowfs-z-c test 1*.

The decrease in radial pixel sums agrees with the increase in sparkle core sums as seen in Figures 71 and 73. The greatest effect is seen at $6 \lambda/D$ (~60% decrease) and $7 \lambda/D$ (~37.5% decrease) which is expected as these are the areas of the coronagraphic image that are most

influenced by CLOWFS&C. Figure 75 also indicates that the temporal variations in radial pixel sums (relative contrast) decrease once the loop is closed. In other words, the coronagraphic image is shown to be more stable at low radial distances from the central PSF when the CLOWFS&C loop is closed.

The MSE metric on the WFS images also suggests loop convergence as shown in Figure 76.

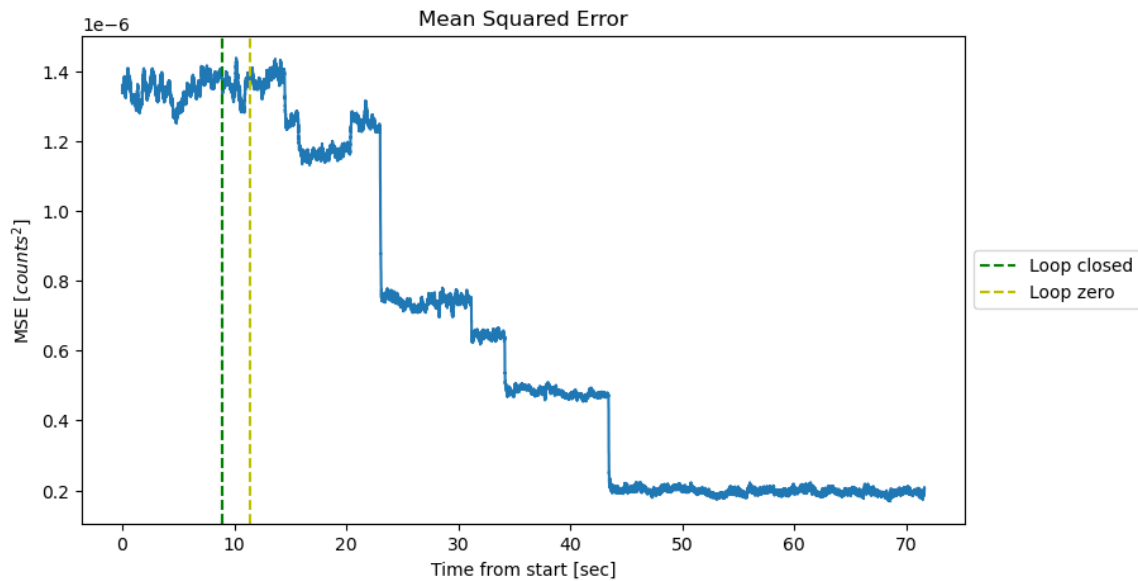


Figure 76. Mean squared error of the WFS images over the data acquisition period for lowfs-z-c test 1.

Figure 76 shows a ~84% decrease in MSE between open and closed loop operation. The modal correction coefficients further suggest loop convergence as seen in Figure 77.

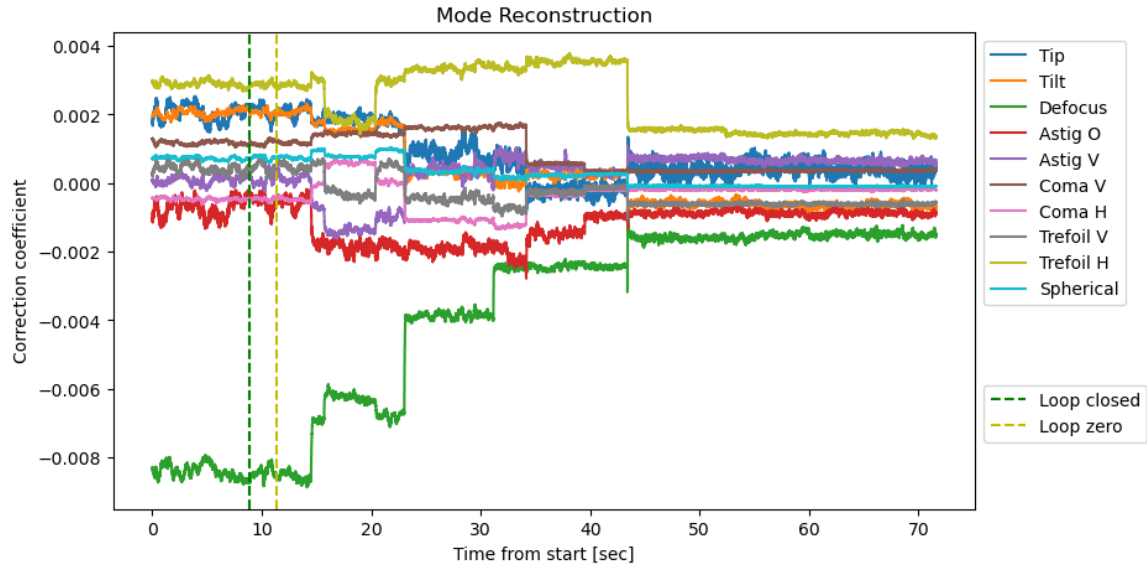


Figure 77. Mode reconstruction over data acquisition period for lowfs-z-c test 1.

5.3.3.2 Lowfs-z-c test 2:

For test 2, the lowfs-z-c calibration is tested without injecting any wavefront errors into the system but was performed after alignment had been lost from when the calibration was taken. The MagAO-X small Lyot stop is in place for this test. The loop control parameters for the data set are given in Figure 78.

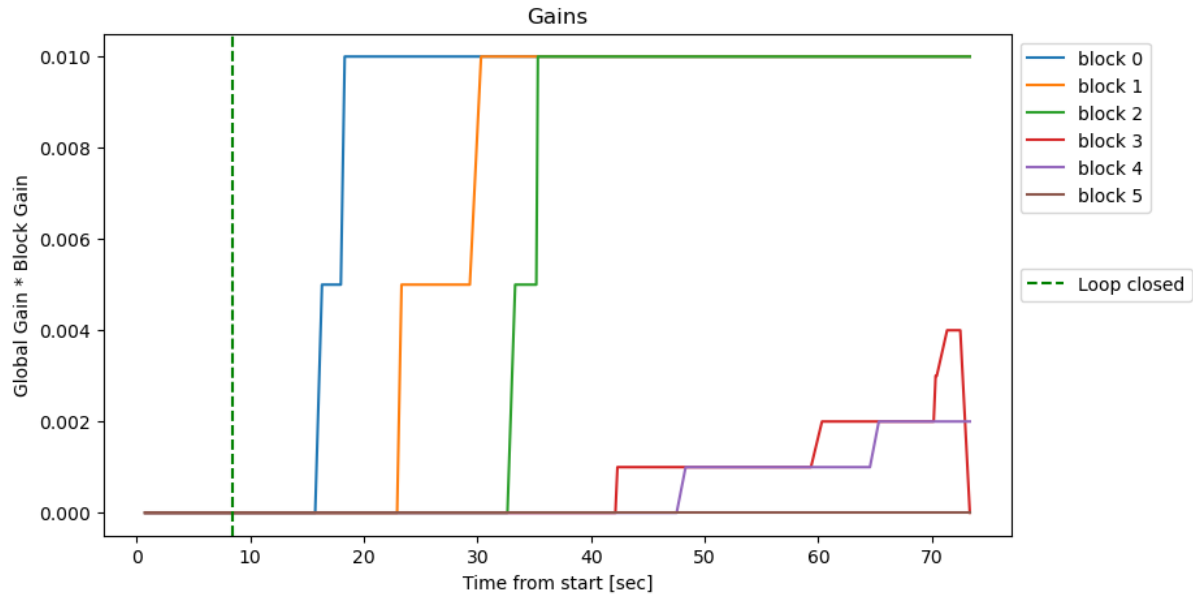


Figure 78. Global gain, block gains, and leak applied to the LOWFS&C loop for lowfs-z-c test 2.

It is seen in Figure 74 that all gains are raised by the end of the data acquisition meaning the CLOWFS&C loop is closed on 34 modes in test 2. The median coronagraphic image for the data set is shown in Figure 79.

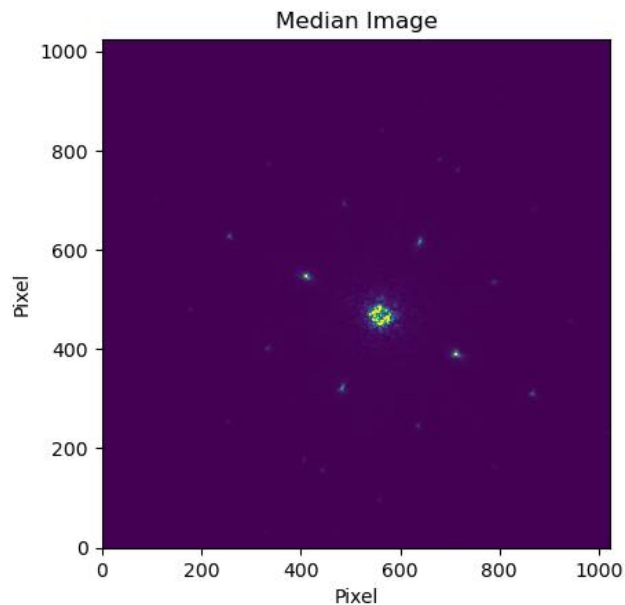


Figure 79. Median image for the lowfs-z-c test 2.

The sparkle cores used to monitor relative change in Strehl are shown in Figure 80.

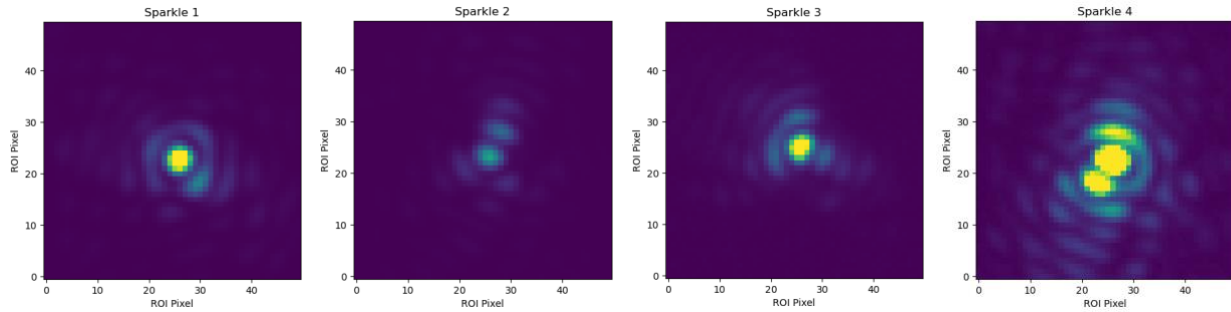


Figure 80. Sparkle PSFs used for monitoring relative change in Strehl for lowfs-z-c test 2.

Figure 81 shows the sparkle core sums over the data acquisition period. The values are very similar for all sparkles such that the plot lines are indistinguishable from one another.

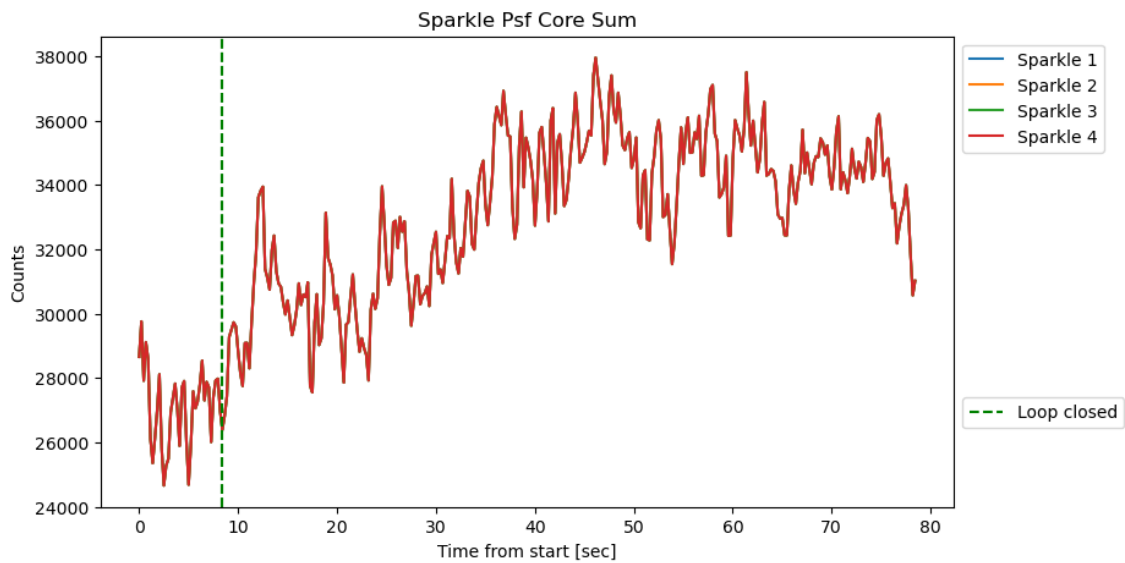


Figure 81. Sparkle PSF core sums over the data acquisition period for lowfs-z-c test 2.

The PSF cores in Figure 81 suggest a relative increase in Strehl of roughly 30%.

Pixel sums are taken at several radial distances on the coronagraphic image as indicated in Figure 82.

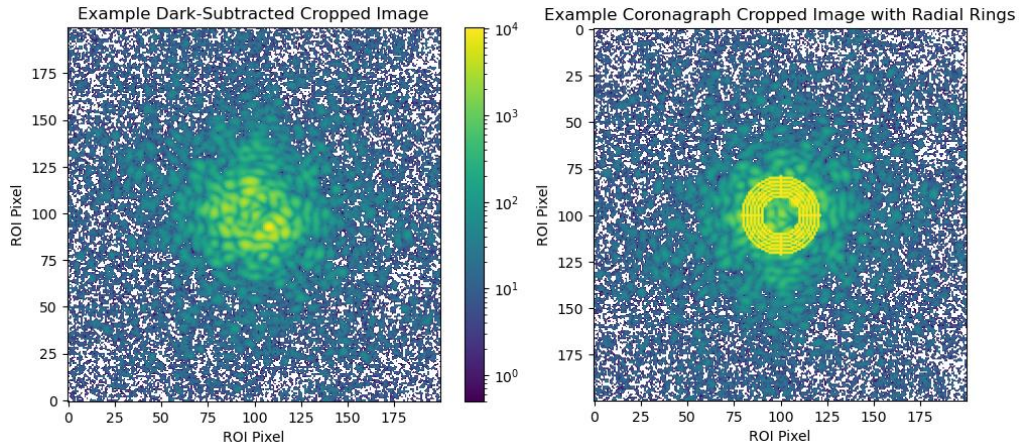


Figure 82. Example dark subtracted cropped image and image with indication of radial pixel sum locations for lowfs-z-c test 2.

The resulting radial sums are given in Figure 83.

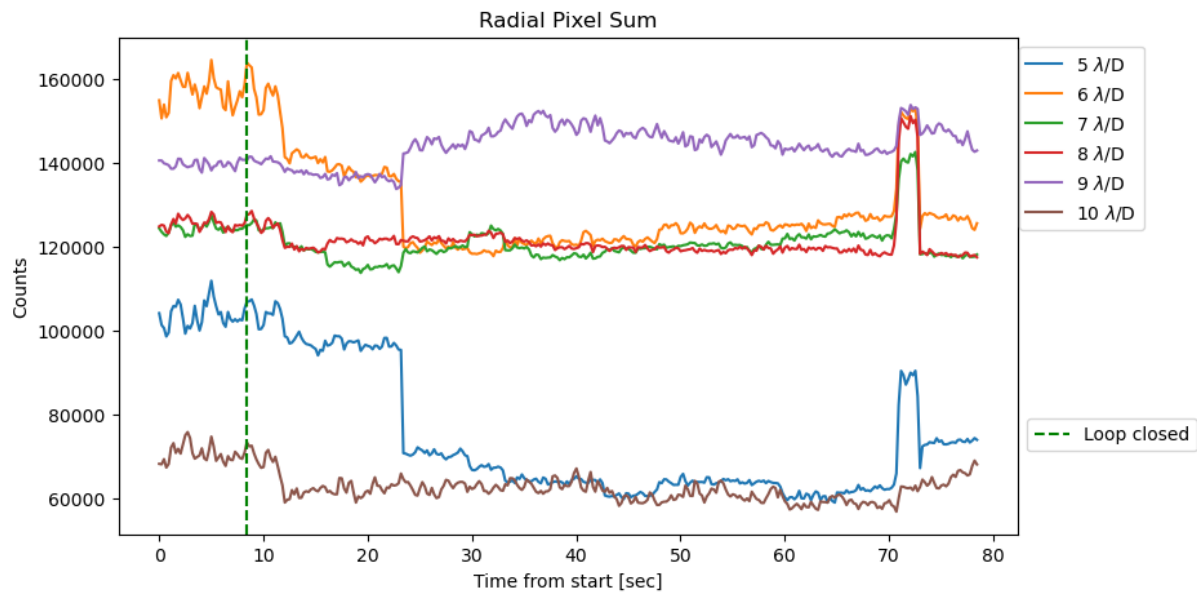


Figure 83. Radial pixel sums over the data acquisition period for lowfs-z-c test 2.

The running mean and standard deviation of the radial pixel sums are given in Figures 84 and 85.

The means and standard deviations shown are calculated using a 10-image sample size, shifting one image for each step.

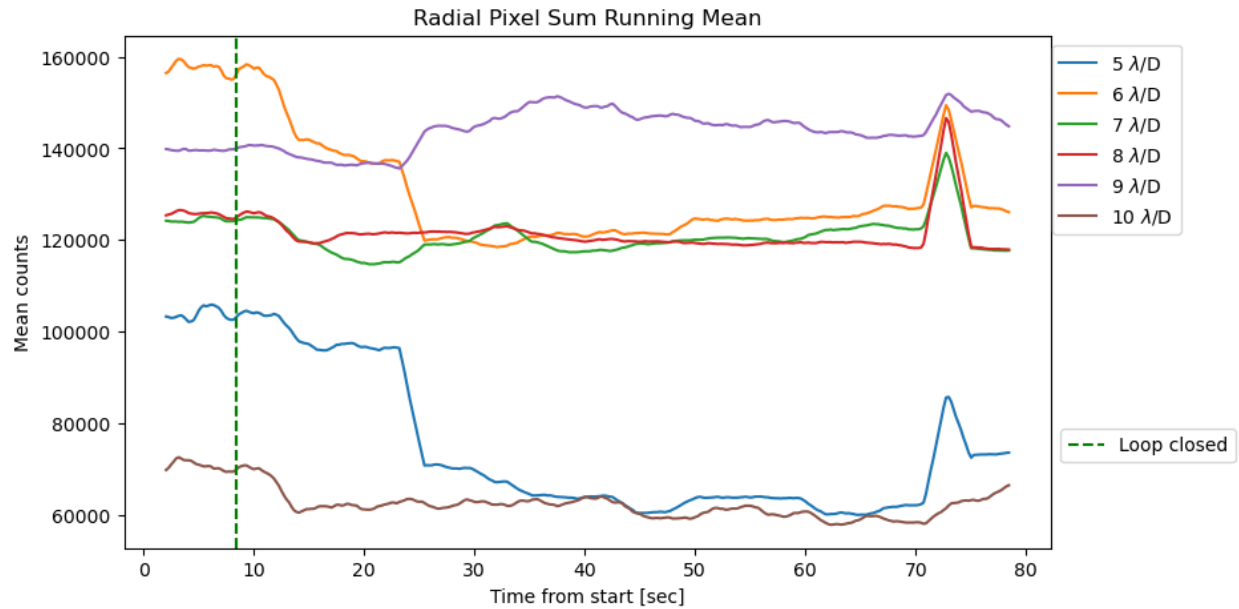


Figure 84. Running mean of radial pixel sums over the data acquisition period for lowfs-z-c test 2.

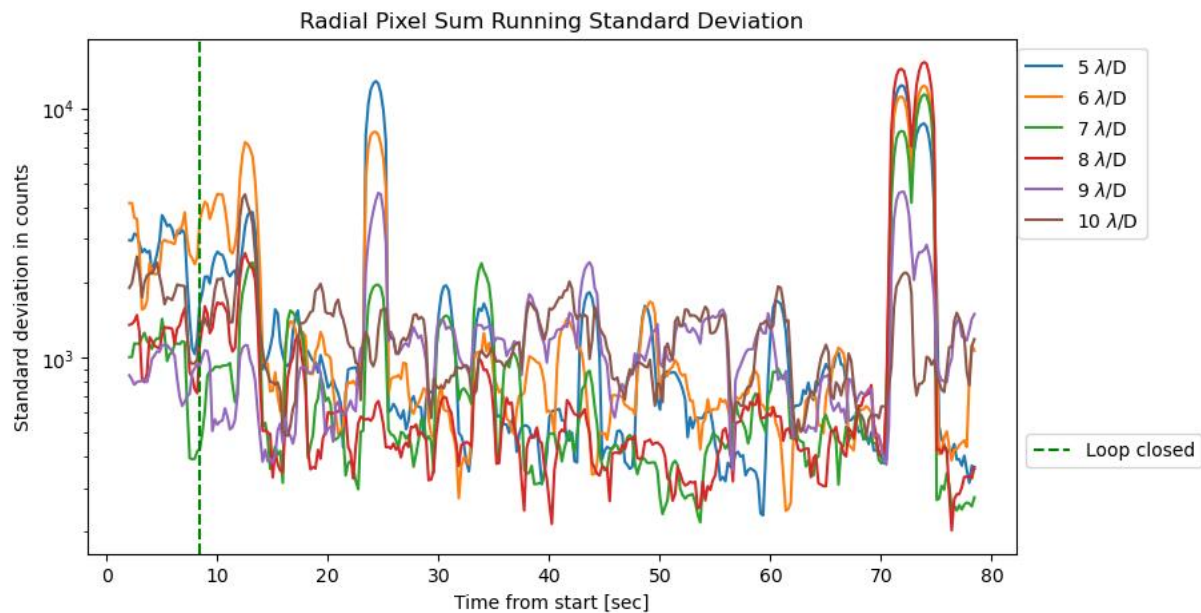


Figure 85. Running standard deviation of radial pixel sums over the data acquisition period for lowfs-z-c test 2.

Figure 83 indicates that the CLOWFS&C loop improved the contrast of coronagraphic image at $5 \lambda/D$ (~25% decrease) and $6 \lambda/D$ (~21.5% decrease), but caused an increase in the radial pixel sum at 9 and $10 \lambda/D$. The spike at the 70 second mark is likely due to increasing

gains too high in block 3. Figure 85 indicates that temporal stability is clearly improved at $5 \lambda/D$ and $6 \lambda/D$ when the loop is closed. The behavior seen from evaluating the MSE and modal reconstruction metrics of the WFS images agree with what is seen in the coronagraphic images.

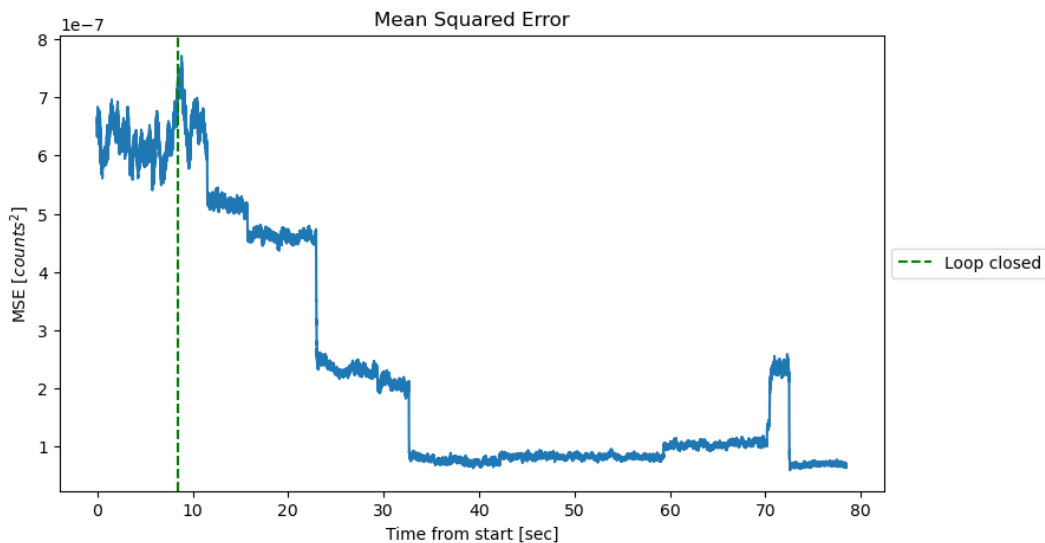


Figure 86. Mean squared error of WFS images over the data acquisition period for lowfs-z-c test 2.

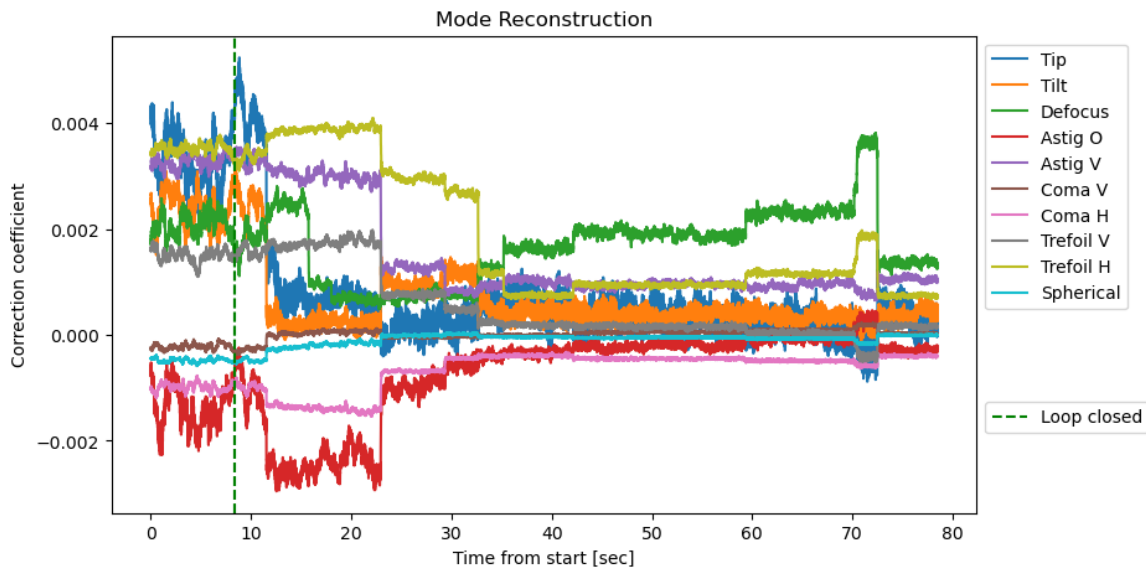


Figure 87. Mode reconstruction over data acquisition period for lowfs-z-c test 2.

The MSE decreased by roughly 84% from the start to 50 seconds into data acquisition.

5.3.3.3 Conclusions

From the tests performed on the lowfs-z-c calibration, it is predicted that this CLOWFS&C loop will be successful on sky under linear conditions. It also confirms the practice of limiting control of higher order modes in order maintain loop convergence.

5.3.4 Additional notes

Several other calibrations were taken for the 2023A observing run after MagAO-X was moved to the Nasymth platform of the Magellan Clay (see Appendix D). Due to time constraints, these calibrations were often not taken after PSF optimizations as rigorous as what was done for the sci2-H α and lowfs-z calibrations (rigorous optimization taking several hours). However, a less rigorous eye doctor algorithm was run before every calibration to ensure the science PSFs were as optimal as time allowed.

All non-coronagraphic calibrations were tested by running similar experiments as shown with the in-lab tests wherein wavefront errors would be intentionally added to the system and the LOWFS&C loop would be closed on the lab source. The performance was monitored, and this allowed some calibrations to be deemed un-fit for on-sky observations. Likely causes for calibrations to behave poorly include:

1. PSF drifts during the time a calibration was taken.
2. Insufficient PSF optimization prior to the calibration.
3. Insufficient signal when performing the calibration.

5.4 On-sky Results 2023A

Several tests were performed on-sky to evaluate the performance of LOWFS&C calibrations. As was suggested by lab-source tests, the gain values were often initially set low and walked up. The ‘loop zero’ function was often used in conjunction with lowering gains to reset LOWFS&C corrections if the loop began to run away. Increasing gains on one block at a time, starting with the lowest modes and working up, was helpful in keeping a loop stable on-sky. The following sections relay on-sky tests performed to evaluate the performance of several LOWFS&C calibrations as shown in Table 5.

Table 5. Details for on-sky tested calibrations including the camera used, filter used, and number of modes corresponding to each mode block.

Name	Camera	Filter	Total # of Modes	Number of Modes in Block					
				Block 0	Block 1	Block 2	Block 3	Block 4	Block 5
sci2-H α	camsci2	H α -narrow	38	2	1	6	9	10	10
sci1-r	camsci1	r	41	2	1	6	10	14	8
lowfs-z-c	camlowfs	z	34	2	1	5	6	11	9

The sci2-H α , lowfs-z, and sci1-r calibrations listed in Table 5 are non-coronagraphic. The lowfs-z-c calibration was taken with the $6 \lambda/D$ diameter reflective Lyot focal plane mask aligned.

The reference images and bright field masks corresponding to the calibrations in Table 5 are given in Figures 88 - 90:

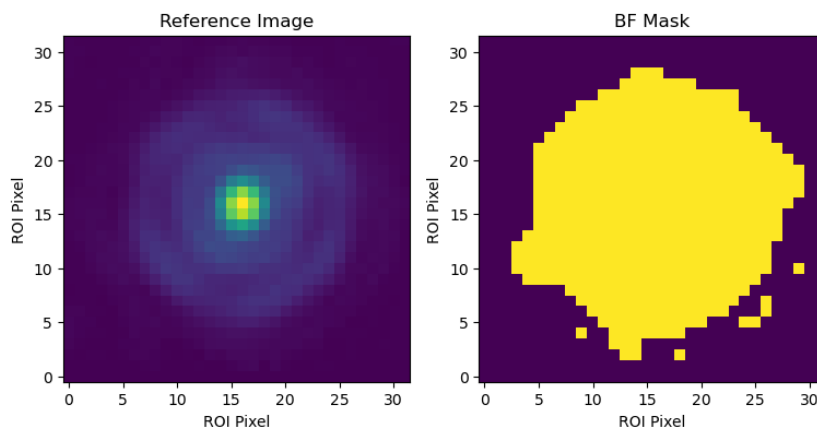


Figure 88. Reference image and bright field mask for the sci2-H α calibration.

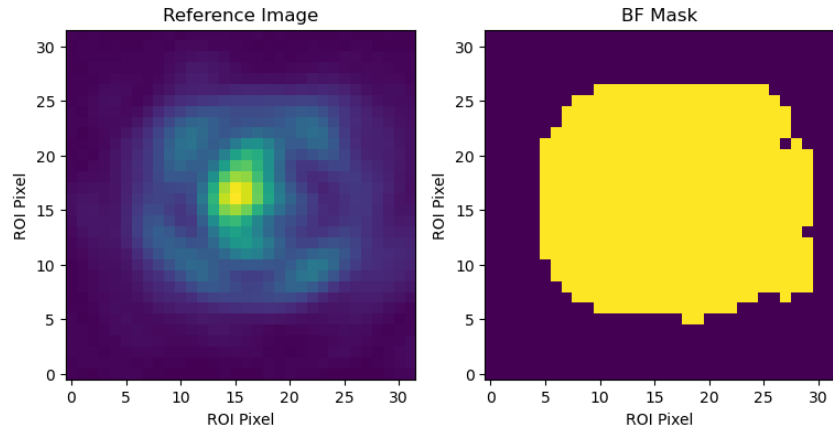


Figure 89. Reference image and bright field mask for the sci1-r calibration.

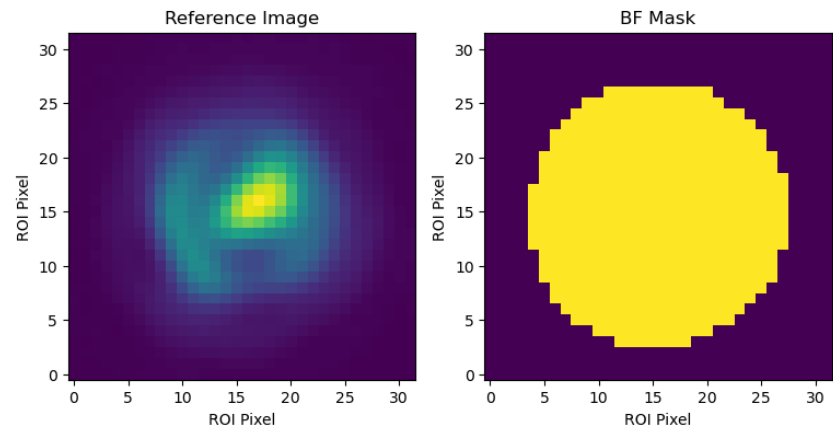


Figure 90. Reference image and bright field mask for the lowfs-z-c calibration.

For non-coronagraphic calibrations, in-focus PSF science camera images and WFS images are evaluated to determine performance. For an in-focus PSF image stack, a median image is found and the brightest pixel in that image is used to center and crop the entire stack. A 5x5 pixel region is isolated around the median-defined center for each cropped image in the stack and the sum of those pixels is monitored throughout a data acquisition period. This metric informs on relative changes in Strehl, an increase indicating positive LOWFS&C loop performance. WFS images are evaluated using the MSE and mode reconstruction metrics as done with the in lab-tests outlined in the previous section.

For coronagraphic calibrations, high contrast science camera images and WFS images are evaluated to determine performance. The primary loop's 2k DM is used to induce PSF copies (referred to as sparkles) surrounding the nominal PSF location. A median image of the high-contrast image stack is found, and the center of each sparkle is determined by isolating a small ROI around it and finding the location of the peak pixel value. The x and y pixel centers for each sparkle is averaged to estimate the center of the PSF in the full high-contrast images, and those images are stacked and cropped around that coordinate. The sparkle cores are used to monitor relative Strehl throughout the data acquisition period. With this, rings of pixels at several λ/D locations of the high-contrast images are summed and monitored throughout data acquisition. The running mean and standard deviation of the radial sums is found to evaluate high contrast region stability. An increase in sparkle-core value and decrease in λ/D radial pixel sum indicate a positive LOWFS&C performance. A decrease in radial sum standard deviation indicates contrast stability. The WFS images are again evaluated with the MSE and mode reconstruction metrics.

Several on-sky data sets were taken during the 2023A run, but only a handful are presented in this section. Any data that did not have a corresponding proper dark taken at the time of data acquisition uses a dark image estimation. The estimation is made by finding the median pixel value for a 1-pixel wide border around the median image from the stack, and that value is subtracted everywhere from all images in the stack.

5.4.1 On-sky performance of LOWFS&C for PSF optimization

The following on-sky results correspond to the sci2-H α and lowfs-r calibrations used to optimize PSFs before science observations. The LOWFS&C corrective loop is closed to correct for static and quasi-static NCPAs and is then opened to return PSF light to in-focus science cameras. The corrective shape is held on the NCPC DM following the corrective loop, meaning

there should be no ‘loop zero’ commands sent once the DM corrective shape is considered optimal (though is not necessarily relevant for the following data). Because the loop is aiming to correct for static and quasi-static NCPAs, the corrective loop can be run at low speeds (<1 Hz) to average out high frequency atmospheric turbulence. All camera configurations for each evaluation are summarized in Appendix C.

5.4.1.1 Sci2-H α on-sky test:

The object HD34700 was used to evaluate LOWFS&C using the sci2-H α calibration on 2023-03-08. Camsci2 was used with H α -continuum filter to monitor an in-focus PSF. The Differential Image Motion Seeing Monitor (DIMM) reported astronomical seeing of 0.75 throughout the data set. The loop control parameters over the data acquisition period are given in Figure 91.

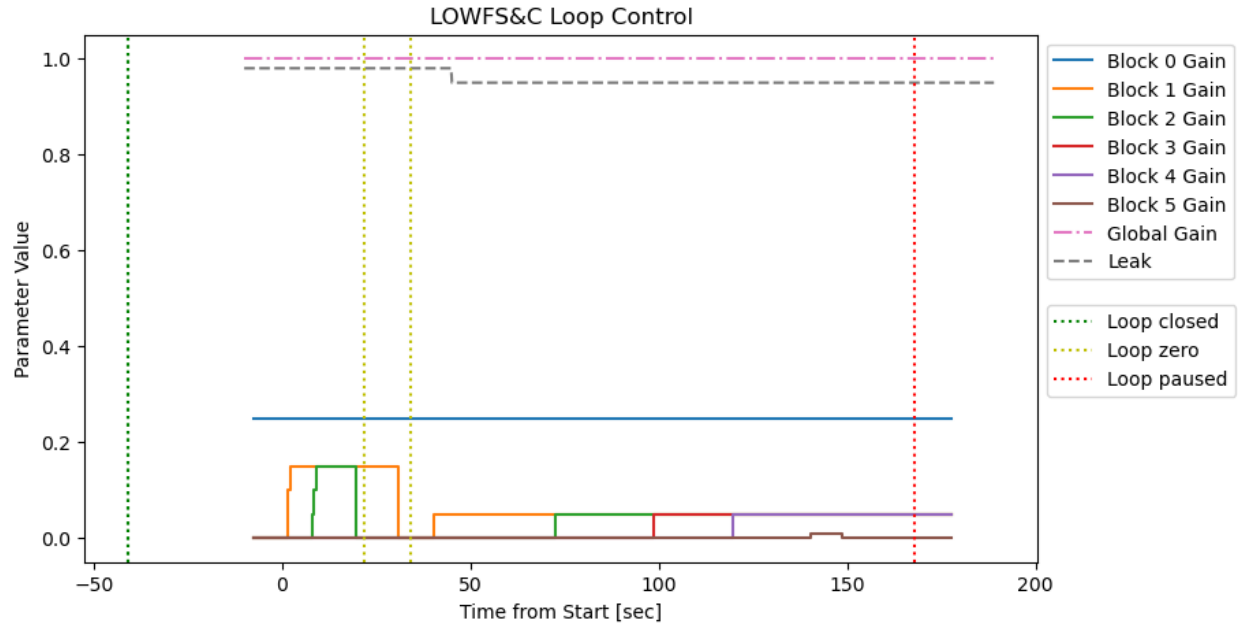


Figure 91. Loop control parameters over data acquisition time for the sci2-H α on-sky test.

The loop control parameters indicate the loop was closed before data acquisition. The tip/tilt, defocus, and astigmatism-spherical blocks are increased initially and then dropped and brought

up again slowly. The higher orders are brought up starting around 100 seconds into data acquisition, with block 4 initiated around 120 seconds in. The gain blocks indicate that by the end of data acquisition the loop was closed on 31 modes.

Figure 92 shows example full-frame and cropped in-focus science images from the data stack.

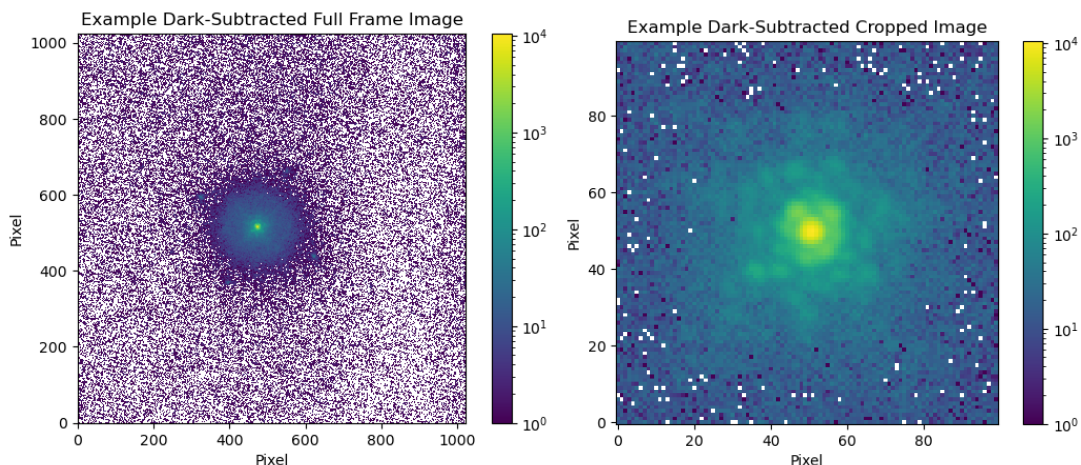


Figure 92. Dark subtracted images from the science image cube for the sci2-H α on-sky test.

Figure 93 shows the PSF core sum over the data acquisition time.

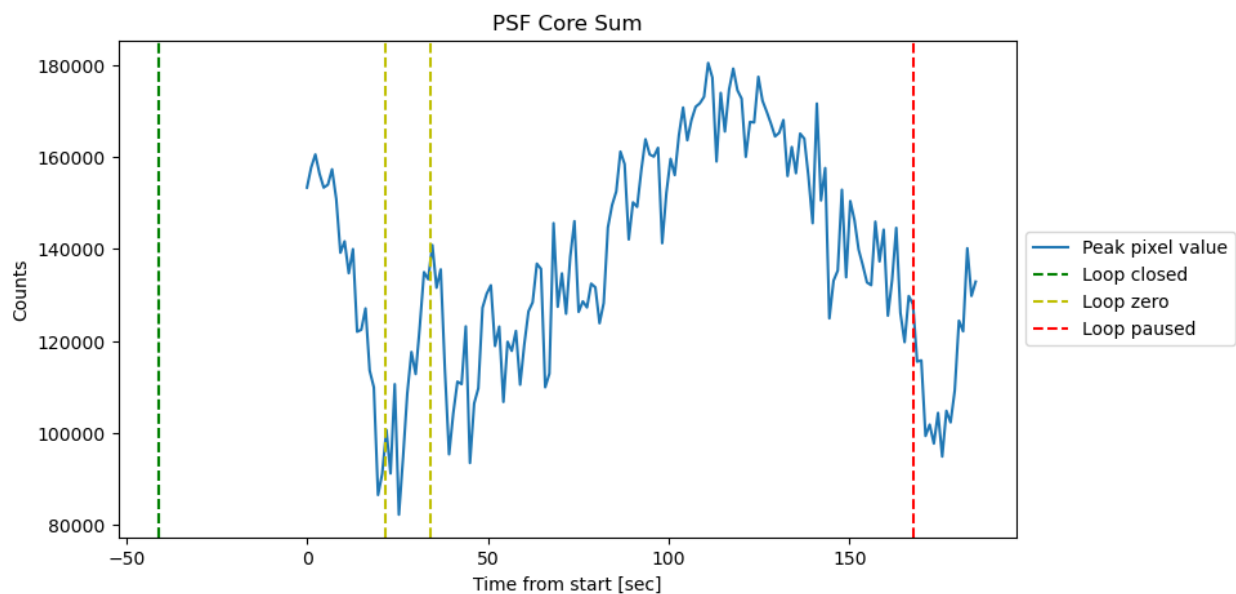


Figure 93. 5x5 ROI PSF pixel sum over data acquisition time for the sci2-H α on-sky test.

The PSF core sums indicate good correction after the loop was zeroed and the low order gains were brought up slowly. The relative Strehl was increased by roughly 20% over 90 seconds after the loop was initially zeroed. However, around 120 seconds (when block 4 was brought up), the PSF core sum starts to decrease. It is also seen in Figure 94 that the MSE of the WFS images begins to increase around 120 seconds as well.

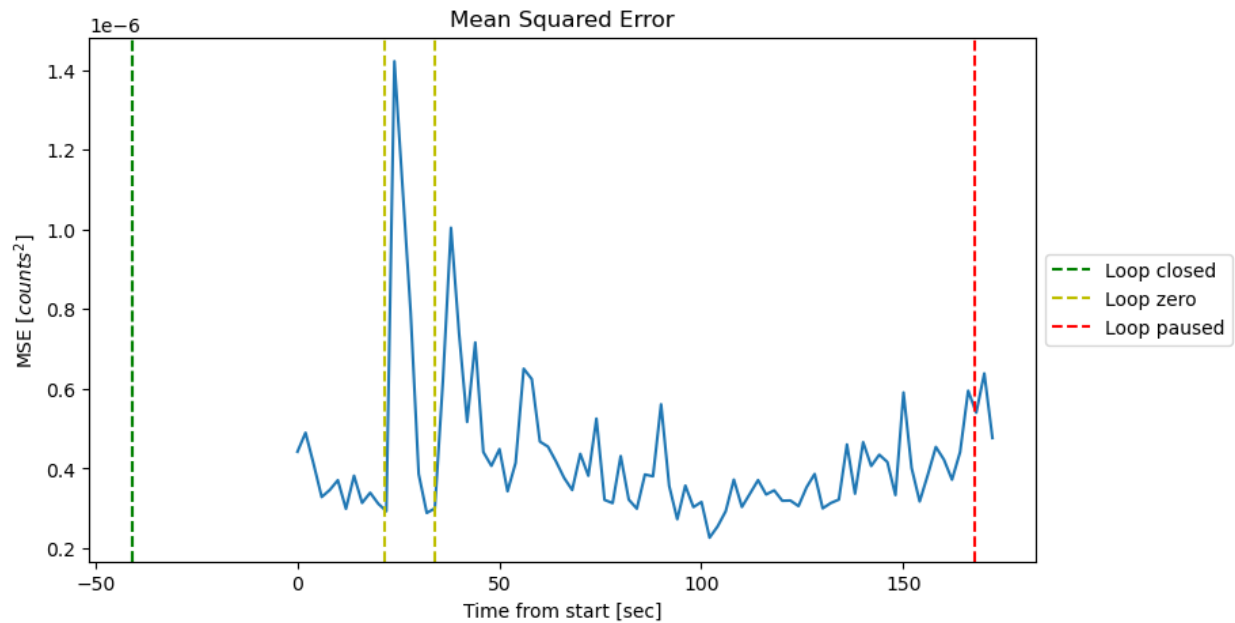


Figure 94. Mean squared error over data acquisition time for the sci2-H α on-sky test.

This indicates that trying to correct modes 19-29 is over-driving the system (causing the loop to diverge). The modal coefficients show convergence following the ‘loop zero’ commands in Figure 95.

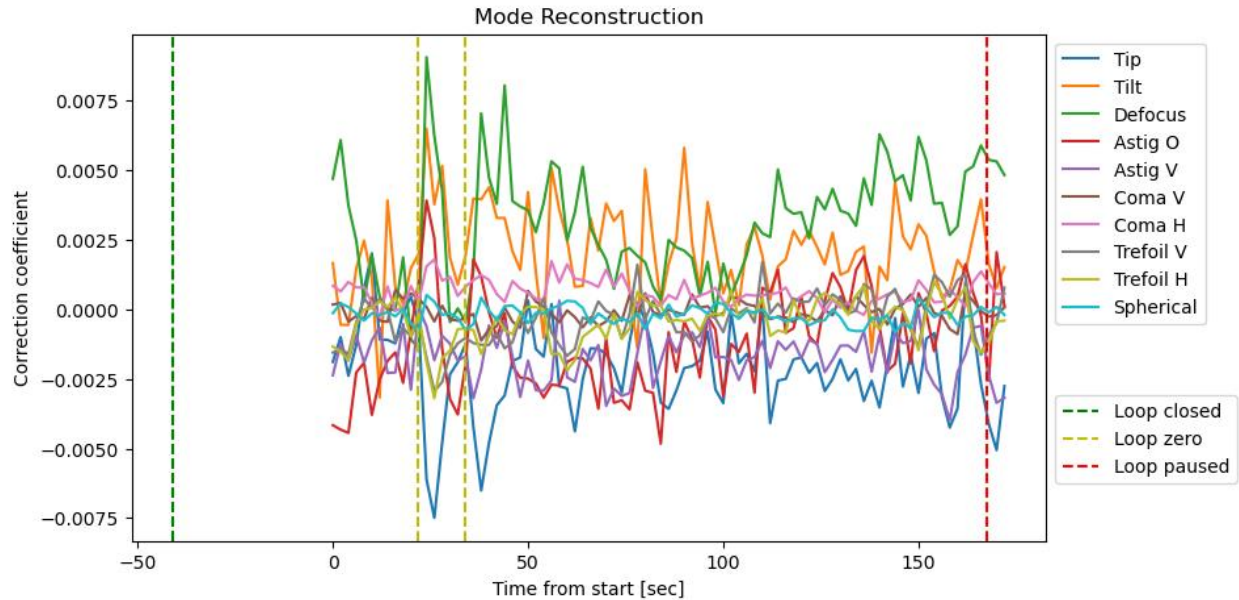


Figure 95. Correction coefficients for the first 10 Zernike modes over the data acquisition period of the *sci2-H α* on-sky test.

Figure 95 only shows mode reconstruction for the first 10 modes, but the divergence following ~ 120 seconds suggests that the reconstruction of these modes is affected by the over-driving of the higher order modes.

5.4.1.2 *Sci1-r* on-sky test:

The object tet01OriC was used to evaluate LOWFS&C using the *sci1-r* calibration on 2023-03-07. Camsci2 was used in r-band to monitor an in-focus PSF. The DIMM reported astronomical seeing starting at 0.63 at the beginning of the data set with a downward trend throughout the data set. The loop control parameters over the data acquisition period are given in Figure 96.

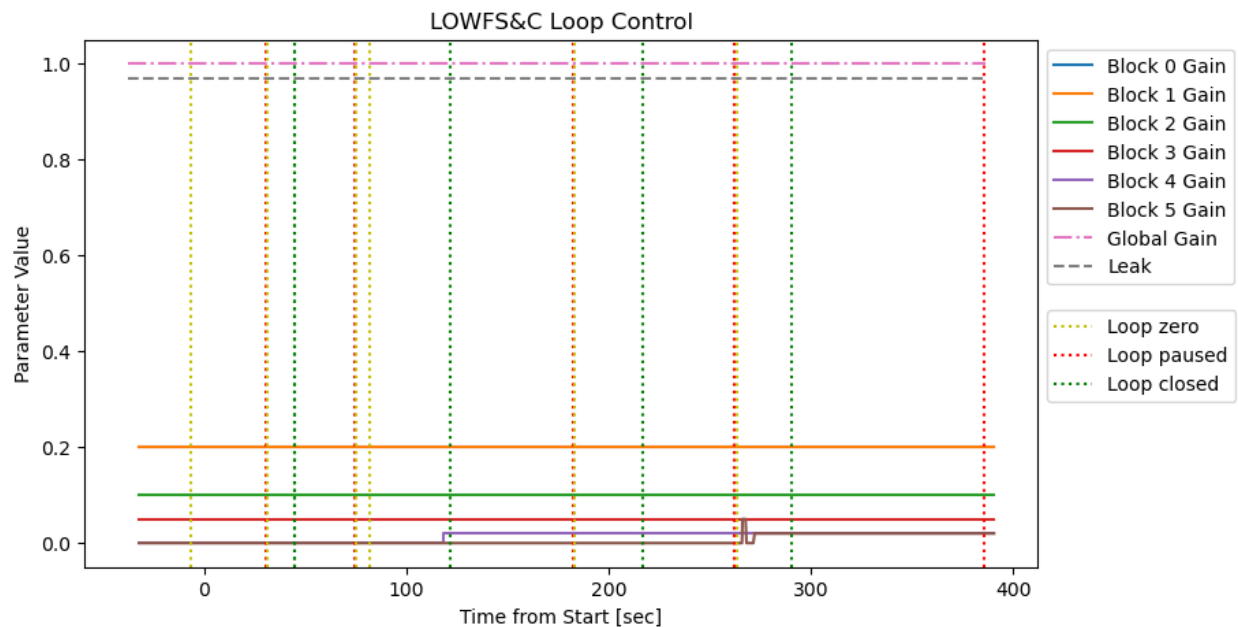


Figure 96. Loop control parameters over data acquisition time for the *sci1-r* on-sky test.

Blocks 0 and 1 overlap throughout the data set. The loop parameters indicate that there were several iterations of closing the loop with the several ‘loop zero’ commands. This data set was taken over a significantly longer time span than what was seen in the *sci2-H α* on-sky test (about 4 times as long). By the end of the observation, all block gains were raised meaning the loop was closed on 41 modes.

Figure 97 shows example full-frame and cropped in-focus science images from the data stack.

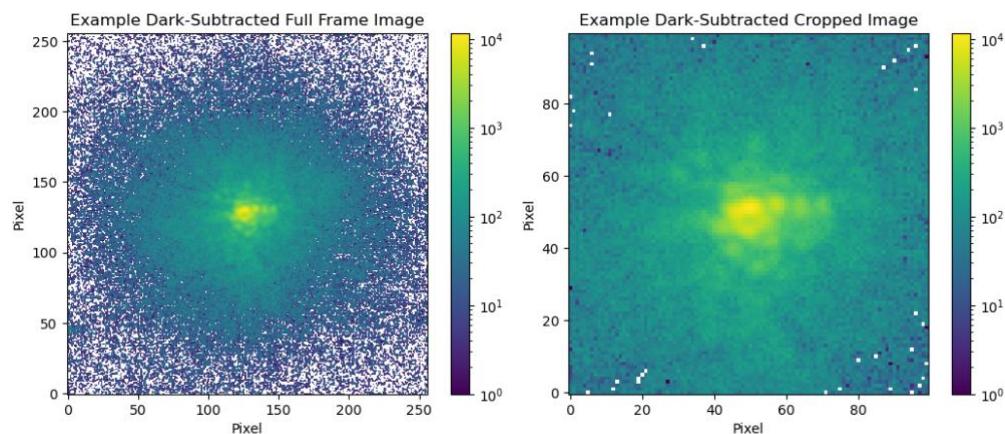


Figure 97. Dark subtracted images from the science image cube for the sci1-r on-sky test.

Figure 98 shows the PSF core sum over the data acquisition time.

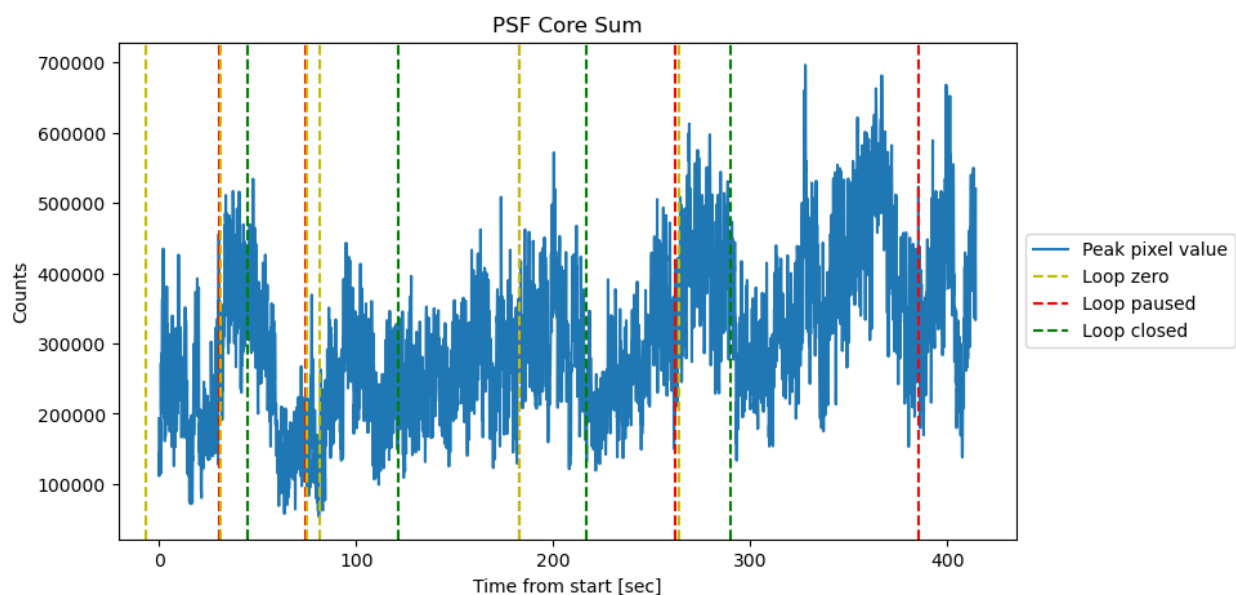


Figure 98. 5x5 ROI PSF pixel sum over data acquisition time for the sci1-r on-sky test.

It is not clear from this data set if the LOWFS&C loop was significantly improving the relative Strehl of the image or not. Because the astronomical seeing was decreasing through the observation, the general upward trend of the PSF through open and closed loop periods is likely influenced by improved performance of the HOWFS&C loop. However, the MSE metric of the

WFS images shown in Figure 99 clearly indicates that the WFS was converging towards the defocused reference PSF when the loop was closed.

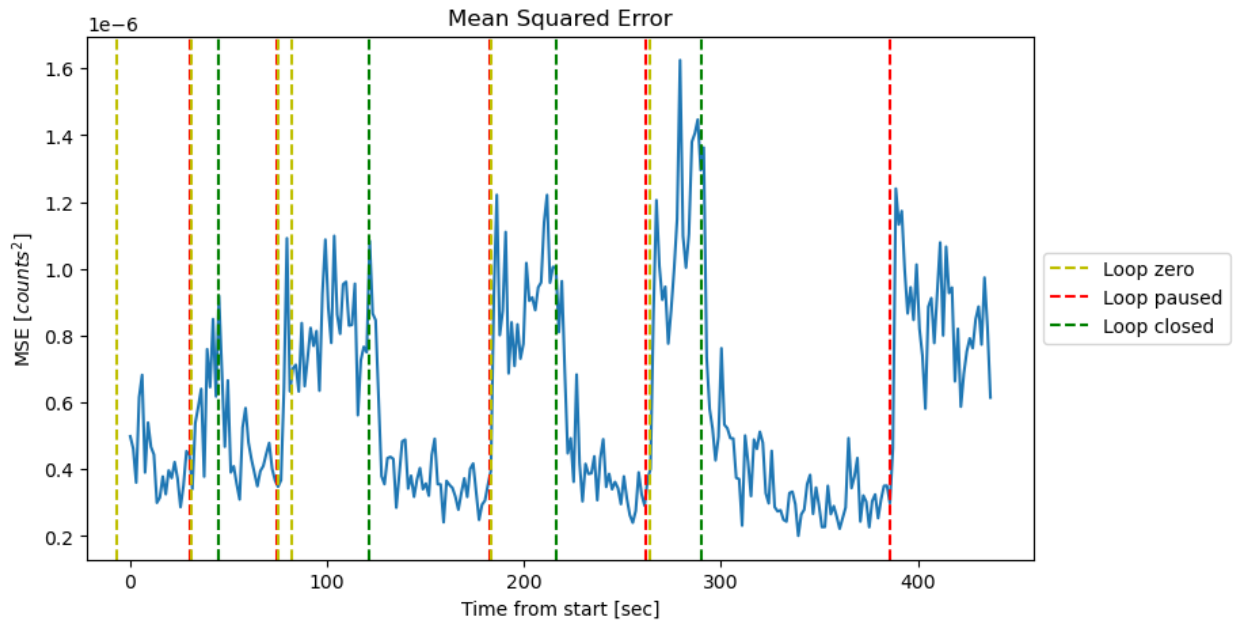


Figure 99. Mean squared error over data acquisition time for the sci1-r on-sky test.

The modal correction coefficients throughout the data set also indicate loop convergence towards the reference for some modes as seen in Figure 100.

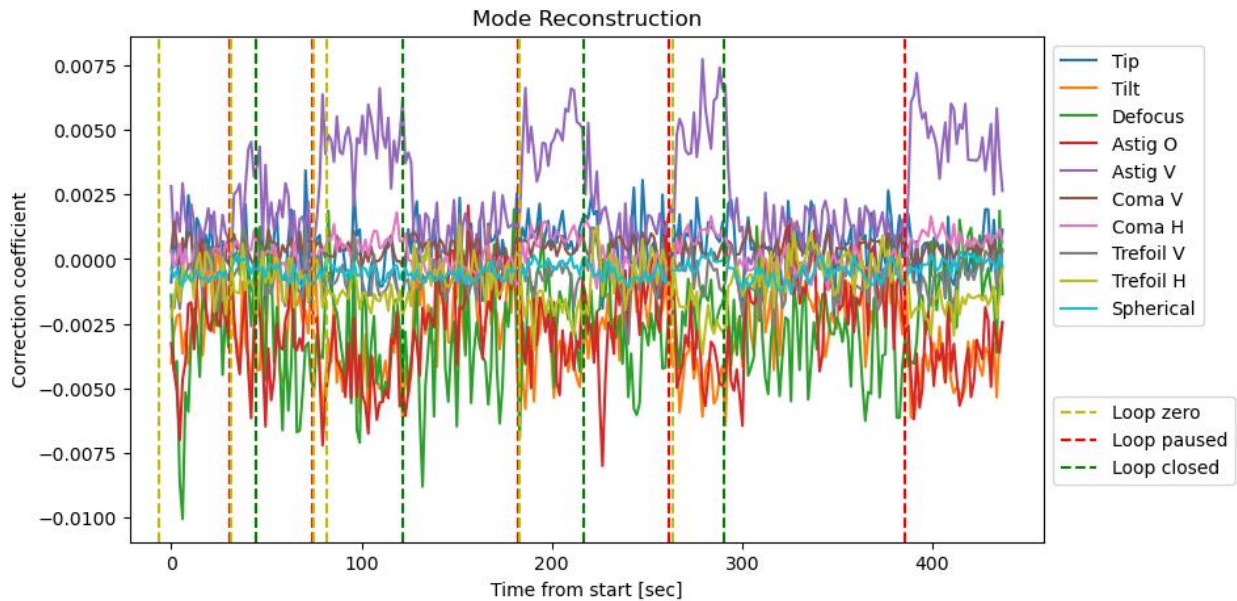


Figure 100. Correction coefficients for the first 10 Zernike modes over the data acquisition period of the sci1-r on-sky test.

Figure 100 reveals that defocus was not converging well when the loop was closed, possibly due to block 1 gain values set too high. Vertical and oblique astigmatism are shown to clearly converge when the loop was closed and were set to a gain value half of that of defocus. This data set is a good example of how implementing the LOWFS&C loops on sky as a MagAO-X user is non-trivial, as it is difficult to tell when the loop is improving MagAO-X performance or temporal changes in the environment like improved seeing is responsible.

5.4.2 On-sky performance of LOWFS&C for coronagraph control

The following on-sky results correspond to the lowfs-z-c calibration taken off the $6 \lambda/D$ diameter reflective Lyot FPM. The LOWFS&C corrective loop is closed to correct for static, quasi-static, and dynamic NCPAs during coronagraphic imaging with all coronagraphic elements in place (including Lyot Stop). Because the loop is aiming to correct for dynamic NCPAs, the corrective loops are run at high speeds (100 Hz). All camera parameters for the on-sky evaluations are summarized in Appendix C.

5.4.2.1 Lowfs-z-c on-sky test:

The Beta pic object was used to evaluate CLOWFS&C using the lowfs-z-c calibration on 2023-03-09. Camsci1 was used in i-band to monitor a coronagraphic image. The DIMM reported astronomical seeing starting at 0.43 throughout the data set. The loop control parameters over the data acquisition period are given in Figure 101.

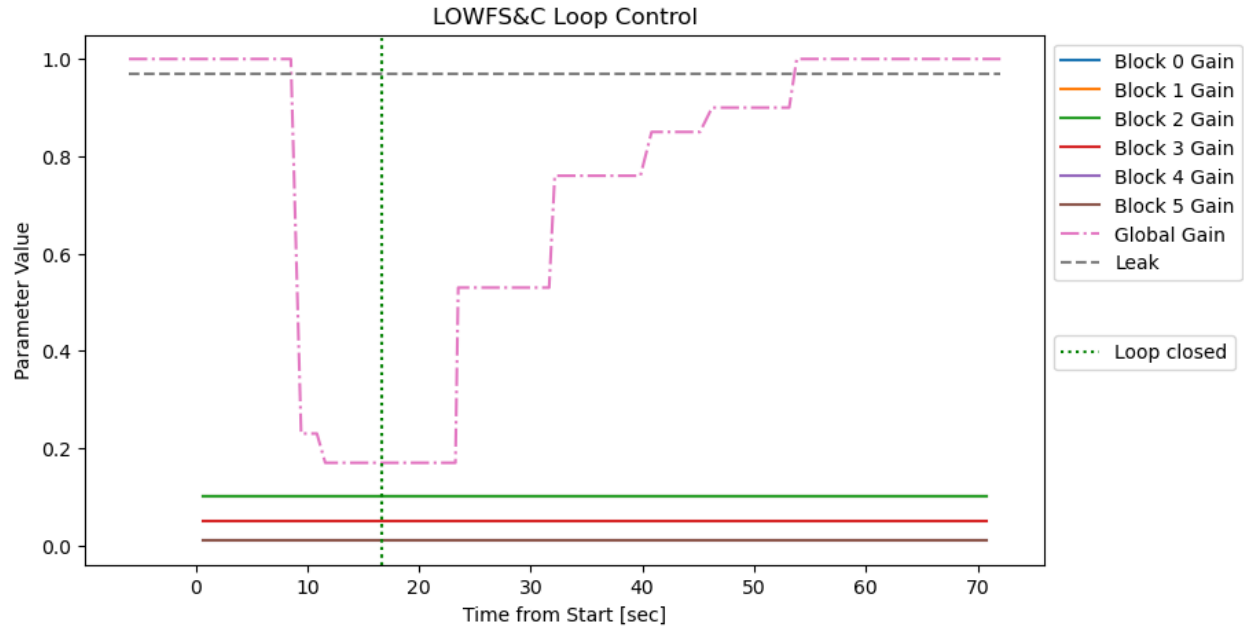


Figure 101. Loop control parameters for the data acquisition period of lowfs-z-c on-sky evaluation.

The median image from the science camera data set is given in Figure 102.

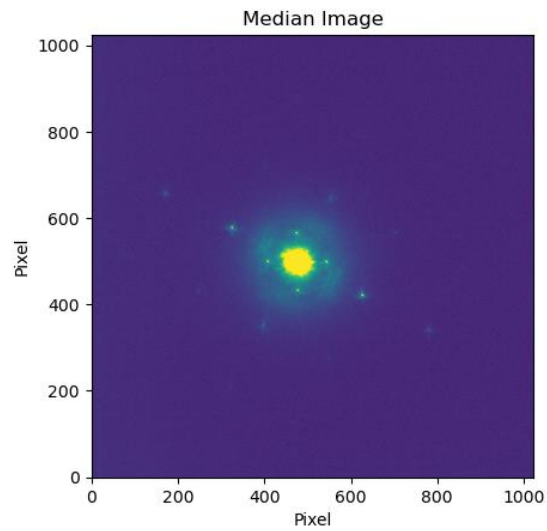


Figure 102. Median image for lowfs-z-c on-sky test.

The sparkles used to monitor relative changes in Strehl are given in Figure 97.

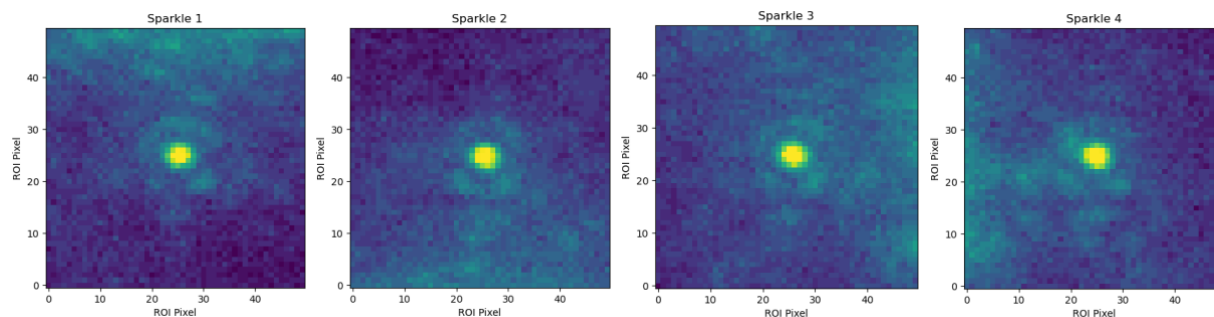


Figure 103. Sparkle PSF ROIs for lowfs-z-c on-sky test.

The sparkle core sums are reported over the data acquisition period in Figure 103. All the core sums have similar values throughout the data set such that the plot lines in Figure 100 are indistinguishable from one another.

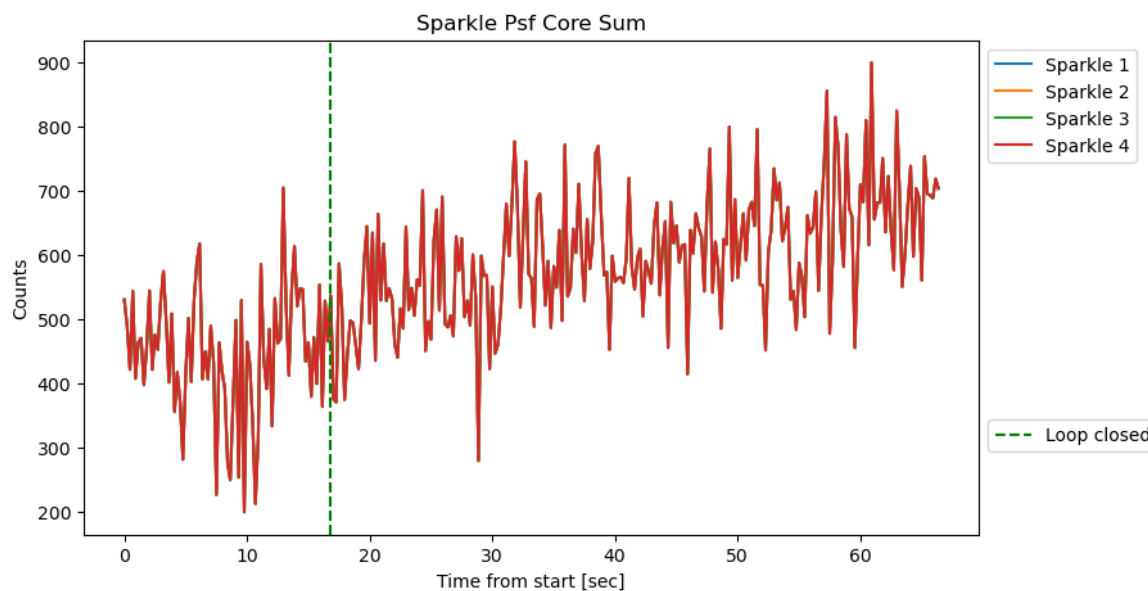


Figure 104. Sparkle core sums over the data acquisition period for the lowfs-z-c on-sky test.

The sparkle core sums indicate a $\sim 51\%$ increase in relative Strehl between the first and last 5 seconds of the data set.

The radial sums of several science image locations are evaluated. An example dark subtracted and cropped image is shown in Figure 105 along with indications of the radial sum locations.

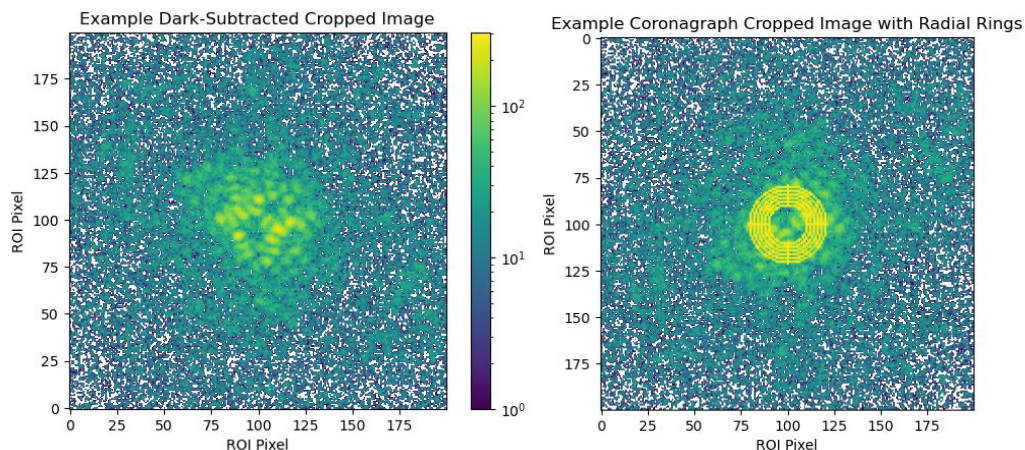


Figure 105. Example dark subtracted cropped image and image with indication of radial pixel sum locations for lowfs-z-c on-sky test.

The resulting radial sums are given in Figure 106.

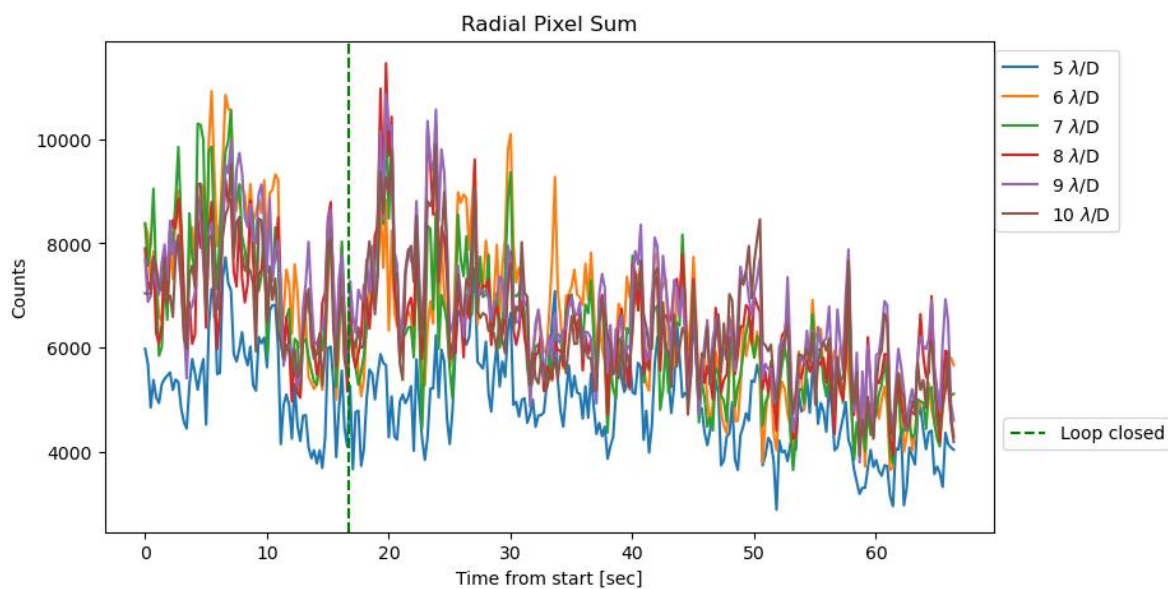


Figure 106. Radial pixel sums over the data acquisition period for the lowfs-z-c on-sky test.

The running mean and standard deviation of the radial pixel sums are given in Figures 107 and 108. The means and standard deviations shown are calculated using a 20-image sample size, shifting one image for each step.

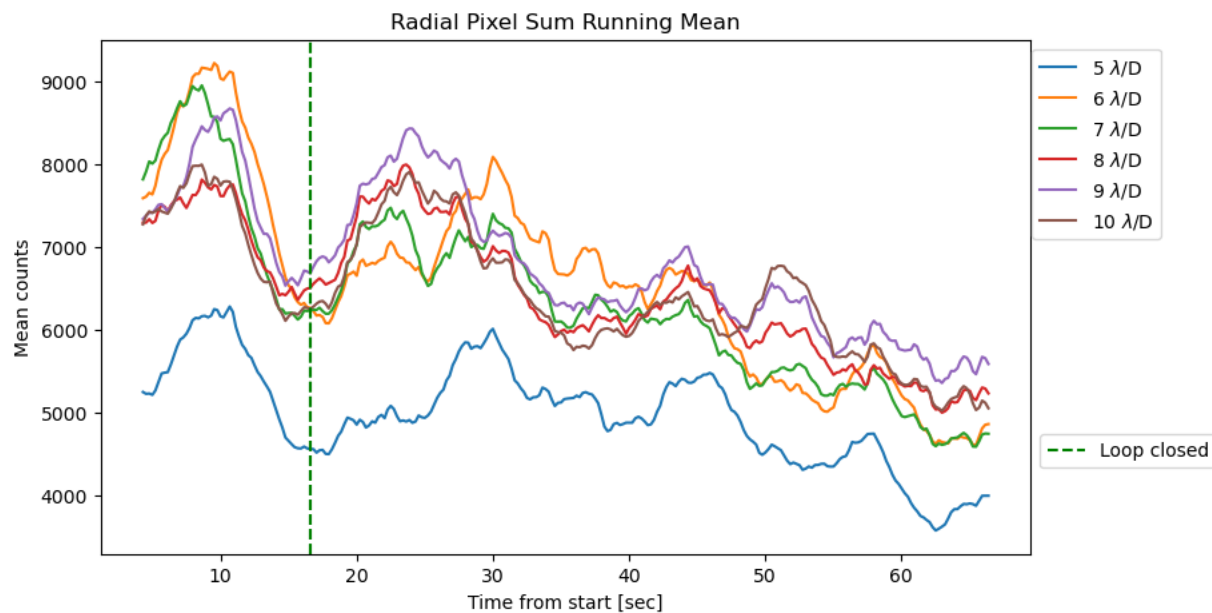


Figure 107. Running mean of radial pixel sums over the data acquisition period for lowfs-z-c on-sky test.

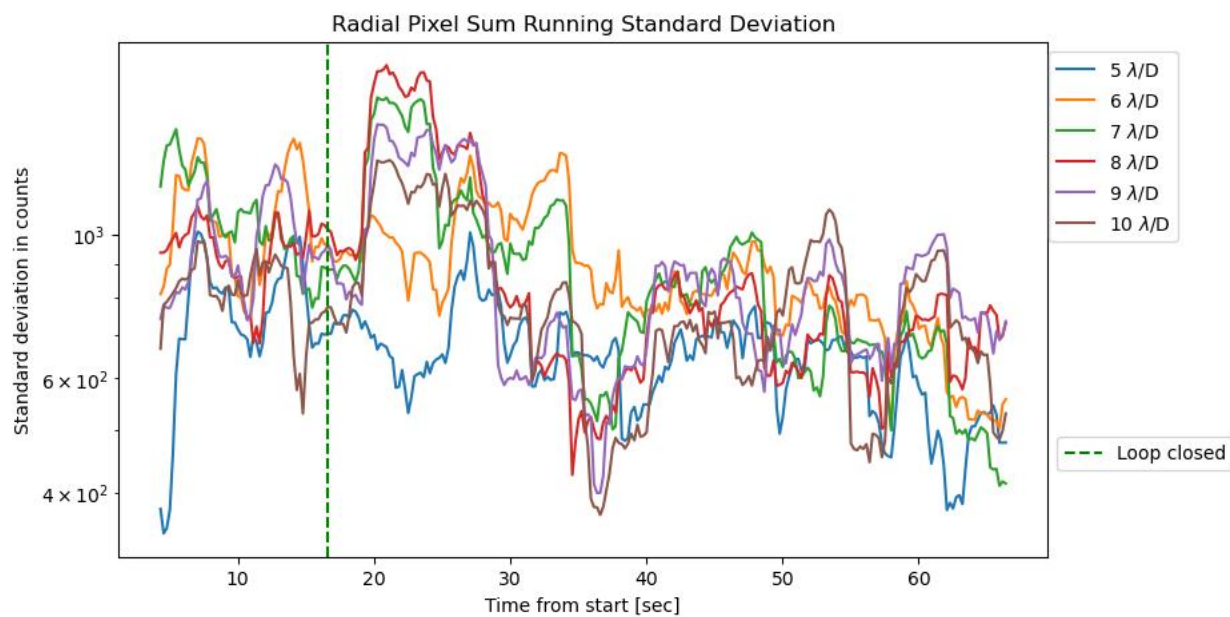


Figure 108. Running standard deviation of radial pixel sums over the data acquisition period for lowfs-z-c on-sky test.

Figures 107 and 108 indicate that the radial sums are lowered and become slightly more stable about 10 seconds after the loop is closed, with a $\sim 37\%$ relative decrease in pixel sums at 6 λ/D between open and closed loop operation.

The MSE and modal reconstruction metrics suggest the CLOWFS&C loop converges towards the reference when the loop is closed. This is shown in Figures 109 and 110.

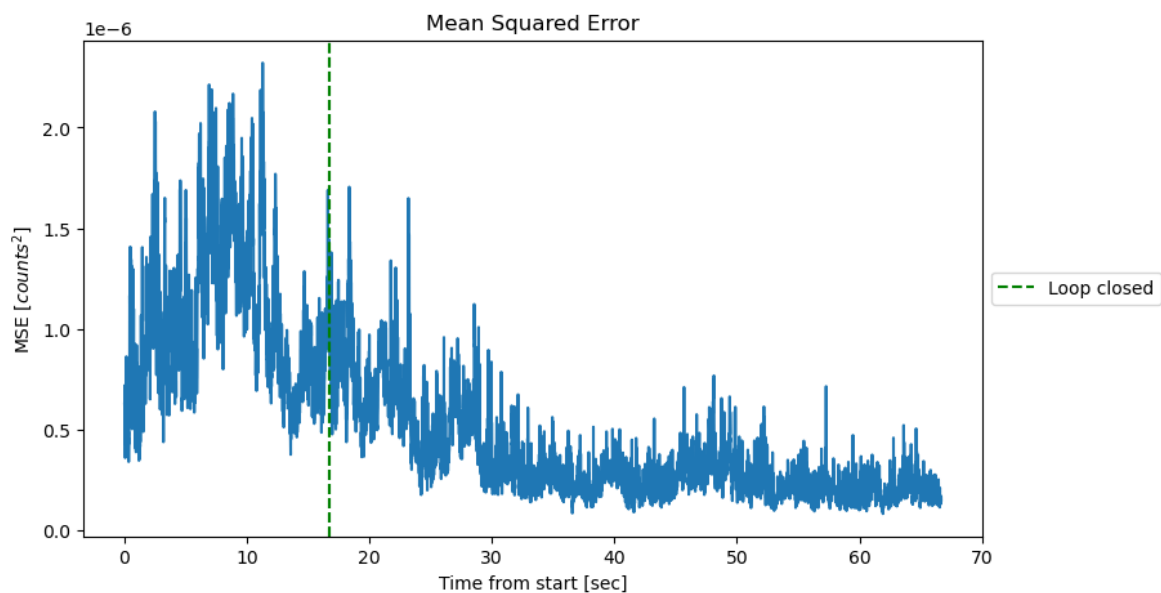


Figure 109. Mean squared error of WFS images over the data acquisition period for the lowfs-c-z on-sky test.

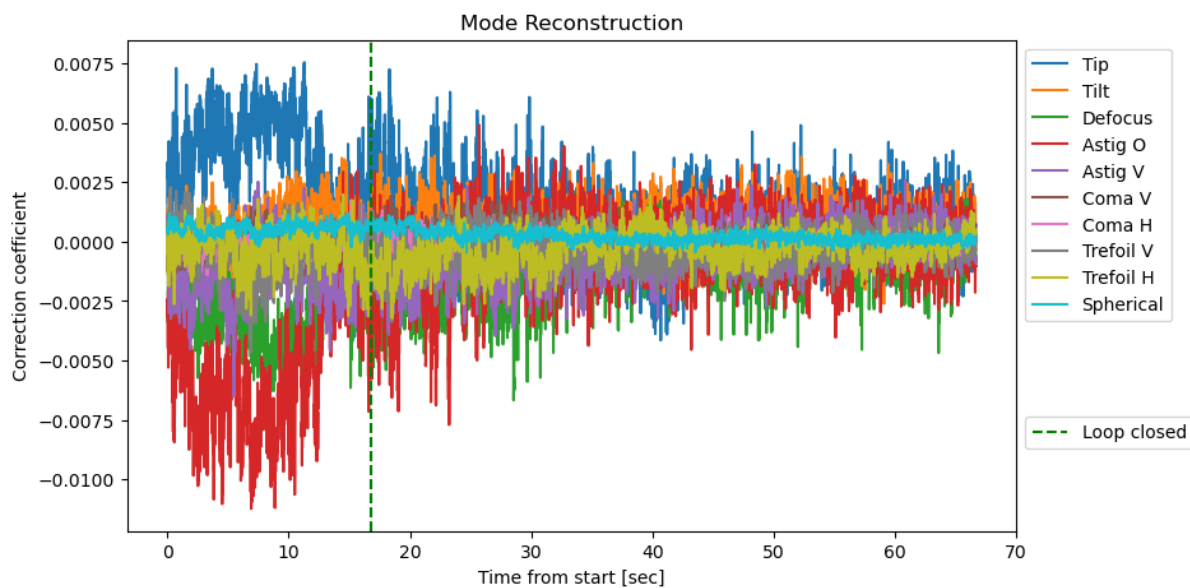


Figure 110. Correction coefficients for the first 10 Zernike modes over the data acquisition period of the lowfs-z-c on-sky test.

By evaluating the on-sky data for this calibration, it is suggested that the defocused CLOWFS&C loop successfully closed on 34 modes for the Beta pic object.

5.4.3 Additional notes

Good user-practices for loop-parameter control were developed from tests performed on the lab-source and often led to improved performance when performing LOWFS&C and CLOWFS&C on sky. This largely refers to starting with low gains and walking each gain block up one at a time, starting with the lowest order correction (tip/tilt). Variable astronomical seeing during an observation makes it difficult to identify the true loop performance over extended periods of time, as both the loop and seeing value influence the achieved Strehl in a science image. It was also seen that closing on high order modes could disrupt the corrective performance of low order modes on-sky, as was seen with lab-source tests as well. This suggests that under certain conditions it is better to only apply gains to the low order blocks and sacrifice correction on higher modes.

It is very important to note an emphasis on the quality of the reference PSF when taking a calibration. As seen in the sci1-r reference image (Figure 89), the defocused PSF had significant amounts of NCPA left in the system when the calibration was taken. Because the loop can only correct to what it was trained with, even a perfect correction with this calibration would not create an ideally optimized PSF. Furthermore, if this calibration was used on a PSF that had less residual NCPA to begin with, perfect correction would actually degrade the quality of the PSF.

6 Conclusions

LOWFS&C and CLOWFS&C provide a solution to correcting low order NCPAs in MagAO-X. NCPA control is performed in non-coronagraphic and coronagraphic configurations to increase Strehl values in science image PSFs and lower the achievable contrasts of MagAO-X.

Several configurations of low order wavefront sensing and control for defocused images were modeled, tested on the MagAO-X lab source, and implemented on sky. The baseline engineering requirements for completing this thesis included tip/tilt control on coronagraphic images using the CLOWFS&C configuration, and control of low order Zernike modes (tip/tilt through spherical) using the LOWFS&C configuration. These requirements were met and exceeded, closing the CLOWFS&C loop on up to 34 Zernike modes on-sky and the LOWFS&C loop on up to 41 Zernike modes on-sky.

Optimal defocus locations were found for several visible to NIR filters on MagAO-X for camsci1/camsci2 and camlowfs. All presented lab tests on non-coronagraphic LOWFS&C calibrations suggest >95% relative decrease in mean squared error between WFS images and the calibration reference images between open and closed loop operation. All presented CLOWFS&C lab-source tests present >30% increase in relative sparkle core sums and >20% decrease in relative radial pixel sums at $6 \lambda/D$ and $7 \lambda/D$ in coronagraphic images. On-sky data revealed a ~20% increase in relative Strehl in H α -continuum when 18 modes were closed on an H α -narrow LOWFS&C loop for PSF optimization. On-sky data presented for a CLOWFS&C loop in z-band revealed a ~51% increase in relative sparkle core sums and ~37% decrease in radial pixel sums at $6 \lambda/D$ between open and closed loop operation when 34 modes were closed on a z-band calibration. Both on-sky and lab data show a decrease in temporal changes in coronagraphic images at low (several λ/D) radial distances from the PSF core when the CLOWFS&C loop is closed. This indicates that closing the low order loop improves high contrast image stability at low angular separations from the primary target (PSF core).

Aspects of LOWFS&C and CLOWFS&C on MagAO-X worthy of further investigation include determining the limiting astronomical seeing values and effects of corrective filter

bandwidths on correction performance. It is known that certain levels of atmospheric turbulence will cause deviation from the linear regime and limit the linear loop's ability to correct for low order aberrations, though this limit was not determined throughout the completion of this thesis. Furthermore, the effects of broad vs. narrow band low order correction is not defined by the results presented here; there are too many variable parameters between data sets to definitively compare this. It is also possible that a simulated PSF could serve as the ideal reference image for closed-loop operation, and is worth considering with future implementation of (C)LOWFS&C. This would require a very accurate simulation of the instrument and may be better suited for correcting static and quasi-static NCPAs. If implemented properly, using a simulated PSF would save time when performing calibrations for a filter/camera configuration and would guarantee that the real PSF is being trained to converge to a truly ideal reference.

The optical set up required for performing LOWFS&C and CLOWFS&C as presented in this thesis is relatively simple and can be implemented in future exAO/HCI designs for ground and space-based instruments. The linear principles reviewed for low order wavefront sensing extend to applications beyond what it is currently used for in (C)LOWFS&C on MagAO-X. Adaptions of the CLOWFS&C loops presented in this thesis can be tested and used on sky for the PIAA and vAPP coronagraphs on MagAO-X as they are implemented in the system. The fundamental proof of concept presented in this thesis confirms the ability for low order NCPA correction within the science/coronagraphic arm of MagAO-X, and can therefore be improved upon and expanded in scope for future observing with MagAO-X.

7 APPENDIX A

7.1 LOWFS&C Simulation Code

The following code is written in Python 3 using Jupyter Notebook. This code is used to model defocus positions and find the optimal location for the camera in order to perform LOWFS&C. It was also used to evaluate the results of the optimal defocus positions and resulting SNR values as a function of wavelength. Cells are separated by '# In[]:' meaning code blocks could be ran independently as separated by this indicator.

```
#!/usr/bin/env python
# coding: utf-8

# In[ ]:

import numpy as np
import matplotlib.pyplot as plt
from matplotlib import animation, rc
from hci.py import *
import matplotlib.lines as mlines

micron = 10**(-6)
mm = 10**(-3)

# In[ ]:

# Set up input parameters

wl = 0.656*micron # Halpha
#wl = 0.909*micron # Z
#wl = 0.762*micron # I
#wl = 0.615*micron # R

# In[ ]:

f_ratio = 69 # camsci
p = 13*micron # pixel pitch
pix_per_resolve = 2 # pixels per resolution element (wl/ap_D)
```

```

# In[ ]:

f_ratio = 85.53 # camlowfs
p = 16*micron
pix_per_resolve = 3 # pixels per resolution element (wl/ap_D)

# In[ ]:

ap_D = 9*mm # pupil diameter
f = f_ratio*ap_D # focal length
F = f_ratio*6.5
pla = 206265*p/F # plate scale [arcseconds/pixel]

# In[ ]:

# Set up focal and pupil planes

N_pix_pupil = 256

# Focal plane parameters
spat_resolution = wl/ap_D*f # spatial resolution on focal plane
spat_extent = 32/pix_per_resolve/2 # spatial extent of the focal grid
N_pix_dm = 10

# Make pupil and focal grids
pupil_grid = make_pupil_grid(N_pix_pupil, ap_D)
focal_grid =
make_focal_grid(pix_per_resolve,spat_extent,spat_resolution)
dm_grid = make_pupil_grid(N_pix_dm,ap_D)

# Create aperture and propagator
aperture =
evaluate_supersampled(make_obstructed_circular_aperture(ap_D,0.3),pupi
l_grid,8)
#aperture = make_circular_aperture(ap_D)(pupil_grid)
prop = FraunhoferPropagator(pupil_grid, focal_grid)
wf = Wavefront(aperture, wl)
wf.total_power = 1 # normalizes wavefront power

# Make zernike basis on DM
probe_amp = 0.02 * micron / 2
rcond = 1E-5
num_modes = 10
zernike_modes = make_zernike_basis(num_modes, ap_D, pupil_grid, 2)
dm = DeformableMirror(zernike_modes)

```

```

gain = 1
leakage = 1

# Make BF mask
bf_mask = make_circular_aperture(4*wl/ap_D)(focal_grid)
imshow_field(bf_mask, grid_units = spat_resolution/f)
plt.title('Bright Field Mask')
plt.xlabel('$\lambda/D$')
plt.ylabel('$\lambda/D$')

# ## Chose defocus and print results

# In[ ]:

d = 0 * mm # chosen defocus

# set up defocused pupil
P = -d/(8*f_ratio**2) # P-V error in [m]
w = P/np.sqrt(12) # rms wfe in [m]
z = w/wl*2*np.pi # rms wfe in terms of wl
r_2 =
(pupil_grid.x/pupil_grid.x.max())**2+(pupil_grid.y/pupil_grid.y.max())
**2
defocus = np.sqrt(3)*(2*r_2 - 1)*z
defocused = PhaseApodizer(defocus)

image_ref = prop(defocused(wf)).power # reference image is taken at
wfs
response_matrix = [] # to append mode responses

# build response

for ind in range(num_modes):
    dm.flatten() # flatten dm in order to not build signals up on dm
    dm.actuators[ind] = -1*probe_amp
    image_neg = prop(dm(defocused(wf))).power - image_ref

    dm.flatten() # flatten dm in order to not build signals up on dm
    dm.actuators[ind] = 1*probe_amp
    image_pos = prop(dm(defocused(wf))).power - image_ref

    diff_image = (image_neg - image_pos)/(2*probe_amp)*bf_mask
    response_matrix.append(diff_image)

    imshow_field(diff_image, grid_units = spat_resolution/f)
    plt.title('Mode '+str(ind)+' Response')

```

```

plt.xlabel('\lambda/D$')
plt.ylabel('\lambda/D$')
plt.show()

mode_responses = ModeBasis(response_matrix)
decomp = SVD(mode_responses.transformation_matrix)

reconstruction_matrix =
inverse_tikhonov(mode_responses.transformation_matrix, rcond=rcond,
svd=decomp)

# evaluate response

r_store = []
diag = []
ctalk = []

plt.figure(figsize=(15,5))

for indx in range(num_modes):
    dm.flatten()
    dm.actuators[indx] = probe_amp*2 # check at twice the training amp
    image = prop(dm(defocused(wf))).power
    diff_image = (image - image_ref)*bf_mask

    recon_coef = reconstruction_matrix.dot(diff_image)
    crosstalk = recon_coef/(probe_amp*2)
    r_store.append(recon_coef/(probe_amp*2)) # normalize to the probe
amp, same as max(dm.actuators)
    diag.append(recon_coef[indx]/(probe_amp*2))
    crosstalk[indx] = 0
    ctalk.append(crosstalk)

signal = np.sum(np.abs(diag))
noise = np.sum(np.abs(ctalk))

SNR = signal / noise

u = 1
num = 0

for xi in diag:
    num += (-xi-u)**2
signal_std = np.sqrt(num/num_modes)

plt.figure(figsize=(15,5))

plt.subplot(121)
plt.imshow(-np.array(r_store).T,origin='lower')
plt.colorbar()

```

```

plt.title('Response Matrix')
plt.xlabel('Mode Index')
plt.ylabel('Poke Response')

plt.subplot(122)
imshow_field(image_ref/np.max(image_ref),grid_units =
spat_resolution/f)
plt.title('Defocused Reference Image')
plt.xlabel('$\lambda/D$')
plt.ylabel('$\lambda/D$')
plt.show()

plt.figure(figsize=(15,5))

plt.subplot(121)
plt.plot(-np.array(diag),label='Mode response')
plt.plot(np.sum(ctalk,axis=1),label='Cross talk response')
plt.xlabel('Poked mode index')
plt.ylabel('Normalized response')
plt.axhline(y=1,color='g',label='Ideal mode response')
plt.axhline(y=0,color='r',label='Ideal cross talk response')
plt.legend()

mode_snr = diag/np.sum(np.abs(ctalk),axis=1)

plt.subplot(122)
plt.plot(-mode_snr)
plt.xlabel('Poked mode index')
plt.ylabel('SNR')
plt.title('Modal SNR')
plt.show()

print('SNR')
print(SNR)

# ## Set defocus range and find optimal point

# In[ ]:

defocus_range = np.linspace(0*mm,30*mm,3000)

# In[ ]:

snr = []
S = []
N = []
std = []

```

```

for defoc in defocus_range:

    # set up defocused pupil

    P = -defoc/(8*f_ratio**2) # P-V error in [m]
    w = P/np.sqrt(12) # rms wfe in [m]
    z = w/wl*2*np.pi # rms wfe in terms of wl
    r_2 =
    (pupil_grid.x/pupil_grid.x.max())**2+(pupil_grid.y/pupil_grid.y.max())
**2
    defocus = np.sqrt(3)*(2*r_2 - 1)*z
    defocused = PhaseApodizer(defocus)

    image_ref = prop(defocused(wf)).power # reference image is taken
at wfs

    response_matrix = [] # to append mode responses

    # train system at that defocus

    for ind in range(num_modes):
        dm.flatten() # flatten dm in order to not build signals up on
dm
        dm.actuators[ind] = -1*probe_amp
        image_neg = prop(dm(defocused(wf))).power - image_ref

        dm.flatten() # flatten dm in order to not build signals up on
dm
        dm.actuators[ind] = 1*probe_amp
        image_pos = prop(dm(defocused(wf))).power - image_ref

        diff_image = (image_neg - image_pos)/(2*probe_amp)*bf_mask
        response_matrix.append(diff_image)

    mode_responses = ModeBasis(response_matrix)
    decomp = SVD(mode_responses.transformation_matrix)

    reconstruction_matrix =
inverse_tikhonov(mode_responses.transformation_matrix, rcond=rcond,
svd=decomp)

    # Check performance of response at that defocus

    r_store = []
    diag = []
    ctalk = []

    for indx in range(num_modes):
        dm.flatten()
        dm.actuators[indx] = probe_amp*2 # check at twice the training
amp
        image = prop(dm(defocused(wf))).power

```



```

diff_image = (image - image_ref)*bf_mask

recon_coef = reconstruction_matrix.dot(diff_image)
crosstalk = recon_coef
r_store.append(recon_coef/probe_amp/2) # normalize to the
probe amp, same as max(dm.actuators)
diag.append(recon_coef[indx]/probe_amp/2)
crosstalk[indx] = 0
ctalk.append(crosstalk)

signal = np.sum(np.abs(diag))
#signal_std = np.std(np.abs(diag))

u = 1
num = 0
for xi in diag:
    num += (-xi-u)**2
signal_std = np.sqrt(num/num_modes)

noise = np.sum(np.abs(ctalk))/probe_amp/2
S.append(signal)
N.append(noise)

SNR = signal / noise
snr.append(SNR)
std.append(signal_std)

S = np.array(S)
diff_array = np.abs(S-10)

prime_defoc = defocus_range[np.argmax(S/N)]

print('The optimum defocus for correct signal '+str(prime_defoc/mm)+'
mm\n')

# In[ ]:

# create figure and axis objects with subplots()
fig,ax = plt.subplots()
# make a plot
ax.plot(defocus_range/mm,snr,color="red")
# set x-axis label
ax.set_xlabel("Defocus [mm]", fontsize = 14)
# set y-axis label
ax.set_ylabel("SNR",color="red",fontsize=14)

# twin object for two different y-axis on the sample plot

```

```

ax2=ax.twinx()
# make a plot with different y-axis using second axis object
ax2.plot(defocus_range/mm, std ,color="blue")
ax2.set_ylabel("Std of signal",color="blue",fontsize=14)
ax.axvline(x=defocus_range[np.argmax(S/N)]/mm,color='r',ls='--',
',label='Optimal defocus')
#ax.axvline(x=defocus_range[np.argmin(std)]/mm,color='b',ls='--')
#ax.axvline(x=defocus_range[np.argmax(np.subtract(np.array(snr),np.array(std)))]/mm,color='g')
plt.title('r camlowfs')
plt.show()

print('High SNR focus: '+str(defocus_range[np.argmax(S/N)]/mm)+'
mm\n')
print('Low std focus: '+str(defocus_range[np.argmin(std)]/mm)+' mm\n')
print('Greatest difference focus:
'+str(defocus_range[np.argmax(np.subtract(np.array(snr),np.array(std))
)]/mm)+' mm')

# In[ ]:

# 2pi phase shift defocus value

delta=16*wl*f_ratio**2

# In[ ]:

d = 36.24* mm
phase = np.sqrt(3)*2*np.pi/np.sqrt(12)/wl*d/(8*f_ratio**2)

print(phase/np.pi)

# In[ ]:

# ## RESULTS SUMMARY

# In[ ]:

def polyfit(x, y, degree):
    results = {}
    coeffs = np.polyfit(x, y, degree)
    p = np.polyld(coeffs)
    #calculate r-squared
    yhat = p(x)

```

```

ybar = np.sum(y)/len(y)
ssreg = np.sum((yhat-ybar)**2)
sstot = np.sum((y - ybar)**2)
results = ssreg / sstot

return results

# In[ ]:

camlowfs_SNR = [4.27,4.58,5.38,6.49]
camsci_SNR = [4.28,4.59,5.39,6.51]
wls = [615,656,762,909]

plt.plot(wls,camlowfs_SNR,color='c',label=r'camlowfs $R^2$>0.99')
plt.plot(wls,camsci_SNR,color='m',label=r'camsci1&2 $R^2$>0.99')
plt.title('SNR vs Wavelength')
plt.xlabel(r'$\lambda$ [nm]')
plt.ylabel('SNR')
plt.legend()

lo = polyfit(wls,camlowfs_SNR,1)
print(lo)

sci = polyfit(wls,camsci_SNR,1)
print(sci)

print('\nslope\n')
print((camlowfs_SNR[3]-camlowfs_SNR[0])/(wls[3]-wls[0]))

print(np.average(np.array(camsci_SNR)-np.array(camlowfs_SNR)))

# In[ ]:

camlowfs_d = [24.89,26.47,30.55,36.24]
camsci_d = [16.34,17.37,20.05,23.76]

plt.plot(wls,camlowfs_d,color='c',label=r'camlowfs $R^2$>0.99')
plt.plot(wls,camsci_d,color='m',label=r'camsci1&2 $R^2$>0.99')
plt.title('Defocus vs Wavelength')
plt.xlabel(r'$\lambda$ [nm]')
plt.ylabel('Defocus [mm]')
plt.legend()

lo = polyfit(wls,camlowfs_d,1)
print(lo)

sci = polyfit(wls,camsci_d,1)

```

```
print(sci)

print('\nslope\n')
print((camlowfs_d[3]-camlowfs_d[0])/(wls[3]-wls[0]))
print('\nslope\n')
print((camscli_d[3]-camscli_d[0])/(wls[3]-wls[0]))
```

8 APPENDIX B

The following Appendix B entries correspond to the camera configurations for all reviewed (C)LOWFS&C lab tests.

8.1 Sci2-H α test 1 camera parameters

Table 6. Wavefront sensor camera parameters for sci2-H α test 1.

Camera	Filter	ROI	Exposure time [s]
camsci2	H α -narrow	32 x 32	0.0036365

Table 7. Focal plane camera parameters for sci2-H α test 1.

Camera	Filter	ROI	Exposure time [s]
n/a	n/a	n/a	n/a

8.2 Sci2-H α test 2 camera parameters

Table 8. Wavefront sensor camera parameters for sci2-H α test 2.

Camera	Filter	ROI	Exposure time [s]
camsci2	H α -narrow	32 x 32	0.0036365

Table 9. Focal plane camera parameters for sci2-H α test 2.

Camera	Filter	ROI	Exposure time [s]
n/a	n/a	n/a	n/a

8.3 Lowfs-z test 1 camera parameters

Table 10. Wavefront sensor camera parameters for lowfs-z test 1.

Camera	Filter	ROI	Exposure time [s]
camlowfs	z	32 x 32	0.001505

Table 11. Focal plane camera parameters for lowfs-z test 1.

Camera	Filter	ROI	Exposure time [s]
n/a	n/a	n/a	n/a

8.4 Lowfs-z test 2 camera parameters

Table 12. Wavefront sensor camera parameters for lowfs-z test 2.

Camera	Filter	ROI	Exposure time [s]
camlowfs	z	32 x 32	0.001505

Table 13. Focal plane camera parameters for lowfs-z test 2.

Camera	Filter	ROI	Exposure time [s]
n/a	n/a	n/a	n/a

8.5 Lowfs-z-c test 1 camera parameters

Table 14. Wavefront sensor camera parameters for lowfs-z-c test 1.

Camera	Filter	ROI	Exposure time [s]
camlowfs	z	32 x 32	0.00152

Table 15. Focal plane camera parameters for lowfs-z-c test 1.

Camera	Filter	ROI	Exposure time [s]
camsci1	Ha-cont	1024 x 1024	0.22626

8.6 Lowfs-z-c test 2 camera parameters

Table 16. Wavefront sensor camera parameters for lowfs-z-c test 2.

Camera	Filter	ROI	Exposure time [s]
camlowfs	z	32 x 32	0.00152

Table 17. Focal plane camera parameters for lowfs-z-c test 2.

Camera	Filter	ROI	Exposure time [s]
camsci1	Ha-cont	1024 x 1024	0.22626

9 APPENDIX C

The following Appendix C entries correspond to the camera configurations for all reviewed (C)LOWFS&C on-sky tests.

9.1 Sci2-Ha on-sky test camera parameters

Table 18. Wavefront sensor camera parameters for sci2-h α on-sky test.

Camera	Filter	ROI	Exposure time [s]
camsci2	h α -narrow	32 x 32	2

Table 19. Focal plane camera parameters for sci2-h α on-sky test.

Camera	Filter	ROI	Exposure time [s]
camsci1	h α -cont.	1024 x 1024	1.15494

9.2 Sci1-r on-sky test

Table 20. Wavefront sensor camera parameters for sci1-r on-sky test.

Camera	Filter	ROI	Exposure time [s]
camsci1	r	32 x 32	1.5

Table 21. Focal plane camera parameters for sci1-r on-sky test.

Camera	Filter	ROI	Exposure time [s]
camsci2	r	1024 x 1024	0.1

9.3 Lowfs-z-c on-sky test

Table 22. Wavefront sensor camera parameters for lowfs-z-c on-sky test.

Camera	Filter	ROI	Exposure time [s]
camlowfs	z	32 x 32	0.01

Table 23. Focal plane camera parameters for lowfs-z-c on-sky test.

Camera	Filter	ROI	Exposure time [s]
camsci1	ha-cont		0.22626

10 APPENDIX D

This appendix contains all calibrations taken in 2023A for LOWFS&C and CLOWFS&C configurations that did not cause the loop to diverge during lab testing or while on sky. Not all calibrations have undergone rigorous testing and data review, though those that have been reviewed in this thesis are indicated.

10.1 LOWFS&C calibrations from 2023A

Table 24. LOWFS&C calibrations taken during the 2023A observing run.

Camera	Filter	ROI	Calibration name	Notes
camsci2	H α -narrow	32 x 32	2023A_camsci2_halpha_0.92Strehl_32x32	sci2-H α , reviewed
camsci2	r	33 x 32	2023A_camsci2_r_defocused	not reviewed
camsci1	r	34 x 32	2023A_lowfs_camsci1_r_defocused_nocoro_v2	sci1-r, reviewed
camlowfs	z	35 x 32	2023A_lowfs_camlowfs_z_32x32	lowfs-z, reviewed
camlowfs	r	36 x 32	2023A_lowfs_camlowfs_r_defocused_v2	not reviewed

10.2 CLOWFS&C calibrations from 2023A

Table 25. CLOWFS&C calibrations taken during the 2023A observing run.

Camera	Filter	ROI	Calibration name	Notes
camlowfs	z	32 x 32	2023A_lowfs_camlowfs_z_Slyot_defocused	lowfs-z-c, small Lyot coronagraph, reviewed
camlowfs	z	16 x 16	2023A_lowfs_camlowfs_z_dichroic_in_focus	tip/tilt control only, small Lyot coronagraph camlowfs in focal plane, not reviewed
camlowfs	z	16 x 16	2023A_lowfs_camlowfs_z_in_focus_lyotS	tip/tilt control only, PIAA coronagraph, camlowfs in focal plane, not reviewed

11 References

- [1] M. Mayor and D. Queloz, “A Jupiter-mass companion to a solar-type star,” *Nature*, vol. 378, Nov. 23, 1995.
- [2] D. Ziqi, et al, 2021, *J. Phys.: Conf. Ser.* 2012 012135.
- [3] J. R. Males, L. M. Close, et al, “MagAO-X: current status and plans for Phase II”, *Proc. SPIE 12185, Adaptive Optics Systems VIII*, 1218509 (29 August 2022); <https://doi.org/10.1117/12.2630584>.
- [4] Martinache, F., Guyon, O., et al, “On-Sky Speckle Nulling Demonstration at Small Angular Separation with SCExAO”, *Publications of the Astronomical Society of the Pacific*, Vol. 126 No. 940, (June 2014) pp. 565-572.
- [5] J. D. Long, “Giant Exoplanets, Sirius, and Starlight Subtraction at Scale”, Ph.D. thesis, Steward Observatory, University of Arizona, Tucson, AZ, 2023.
- [6] L. M. Close, J. R. Males, et al, “Status of MagAO and review of astronomical science with visible light adaptive optics”, *Proc. SPIE 10703 Adaptive Optics Systems VI*, 107030L (10 July 2018); <https://doi.org/10.1117/12.2313107>.
- [7] R. Dekany, J. Roberts, et al, “PALM-3000: Exoplanet adaptive optics for the 5-meter Hale telescope”, *The Astrophysical Journal*, 19 August 2013.
- [8] N. Jovanovic, F. Martinache, et al, “The Subaru Coronagraphic Extreme Adaptive Optics System: enabling high-contrast imaging on solar-system scales”, *Publications of the Astronomical Society of the Pacific*, September 2015, 127, 890

- [9] J. Beuzit, M. Feldt, et al, “SPHERE: a planet finder instrument for the VLT”, *Proc. SPIE 7014, Ground-based and Airborne Instrumentation for Astronomy II*, 701418 (25 July 2008); <https://doi.org/10.1117/12.790120>
- [10] P. J. Valle, A. Fuentes, V. F. Canales, M. A. Cagigas, and M. P. Cagigal, “Digital Coronagraphy: application to space telescope images”, *OSA Continuum*, Vol. 2, No. 6, 15 June 2019.
- [11] O. Guyon, E. A. Pluzhnik, M. J. Kuchner, B. Collins, and S. T. Ridgway, “Theoretical Limits on Extrasolar Terrestrial Planet Detection with Coronagraphs”, *The Astrophysical Journal*, 24 August 2006.
- [12] R. Galicher and J. Mazoyer, “Imaging exoplanets with coronagraphic instruments”, *Comptes Rendus. Physique*, Online first (2023), pp. 1-45; <https://doi.org/10.5802/crphys.133>
- [13] K. Miller, J. R. Males, et al, “Focal plane wavefront sensing and control strategies for high-contrast imaging on the MagAO-X instrument”, *Proc. SPIE 10703, Adaptive Optics Systems VI*, 107031T (10 July 2018); <https://doi.org/10.1117/12.2312809>.
- [14] O. Guyon, T. Matsuo, and R. Angel, “Coronagraphic low-order wave-front sensor: principle and application to a phase-induced amplitude coronagraph”, *The Astrophysical Journal*, 27 February 2009.
- [15] S. Garima, F. Martinache, P. Baudoz, O. Guyon, T. Matsuo, N. Jovanovic, and C. Clergeon, “Lyot-based low order wavefront sensor for phase-mask coronagraphs:

- principle, simulations and laboratory experiments”, *Publications of the Astronomical Society of the Pacific*, Vol. 126, No. 940 (June 2014), pp. 586-594.
- [16] F. Martinache, N. Jovanovic, and O. Guyon, “Closed-loop focal plane wavefront control with the SCExAO instrument”, *Astronomy & Astrophysics*, 9 November 2018.
- [17] K. Miller, O. Guyon, and J. Males, “Spatial linear dark field control: stabilizing deep contrasts for exoplanet imaging using bright speckles”, *Journal of Astronomical Telescopes, Instruments, and Systems* 3(4), 049002 (30 October 2017).
<https://doi.org/10.1117/1.JATIS.3.4.049002>
- [18] R. J. Noll, “Zernike polynomials and atmospheric turbulence”, *Journal of the Optical Society of America*, Vol. 66, No. 3, March 1976.
- [19] S. P. Bos, D. S. Doelman, J. Lozi, O. Guyon, C. U. Keller, K. L. Miller, N. Jovanovic, F. Martinache, and F. Snik, “Focal-plane wavefront sensing with the vector-apodizing phase plate”, *Astronomy & Astrophysics*, 632, A48, 10 September 2019.
- [20] J. W. Goodman, *Introduction to Fourier Optics*, Roberts and Company Publishers, 2005.
- [21] V. Sacek, “Amateur telescope optics”, sec. 4.4, Web-published 14 July 2006,
<https://www.telescope-optics.net/index.htm>
- [22] O. Guyon, S. Arnaud, et al, “The Compute and Control for Adaptive Optics (cacao) real-time control software package”, *Proc. SPIE 10703, Adaptive Optics Systems VI*, 107031E (17 July 2018); <https://doi.org/10.1117/12.2314315>
- [23] K. Van Gorkom, J. R. Males, et al, Characterizing deformable mirrors for the MagAO-X instrument”, *Journal of Astronomical Telescopes, Instruments, and Systems* 7(3), 039001 (2 August 2021). <https://doi.org/10.1117/1.JATIS.7.3.039001>